

Design and Modeling of Ferroelectric BST FBARs for Switchable RF Bulk Acoustic Wave Filters

by

Seungku Lee

A dissertation submitted in partial fulfillment
of the requirements for the degree of
Doctor of Philosophy
(Electrical Engineering)
in the University of Michigan
2016

Doctoral Committee:

Professor Amir Mortazawi, Chair
Associate Professor Anthony Grbic
Professor Jerome P. Lynch
Professor Kamal Sarabandi

@ Seungku Lee 2016

To my wife and parents

ACKNOWLEDGMENTS

As an optimist, I feel very lucky to meet a variety of great people while I have been doing what I like most. Therefore, I would like to take this chance to sincerely acknowledge and appreciate them.

My first acknowledgment must go to my admirable PhD advisor and great friend, Prof. Amir Mortazawi. Thanks to his encouragement, support, and guidance, I have learned how a PhD student could become a successful independent researcher. Every time I solved the problems encountered during my PhD (still there are), I felt a great sense of achievement and satisfaction that others cannot easily imagine. Also, I would never forget what he told me right after my first IMS in June 2012: “If we are the biggest critiques of our work, we won’t get surprised.” This made an impression on me and I always wish that for myself.

I appreciate my great thesis committee members. I would like to thank Prof. Kamal Sarabandi for his theoretical and practical comments on my work. Also, his wonderful EECS 530 class strengthened my EM knowledge. I would like to thank Prof. Anthony Grbic for his invaluable comments and thoughts. It was also my great pleasure working with him as a GSI during my last semester. I would like to thank Prof. Jeromy P. Lynch for providing me with his insights and points of view on my work from different angles, which broadened my PhD work. Also, I would like to express my sincere appreciation to my MS advisor, Prof. Yongshik Lee at Yonsei University in Korea who is also a Radlab alum (2004) and first led me to dive in RF & Microwave circuits. He has been my great mentor and friend since I first met him in 2006. I also would like to thank Prof. Jong-Gwan Yook at Yonsei, as well as Prof. Mina Rais-Zadeh and Prof. Jamie Philips at Michigan.

My PhD work was possible with the help of my wonderful friends, Dr. Victor Lee now in Apple and Prof. Seyit Ahmet Sis now at Balikesir University in Turkey. It was my great pleasure to discuss, collaborate, and hang out with them during my first two and half years in Ann Arbor. I also thank Prof. Xinen (Alfred) Zhu and Milad Zolfagharloo Koochi for

their valuable comments and friendship. I also thank former and current research group members, Dr. Jonghoon Choi, Dr. Waleed Alomar, Xiaoyu Wang, Noyan Akbar, and Omar Abdelatty for their help and support. Also, I would like to thank former and current Rad Lab/EM track Korean friends and Radlab class of 2011, Professor Jungsuek Oh, Dr. Young Jun Song, Dr. Sangjo Choi, Jihun Choi, Taehee Jang, Hyeongseok Kim, Armin Jan, and Brian Tierney for their encouragement, guidance, and friendship throughout my PhD. I would like to thank all my former and current Korean friends, Radiation Lab friends, SSEL friends, EECS friends, Lurie Nano Fabrication (LNF) friends, and Korean Student Associate-Graduate (KSAG) board member friends for 2014-2015. Also, I would like to thank all staff in Radiation Lab, EECS department, LNF for their help throughout my PhD.

I had opportunities to be a Graduate Student Instructor (GSI) which gave me the great pleasure of teaching. I thank all my students for their passion and enthusiasm. I also thank course instructors, Prof. Mortazawi in W13 EECS 411, Prof. Gilchrist in W14 EECS 430, and Prof. Grbic in W16 EECS 430 for their encouragement and feedback. Also, I would like to thank Dr. Adib Nashashibi and Mr. David Boprie for their enormous help for my lab session preparation. I also acknowledge my other funding sources, NSF, EECS fellowship during my first year, and Rackham Predoctoral Fellowship for 2014-2015.

Lastly and most importantly, I would like to thank my family, without which my PhD would be impossible. I would like to thank all my relatives and my parents-in-law for their enormous love and support. Thank you my best teachers, my father Ilhoon Lee and mother In Hee Hwang who have raised me with their endless love and support. Fortunately, I have grown up watching their diligent work ethic, independence, optimism, and empathy to others. Thanks to them I could build up my life attitude and personality which I regard as my best assets. Thank you my parents, I love you. Finally, I like to express my greatest love to Hyeongkyeong Kim who was my first love, 10-year friend, and is my wife now. You make me happier than I thought I could be and I love to spend my entire life trying to make you feel the same way. Looking back it was the luckiest moment in my life that I met you and fell in love with you in Yonsei. Thank you Hyeongkyeong, I love you.

May 2016
Seungku Lee

TABLE OF CONTENTS

DEDICATION.....	ii
ACKNOWLEDGEMENTS.....	iii
LIST OF TABLES.....	ix
LIST OF FIGURES.....	x
LIST OF APPENDICES.....	xix
ABSTRACT.....	xx
CHAPTER	
I. Introduction.....	1
1.1. Dissertation Motivation.....	1
1.2. Background.....	4
1.2.1. BST Operation in Paraelectric Phase.....	4
1.2.2. Electric-Field-Dependent Permittivity.....	6
1.2.3. Electric-Field-Induced Piezoelectricity (Electrostriction)...	7
1.2.4. BST Acoustic Resonators.....	9
1.2.5. Frequency Response of Switchable BST FBARs.....	11
1-3. Dissertation Goal and Organization.....	13
II. Nonlinear Behavior and Circuit Modeling of Intrinsically Switchable Ferroelectric BST FBARs.....	17
2.1. Chapter Motivation.....	17
2.2. Fabrication Procedure and Measurements of Ferroelectric BST FBARs.....	19

2.3. DC-Bias-Voltage and RF-Power-Level Dependence of Intrinsicly Switchable Ferroelectric BST FBARs.....	22
2.4. Nonlinear Circuit Modeling of intrinsicly Switchable Ferroelectric BST FBARs.....	29
2.4.1. Existing Nonlinear Circuit Model for Capacitance $C_e(V)$	29
2.4.2. Nonlinear Modeling of Electromechanical Coupling Coefficient $k_t^2(V)$	31
2.4.3. Nonlinear Modeling of Parallel Resonance Frequency $f_p(V)$.	36
2.4.4. Nonlinear Modeling of BST FBAR Impedance.....	38
2.5. Example Modeling Procedure based on the Measurement Results for the Intrinsicly Switchable BST FBAR.....	41
2.6. Comparison between Measurement and Modeling Results.....	49
2.7. Chapter Conclusion.....	55
III. Design and Characterization of Intrinsicly Switchable Ferroelectric BST-on-Si Composite FBARs.....	57
3.1. Chapter Motivation.....	57
3.2. BST-on-Si Composite FBARs with High Quality Factors.....	59
3.2.1 Design Procedure based on 1-D Acoustic Transmission Line Model.....	59
3.2.2. Fabrication Procedure using RF Magnetron Sputtering.....	65
3.2.3 Measurement Results and Discussion.....	67
3.2.4 Temperature Dependent Characteristics of Intrinsicly Switchable Ferroelectric Composite FBARs.....	71
3.3. BST-on-Si Composite FBARs for Maximum K_t^2	77
3.3.1. Design Procedure based on 1-D Acoustic Transmission Line Model.....	77
3.3.2. Design Procedure based on 2-D Multiphysics Simulation for Lateral-Wave Spurious-Modes Elimination.....	80
3.3.3. Fabrication Procedure for Spurious-Free Composite BST FBARs for Maximum K_t^2	83

3.3.4. Measurement and Modeling Results.....	84
3.4. Chapter Conclusion.....	88
IV. Design of Intrinsically Switchable RF Bulk Acoustic Wave	90
Filters.....	90
4.1. Chapter Motivation.....	90
4.2. Image Parameter Method Applicable to a Periodic Structure.....	91
4.3. Calculation of Image Impedance for BAW Filters.....	94
4.4. Calculation of Propagation Constant for BAW Filters.....	98
4.5. Filter Insertion Loss and Rejection Level Prediction.....	101
4.6. Design Considerations for BAW Filters.....	104
4.7. Ladder-Type BAW Filter Design Example.....	105
4.8. Fabrication Procedure and Measurement Setup for BAW Filters.....	109
4.9. BST FBAR Filter Measurement Results.....	111
4.10. Chapter Conclusion.....	114
V. Conclusion.....	116
5.1. Summary of contribution.....	116
5.2. Future Direction.....	117
5.2.1. BST Growth Condition Characterization and Optimization using RF Magnetron Sputtering.....	117
5.2.2. Linearity Improvement of BST FBARs and FBAR Filters..	119
5.2.3. Reconfigurable Filter Bank based on Switchable BST FBAR Filters.....	121
5.3. Publications.....	124
5.3.1. Journal publications.....	124
5.3.2. Conference publications.....	125
5.3.3. Under Review or In-Preparation.....	128
APPENDICES.....	129

BIBLIOGRAPHY..... 157

LIST OF TABLES

Table 2.1:	Field Variables and Material Parameters in (2-7)-(2-13) for Thickness-Extensional Mode [16]-[18].....	33
Table 2.2:	Complete Equations and Nonlinear Model Parameter Values.....	47
Table 3.1:	Acoustic Parameters used in 1-D Acoustic Transmission Line Model Simulations in Chapter 3.2.....	62
Table 3.2:	Parameter Values of mBVD Model in Fig. 3.6.....	70
Table 3.3:	Acoustic Parameters used in 1-D Acoustic Transmission Line Model Simulations in Chapter 3.3.....	77
Table 3.4:	BST Material Parameters used in COMSOL Multiphysics Simulations.....	85
Table 3.5:	mBVD Model Parameters	86
Table 4.1:	Complete Simulation Parameters (Device Parameters).....	114
Table 4.2:	Complete Simulation Parameters (Circuit Parameters).....	114

LIST OF FIGURES

Figure

1.1	(a) Generic RF front-end and (b) Proposed RF front-end based on switchable ferroelectric BST FBAR reconfigurable devices.....	3
1.2	Temperature dependent response of ferroelectric BST material in its ferroelectric phase (below T_c) and its paraelectric phase (above T_c) (reproduced from [2]).....	5
1.3	Temperature dependent dielectric constant characteristic of $Ba_xSr_{1-x}TiO_3$ ceramics with the different composition of x (reproduced from [4]).....	6
1.4	Bias voltage dependent capacitance of BST varactors.....	7
1.5	Measurement results of dc-bias voltage dependent electromechanical coupling coefficient for a 1-port BST FBAR [36].....	9
1.6	Cross-sectional view of (a) a BST FBAR and (b) a BST-on-Si composite FBAR.....	10
1.7	Cross-sectional view of a BST SMR.....	10
1.8	Typical frequency responses of BST FBARs with (on) and without (off) the applied dc bias voltage. (a) Magnitude of input impedance and (b) reflection coefficients on the Smith chart when the switchable resonator is in its on- and off-states.....	12

1.9	(a) mBVD circuit model and (b) capacitor model applicable when the switchable resonator is in on- and off-states, respectively.....	12
2.1	Fabrication procedure for ferroelectric BST FBARs.....	20
2.2	A photograph of a typical BST FBAR that has an area of $650 \mu\text{m}^2$. The device was fabricated using pulsed laser deposition (PLD).....	21
2.3	Measurement setup for dc-bias-voltage and RF-power-level dependent S parameters of a fabricated intrinsically switchable 1-port BST FBAR.....	22
2.4	Measured capacitance for a BST FBAR as a function of dc bias voltage.....	23
2.5	Measurement results of electromechanical coupling coefficient for the fabricated 1-port BST FBAR as a function of dc bias voltage.....	23
2.6	Measurement results of resonance frequencies for the fabricated 1-port BST FBAR as a function of dc bias voltage.....	24
2.7	Measurement results of real part of input admittance at the series resonance frequency for the fabricated 1-port BST FBAR as a function of dc bias voltage.....	25
2.8	Measurement results of real part of input impedance at the parallel resonance frequency for the fabricated 1-port BST FBAR as a function of dc bias voltage.....	25
2.9	$K_{t,eff}^2$ and Q of the BST FBAR as a function of P_{avs} with different applied dc bias voltages.....	27

2.10	Measurement results of reflection coefficients for the BST FBAR on the Smith chart (100 MHz to 3 GHz) at a dc bias voltage of (a) 5 V and (b) 25 V with P_{avs} of 0, 4, and 8 dBm.....	29
2.11	A schematic of lossless nonlinear model for intrinsically switchable ferroelectric BST FBARs. Parameters C_e , L_m , and C_m are a function of applied voltage.....	30
2.12	A typical capacitance-voltage curve for BST varactors.....	31
2.13	A schematic of nonlinear model for intrinsically switchable ferroelectric BST FBARs that incorporate mechanical loss, dielectric loss, and ohmic loss. Parameters C_e , L_m , C_m , R_m , and R_e are a function of applied voltage. Parameter R_s represents the device ohmic loss.....	39
2.14	Modeling results of capacitance $C_e(V)$. C_{max} , C_f , and V_2 in (2-6) are found to be 5.84 pF, 0.39 pF, and 6.45 V.....	42
2.15	Modeling results of electromechanical coupling coefficient $k_r^2(V)$. B_0 is - 5.191×10^{-3} and B_1 is 151.48×10^{-3}	43
2.16	Modeling results for the parallel resonance frequency $f_p(V)$. A_0 is - 8.9416×10^6 and A_1 is 2.0805×10^9	44
2.17	Modeling results for the series resonance frequency $f_s(V)$	44
2.18	Modeling results of real part of input admittance at the series resonance frequency $\text{Real}\{Y_{in}(V)\}$. $Q_m(V)$ is 80.1.....	45
2.19	Modeling results of real part of input impedance at the parallel resonance frequency $\text{Real}\{Z_{in}(V)\}$. $Q_e(V)$ is 14.4.....	46

2.20	Comparison between the measurement and simulation results of reflection coefficient for intrinsically switchable ferroelectric BST FBARs on the Smith Chart. DC bias voltage is varied from 0 to 25 V in 5 V increments under -18 dBm RF power level.....	50
2.21	Comparison between the measurement and simulation results of magnitude of input impedance for intrinsically switchable ferroelectric BST FBARs. DC bias voltage is varied from 0 to 25 V in 5 V increments under -18 dBm RF power level.....	50
2.22	Comparison between the measurement and simulation results of phase of input impedance for intrinsically switchable ferroelectric BST FBARs. DC bias voltage is varied from 0 to 25 V in 5 V increments under -18 dBm RF power level.....	51
2.23	Comparison between the measurement and simulation results of reflection coefficient for intrinsically switchable ferroelectric BST FBARs on the Smith chart. RF power level is varied from 0 to 8 dBm in 4 dBm increments at (a) 5 V and (b) 25 V dc bias voltage.....	52
2.24	Comparison between the measurement and simulation results of magnitude of input impedance for intrinsically switchable ferroelectric BST FBARs. RF power level is varied from 0 to 8 dBm in 4 dBm increments at (a) 5 V and (b) 25 V dc bias voltage.....	53
2.25	Comparison between the measurement and simulation results of phase of input impedance for intrinsically switchable ferroelectric BST FBARs. RF	54

	power level is varied from 0 to 8 dBm in 4 dBm increments at (a) 5 V and (b) 25 V dc bias voltage.....	
3.1	A cross section of a BST-on-Si composite FBAR. This is not to scale.....	60
3.2	Simulated (a) K_t^2 (b) quality factor, (c) BST thickness and Si thickness as a function of BST to Si thickness ratio and different thickness-extensional resonance mode number. The simulation is based on the 1-D acoustic transmission line model.....	63
3.3	Fabrication process for a BST-on-Si composite FBAR: (a) bottom electrode, (b) BST deposition, (c) top electrode, (d) BST etching, (e) contact, and (f) Si DRIE.....	66
3.4	A photograph of a fabricated 1-port BST FBAR (AFBAR=1600 μm^2). The vertical dimensions for fabricated devices are as follows: $t_{\text{Top}}=100$ nm, $t_{\text{BST}}=400$ nm, $t_{\text{Bot}}=100$ nm, $t_{\text{Buf}}=200$ nm, $t_{\text{Si}}=5$ μm	67
3.5	Measurement and modeling results for a 1-port switchable BST FBAR when the resonator is in the <i>on</i> ($V_{\text{dc}}=40$ V) and <i>off</i> (0 V) states. (a) Magnitude of input impedance and (b) reflection coefficients on the Smith chart.....	68
3.6	A schematic of mBVD model that includes an additional branch for spurious resonance and the parasitic inductance L_s for better fitting to measurements. The model is for when the BST FBAR is in its <i>on</i> state.....	69
3.7	(a) A photograph of a fabricated composite FBAR with the area of 1325 μm^2 and (b) a schematic cross section of a composite FBAR.....	72

3.8	Measured magnitude of input impedance (Z_{in}) results for the BST-on-Si composite FBAR with various temperatures (Temp.=30°C, 50°C, 70°C, 90°C) when the resonator is switched on ($V_{dc}=40$ V) and off ($V_{dc}=0$ V).....	72
3.9	The change in (a) series and (b) parallel resonance frequencies with respect to temperature. The results are shown at a bias of 5, 10, 20, 30, and 40 V.....	74
3.10	The change in (a) $K_{t,eff}^2$ and (b) Q with respect to temperature. The results are shown at a bias voltage of 5, 10, 20, 30, and 40 V.....	76
3.11	Simulated (a) $K_{t,eff}^2$, (b) BST thickness, and (c) Si thickness as a function of BST to Si thickness ratio at the third resonance mode for a 2-GHz resonator. Simulation is based on the 1-D acoustic transmission line model.....	80
3.12	Measurement results for a typical BST-on-Si composite FBARs at different resonance mode. The FBAR area is 1600 μm^2	81
3.13	(a) Typical dispersion diagram for a type I resonator and (b) a cross-sectional view of BST-on-Si composite FBAR with a raised frame. This is not to scale.....	82
3.14	A photograph of a fabricated BST-on-Si composite FBAR (a) with a frame and (b) without a frame.....	83
3.15	Measured and simulated reflection coefficients on the Smith chart for fabricated BST-on-Si composite FBARs with and without a frame in Fig. 3.14.....	85

3.16	A schematic of mBVD model.....	86
3.17	Magnitude of input impedance for measured/modeled FBAR with a frame and measured FBAR without a frame.....	87
4.1	A schematic of a ladder-type BAW filter starting with a series resonator....	92
4.2	A schematic of a filter consisting of unit cells for which image parameter method can be applied in the filter design (reproduced from [88]).....	92
4.3	A filter unit cell terminated in its image impedances (reproduced from [88]).....	93
4.4	Typical propagation constant (γ) characteristics of a bandpass filter in the passband and the stopband. Attenuation constant (α) and phase constant (β) are shown (reproduced from [88]).....	93
4.5	Schematic of a general pi-type network.....	93
4.6	A schematic of a pi-type unit cell for ladder-type BAW filter in terms of (a) device parameters C_e, f_{s1} (or f_{p1}), and K_t^2 and (b) circuit parameters $C_e,$ $C_m,$ and L_m	94
4.7	A schematic of a pi-type unit cell for ladder-type BAW filter including device loss terms ($R_m, R_s,$ and R_e).....	101
4.8	Equivalent circuit of Fig. 4.7 at the filter center frequency. The circuit consists of resistors which represent device loss terms ($R_m, R_s,$ and R_e).....	102
4.9	Equivalent circuit of Fig. 4.7 in the stopband. The circuit consists of electrical capacitors only (C_{e1} and C_{e2}).....	103
4.10	Schematic of the designed filter with calculated device parameters.....	105

4.11	ADS circuit simulation results of (a) transmission (S_{21}) and (b) reflection (S_{11}) for the designed filter in Fig. 4.10. Q_m is varied from 100 to 1000 in increments of 100.....	106
4.12	Comparison between circuit simulation and predicted results for (a) fractional bandwidth defined as frequency in which $S_{11} < -10$ dB, (b) minimum insertion loss, and (c) rejection level with quality factors from 100 to 1000 in increments of 100.....	108
4.13	Intrinsically switchable BST FBAR filter fabrication procedure.....	109
4.14	(a) A photograph of the fabricated π -type switchable ferroelectric BST FBAR filter and (b) its corresponding circuit schematic. R_{bias} is designed to be 1 kohm. Two double-sized FBARs are connected in series for easier biasing.....	110
4.15	Intrinsically switchable BST FBAR filter measurement setup.....	111
4.16	Measured and simulated (a) transmission and (b) reflection results for a fabricated switchable ferroelectric BST FBAR filter.....	112
4.17	Equivalent circuit for the FBAR filter shown in Fig. 4.14(b). Circuit parameters are given in Table 4.2.....	113
5.1	Schematics of an FBAR with different number of resonators connected in series for improved linearity.....	119
5.2	Input-referred third-order intercept point (IIP3) and peak-to-peak RF voltage swing simulation results for a BST FBAR based on the developed nonlinear model.....	120

5.3 Proposed switched BST filter bank circuit diagram consisting of four filters with series connected BST varactors..... 122

5.4 Simulation results for the proposed switched filter bank consisting of four 2.5-stage filters with matching networks comprising two shunt inductors as well as eight BST varactors..... 123

LIST OF APPENDICES

Appendix A:	Relationship between Device and Circuit Parameters.....	130
Appendix B:	ADS Circuit Models.....	133
Appendix C:	Matlab Code for Nonlinear Model Parameter Extraction and 1-D Acoustic Transmission Line Model Simulation.....	137
Appendix D:	RF Magnetron Sputtering Standard Operating Procedures (SOP).	148
Appendix E:	Fabrication Process in Lurie Nanofabrication Facility (LNF).....	154

ABSTRACT

Multi-standard smartphones have become ubiquitous in everyday life. Such systems operate under different communication standards (2G, 3G, 4G-LTE, WLAN, GPS, Bluetooth, etc.) at different frequencies. Compact and high-performance filters are indispensable for RF front-ends in mobile phones, and RF bulk acoustic wave (BAW) filters, based on piezoelectric film bulk acoustic resonators (FBARs), have become prevalent. Moreover, due to the upcoming Internet of Things (IoT) and 5G, the demand for new technologies that can be employed to design switchable/tunable filters has increased.

This dissertation presents one of the new promising technologies, known as *intrinsically-switchable BAW filters* employing newly-investigated *electrostrictive effect in BST thin films*. Successful implementation of switchable filters would eliminate/minimize external switches in the design of filter banks, thus leading to significant reduction in their size, cost, and complexity.

Contributions of this work are categorized into three major parts. First, the *nonlinear circuit modeling* procedure for BST FBARs is presented. The nonlinear circuit model, essential for the material characterization and device characterization including linearity analysis, is developed based on the physics of electrostriction-based intrinsically switchable FBARs. Modeling results are in close agreement with dc-bias-voltage and RF-power-level dependent measurement results for BST FBARs.

Second, the design methods for BST-on-Si composite FBARs are presented. The designed composite FBAR shows *a record Q of 970 at 2.5 GHz* among switchable BST resonators. Temperature-dependent characteristics of BST-on-Si composite FBAR devices are also presented with the measured TCF of -35 ppm/K. Furthermore, a raised-frame technique, which has been used to *eliminate lateral-wave spurious-modes* in piezoelectric BAW resonators, is first employed for switchable ferroelectric FBARs, demonstrating the effectiveness of the frame technique.

Finally, the design method for intrinsically switchable BST FBAR filters is presented. The *filter design method* for ladder-type BAW filters is developed based on image parameters. Closed-form equations are derived for the first time enabling one to accurately design BAW filters. A systematically-designed pi-type BST FBAR filter is fabricated and measured, exhibiting a 1.22% bandwidth at 1.97 GHz *with an isolation of greater than 22 dB, having a very small device size of 0.021 mm^2 .*

CHAPTER I

Introduction

1.1. Dissertation Motivation

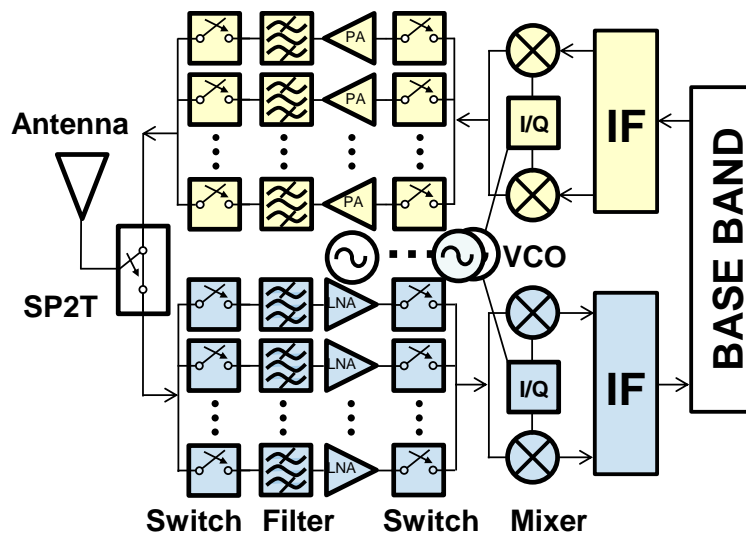
Multi-standard smartphones have become ubiquitous in everyday life. Such systems operate under different communication standards (Bluetooth, Global Positioning Systems-GPS, Global System for Mobile communications-GSM, WLAN, 3G, 4G Long-Term Evolution-LTE, etc.) that operate at different frequencies. Moreover, software-defined and cognitive radios need to quickly change their operating frequency for counteracting the negative impact of environmental conditions of fading, jamming, and interference in order to provide the reliable communication, and/or for concurrently utilizing the available channels within users so as to overcome limited frequency resources. Therefore, frequency agility plays a critical role in modern wireless communication systems. It is essential to implement simple yet high-performance, *frequency reconfigurable* RF front-ends for the next generation of radios.

In order to implement reconfigurable devices, the current technology relies on utilizing solid-state/MEMS switches connected to a large number of filters and/or tunable components such as variable capacitors or varactors within devices. The next generation

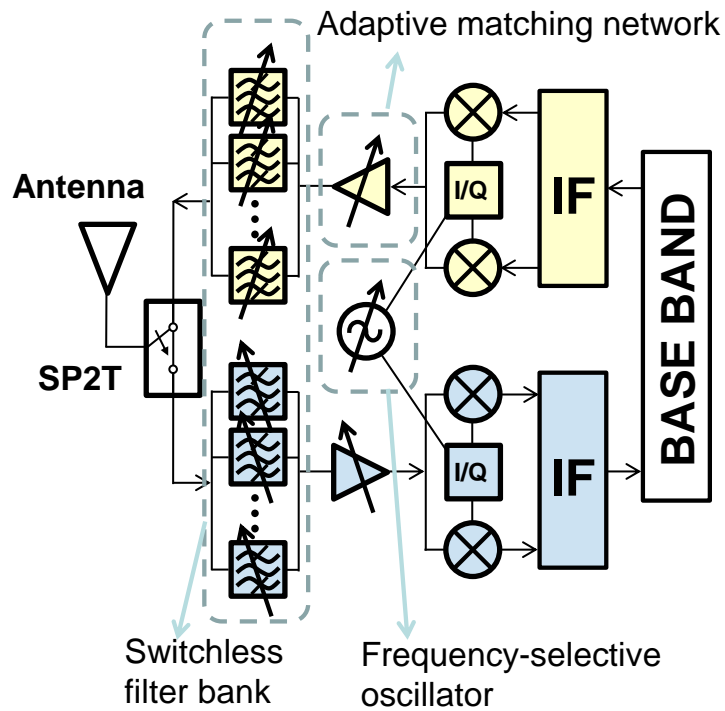
of smartphones is expected to accommodate a large number of frequency bands. This condition leads to an increase in the required number of switches and/or tunable components, making such systems more complex and costly.

One of the alternative and promising approaches for the development of reconfigurable RF front-ends is to utilize ferroelectric materials such as barium strontium titanate ($\text{Ba}_x\text{Sr}_{1-x}\text{TiO}_3$, BST). The ferroelectric BST material in its paraelectric phase exhibits electric-field-induced piezoelectricity (electrostriction). This interesting property enables the design of switchable ferroelectric BST acoustic resonators such as FBARs (thin film bulk acoustic resonators). The ferroelectric BST resonators are intrinsically switchable, with application of a dc bias voltage.

Since resonators are the key components of many RF devices such as filters, oscillators, and matching networks, the BST acoustic resonators can be used to simplify generic RF-front ends (Fig. 1.1(a)) by building reconfigurable RF devices such as switchless filter banks, frequency-selective oscillators, and adaptive matching networks for amplifiers (Fig. 1.1(b)). Of special interest for RF front-end components is RF filters. According to [1], sales of RF front-ends are expected to reach 18 billion US dollars by 2020 and RF filters are the driver for this business opportunity. Elimination of switches within the RF front-ends by embodying switchable filters would reduce the size, complexity, and cost of current communication systems considerably. This is the motivation behind the current dissertation on the design and modeling of ferroelectric BST FBARs for intrinsically switchable RF bulk acoustic wave filters.



(a)



(b)

Figure 1.1: (a) Generic RF front-end and (b) Proposed RF front-end based on switchable ferroelectric BST FBAR reconfigurable devices.

1.2. Background

The ferroelectric material utilized in this work is barium strontium titanate ($\text{Ba}_x\text{Sr}_{1-x}\text{TiO}_3$, BST). The multifunctional properties of ferroelectric BST in paraelectric phase including temperature and electric-field dependent characteristics allow for the design of BST based RF/microwave devices. Of special interest is the electric-field-induced piezoelectric effect known as electrostriction, which enables BST acoustic resonators to be intrinsically switchable. By utilizing such resonators, intrinsically switchable RF bulk acoustic wave filters can be designed. This section discusses the temperature-dependent BST properties, electric-field-dependent permittivity in thin film BST, electric-field-induced piezoelectricity in thin film BST, switchable BST film bulk acoustic resonators (FBARs), and frequency response of switchable BST FBARs.

1.2.1. BST Operation in Paraelectric Phase

The BST material exhibit two distinctive characteristics depending on their operating temperature with respect to the Curie temperature (T_c) as seen in Figure 1.2 [2]. Below their T_c the BST material are in *ferroelectric* phase and exhibit memory effects or hysteresis, making them suitable for memory applications such as non-volatile memories (FeRAM) [2]-[4]. By contrast, above their T_c , the BST material are in *paraelectric* phase and possess high permittivities ($\epsilon_r > 100$) and electric-field-dependent properties. Therefore, BST in paraelectric phase is suitable for RF/microwave device applications such as high-k capacitors/varactors and acoustic resonators [2]-[4].

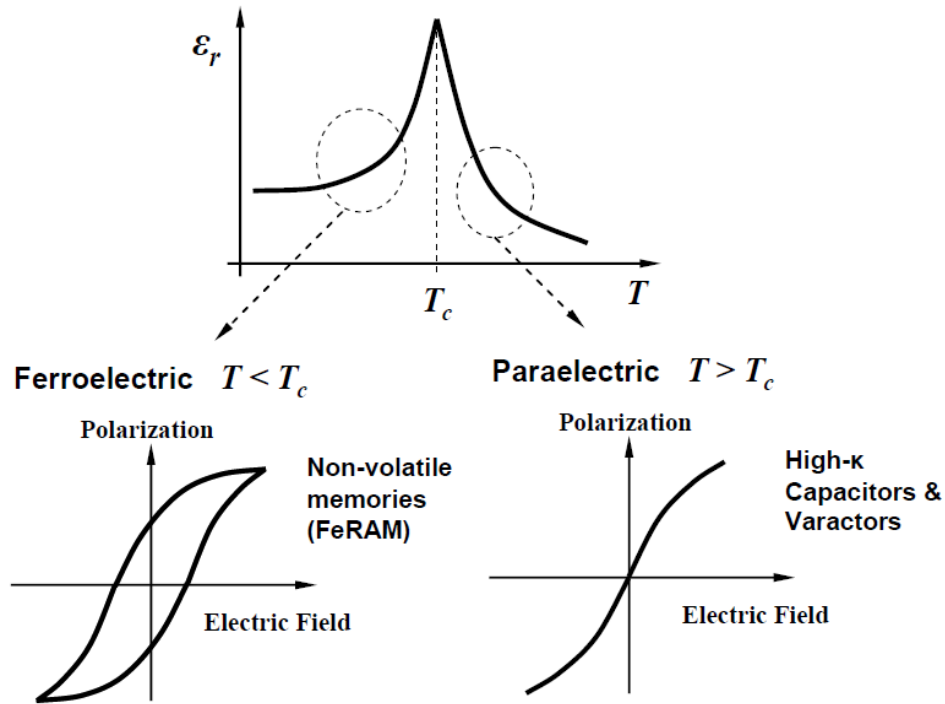


Figure 1.2: Temperature dependent response of ferroelectric BST material in its ferroelectric phase (below T_c) and its paraelectric phase (above T_c) (reproduced from [2]).

The T_c of the BST can be changed by modifying the chemical composition ratio between barium (x) and strontium ($1-x$). Figure 1.3 shows the temperature dependent dielectric constant characteristic of $Ba_xSr_{1-x}TiO_3$ ceramics with the different composition of x . Since this dissertation focuses on reconfigurable RF devices based on acoustic resonators, the paraelectric phase operation at room temperature is preferred and it is achieved by choosing x to be smaller than 0.7 as seen in Figure 1.3. Throughout this dissertation, the $Ba_{0.5}Sr_{0.5}TiO_3$ composition ($T_c \sim 250$ K) is used which is the most commonly utilized composition in BST thin film for the design of varactors and acoustic resonators [2]-[4].

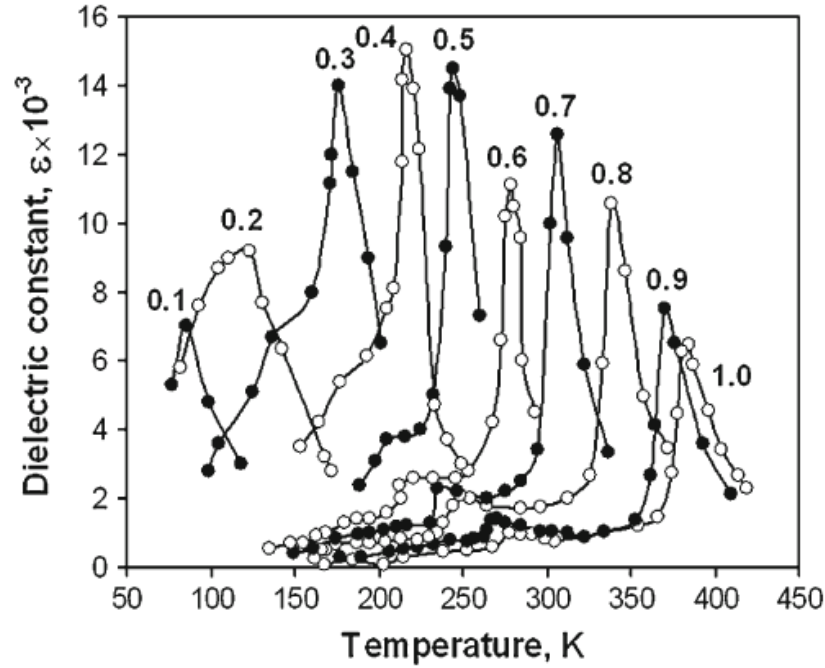


Figure 1.3: Temperature dependent dielectric constant characteristic of $Ba_xSr_{1-x}TiO_3$ ceramics with the different composition of x (reproduced from [4]).

1.2.2. Electric-Field-Dependent Permittivity

BST in its paraelectric phase exhibits an electric-field-dependent permittivity. This property has been extensively used to design BST-based varactors [5]-[11]. A typical response of a BST capacitor as a function of dc bias voltage is provided in Figure 1.4. Capacitance is maximized at zero dc electric field (zero bias voltage) and gradually decreases with the applied dc electric field (dc bias voltage). Its high permittivity, high tunability, and low loss-tangent characteristics make the BST varactors attractive for the design of small-size low-loss tunable RF devices such as tunable filters and phase shifters [2]-[11].

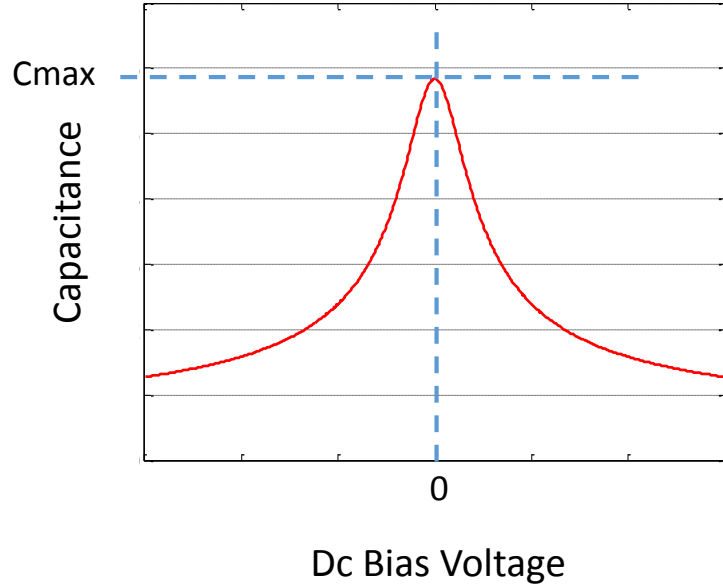


Figure 1.4: Bias voltage dependent capacitance of BST varactors.

1.2.3. Electric-Field-Induced Piezoelectricity (Electrostriction)

BST material exhibits electric-field-induced piezoelectricity known as electrostriction. This property has been recently investigated to design intrinsically switchable BST acoustic resonators (FBARs in [12]-[43] and SMRs in [44]-[54]). At zero dc electric field, the effective piezoelectric coefficient (e) of BST material is near zero and the strain (S) and stress (T) are not coupled with the electric field (E) and electric displacement (D):

$$T = c^E(E) \cdot S - e(E) \cdot E = c \cdot S \quad \text{for } E=0 \quad (1-1)$$

$$D = e(E) \cdot S + \varepsilon^S(E) \cdot E = \varepsilon \cdot E \quad \text{for } E=0 \quad (1-2)$$

These conditions lead to zero electromechanical coupling coefficient.

$$K_t^2(E) = \frac{e(E)^2}{e(E)^2 + c^E(E)\varepsilon^S(E)} = 0 \quad \text{for } E=0 \quad (1-3)$$

In (1-1) and (1-2), c^E and ε^S denote the stiffness constant with E and permittivity with S . On the other hand, as the applied dc electric field increases, the electric-field-induced piezoelectric coefficient ($e(E)$) increases due to its strong electrostrictive effect, providing energy conversion between the electrical domain and mechanical domain [3], [4].

$$T = c^E(E)S - e(E)E \quad (1-4)$$

$$D = e(E)S + \varepsilon^S(E)E \quad (1-5)$$

Therefore, the electromechanical coupling coefficient increases with the applied dc electric field and is a function of the applied dc electric field.

$$K_t^2(E) = \frac{e(E)^2}{e(E)^2 + C^E(E)\varepsilon^S(E)} \quad (1-6)$$

This property makes BST based acoustic resonators suitable for designing intrinsically switchable RF devices such as resonators and filters. Figure 1.5 shows the measurement results for the effective electromechanical coupling coefficient in a 1-port

BST FBAR [36]. At zero bias voltage, the device is in the off-state, leading to zero coupling coefficient. As bias voltage increases, the device is in its on-state, thus the electromechanical coupling coefficient increases with a dc bias suitable for the implementation of switchable FBAR filters. In contrast, the piezoelectric AlN and ZnO material exhibit the constant electromechanical coupling coefficient of 6.5% and 8.5% [55], and therefore they cannot be used for intrinsically switchable resonators.

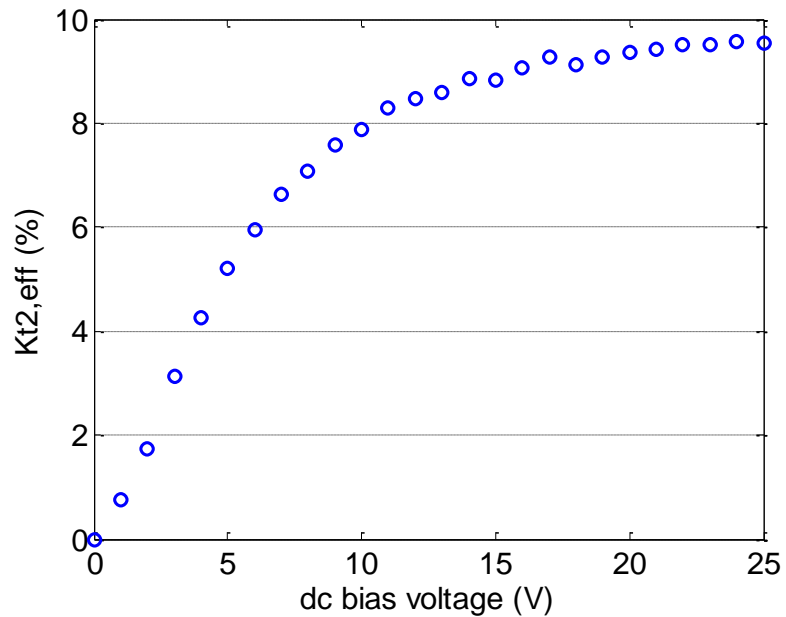


Figure 1.5: Measurement results of dc-bias voltage dependent electromechanical coupling coefficient for a 1-port BST FBAR [36].

1.2.4. BST Acoustic Resonators

BST material's electrostrictive effect is exploited for the development of reconfigurable devices based on the BST acoustic resonators. This research concentrates on the design and fabrication of BST based film bulk acoustic resonator (FBAR) structures.

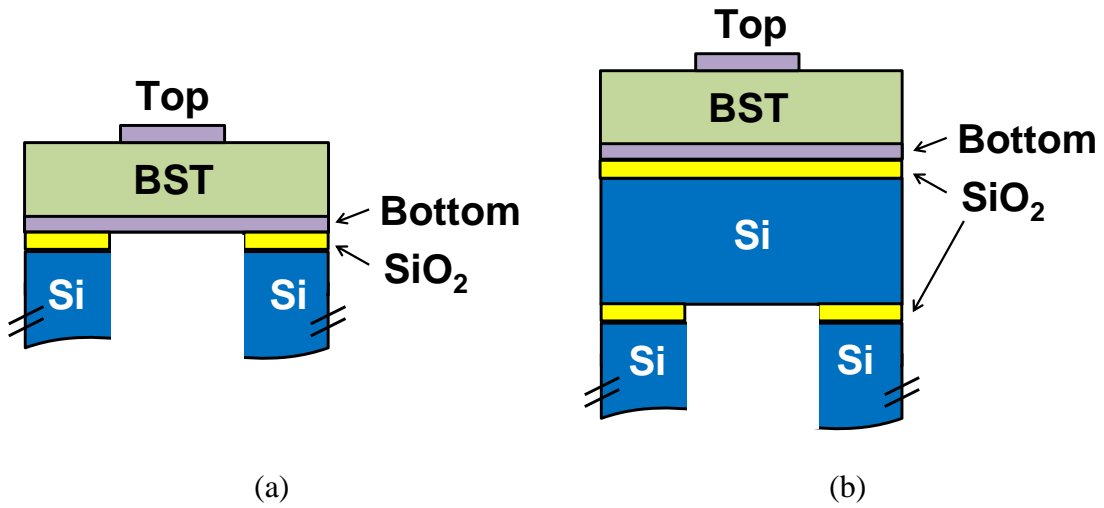


Figure 1.6: Cross-sectional view of (a) a BST FBAR and (b) a BST-on-Si composite FBAR.

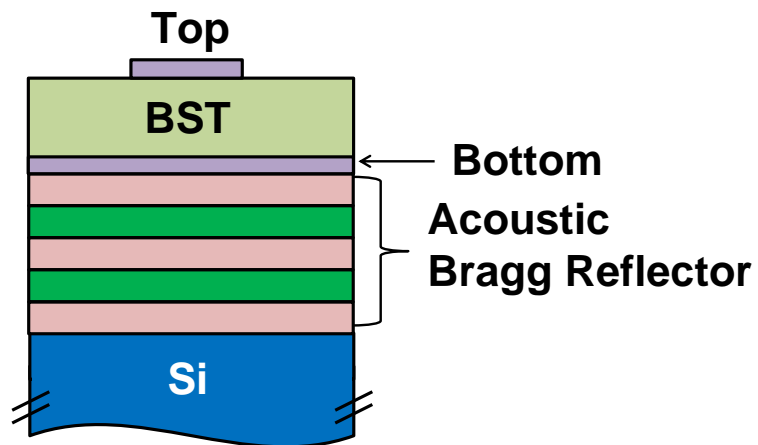


Figure 1.7: Cross-sectional view of a BST SMR.

The BST FBAR structure consists of a thin film BST layer sandwiched between the top and bottom electrodes (Figure 1.6(a)). The BST layer is used as an electromechanical transduction layer which converts mechanical energy into electrical energy, and vice versa. The transduction mechanism in ferroelectric BST FBAR is through

electrostriction, which is the electric field induced piezoelectric effect [3], [4]. The top and bottom electrodes are used to apply the dc and RF signals. The BST-on-Si composite FBAR structure can be made by addition of a low-mechanical-loss silicon layer underneath the bottom electrode (Figure 1.6(b)) in order to tailor FBAR characteristics such as the device quality factor and electromechanical coupling coefficient [23]-[24].

The substrate underneath the FBAR and composite FBAR is released as seen in Fig. 1.6. Since the FBAR is isolated from the substrate, there is no energy leaking into the substrate, leading to high device quality factors. The high quality factor of the FBAR is a great advantage over the SMR (solidly mounted resonator). In SMRs, the acoustic Bragg reflectors are used to reflect the acoustic energy. FBAR filters provide better performance as compared to SMR filters [56], and thus FBAR filters have become prevalent in today's smartphones [56].

1.2.5. Frequency Response of Switchable BST FBARs

A simple FBAR or composite FBAR behaves as an intrinsically switchable resonator controlled by a dc bias voltage across the thin film BST. A typical frequency response of a BST FBAR is provided in Fig. 1.8 showing their switchable property in on-state and off-state. f_s and f_p in Fig. 1.8 denote series and parallel resonance frequencies, respectively. The simple linear mBVD model and capacitor model in Fig. 1.9 are utilized for a switchable BST FBARs when the resonator is in its on-state and off-state, respectively.

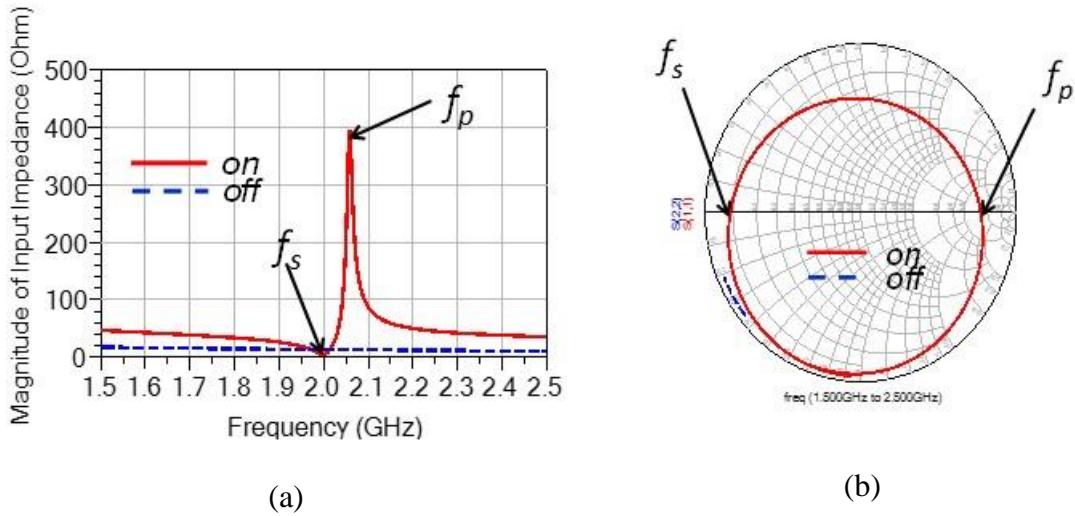


Figure 1.8: Typical frequency responses of BST FBARs with (on) and without (off) the applied dc bias voltage. (a) Magnitude of input impedance and (b) reflection coefficients on the Smith chart when the switchable resonator is in its on- and off-states.

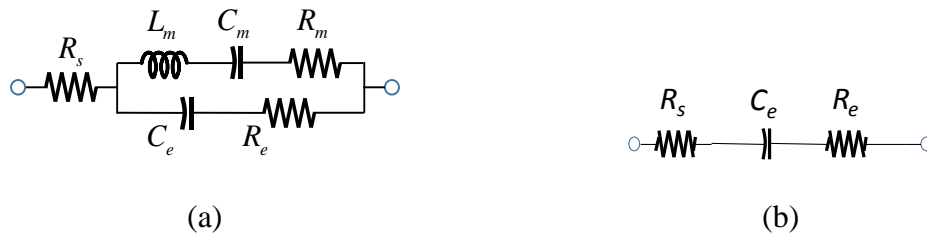


Figure 1.9: (a) mBVD circuit model and (b) capacitor model applicable when the switchable resonator is in on- and off-states, respectively.

In Fig. 1.9(a), the motional branch is modeled by the capacitor C_m in series with the inductor L_m forming the series resonator. The mechanical loss factor is represented by R_m . The electrical branch consists of the static capacitance C_e along with the dielectric loss factor R_e . The combination of the motional and electrical branches determine the parallel resonance frequency. The ohmic resistance R_s due to the device electrodes and

interconnects is incorporated into the model. In Fig. 1.9(b), the motional branch components (L_m, C_m, R_m) vanish since no acoustic resonance can be excited.

In addition to their switchable properties, BST FBARs possess other favorable properties for RF applications. The high permittivity of ferroelectric materials ($\epsilon_r > 100$) allows for reducing the size of devices; for example, a typical BST resonator area and BST filter area is in the order of 0.001 mm^2 and 0.01 mm^2 , respectively, at low GHz frequencies in standard $50\text{-}\Omega$ RF systems. In fact, the resonator size is smaller by a factor of more than 10 as compared to conventional AlN resonators [3], [4]. Moreover, the power consumption in a BST FBAR itself is negligible even with a dc bias voltage across the device due to a very small leakage current in thin film ferroelectric BST [3], [4].

1-3. Dissertation Goal and Organization

The goal of this dissertation is to design, simulate, characterize, and model ferroelectric BST FBARs for intrinsically switchable RF bulk acoustic wave filters. First, a nonlinear circuit model for BST FBARs is developed based on physics of BST's strong electrostrictive effect to predict dc-bias-voltage and RF-power-level dependent behavior of intrinsically switchable BST FBARs, as well as to characterize ferroelectric BST FBARs. Subsequently, the design methods for BST-on-Si composite FBARs are provided based on 1-D acoustic transmission line model and 2-D Multiphysics simulations. Temperature-dependent properties for BST FBARs are characterized and the method for lateral-wave spurious-modes elimination in BST FBARs is presented. Finally, the design method for switchable FBAR filters is presented. For the first time, a complete set of equations for the

design of ladder-type BAW filters is developed based on the image parameter method, which enables BAW filter designers to accurately predict filter behavior.

The organization of this dissertation is as follows. Chapter 2 will focus on the development of a nonlinear model for intrinsically switchable BST FBARs that can be utilized to predict and improve the linearity levels of switchable ferroelectric FBAR components. Due to the strong electrostrictive effect, measurement results for BST FBARs show voltage-dependent nonlinear characteristics including the voltage-dependent series and parallel resonance frequencies, electromechanical coupling coefficient, and impedance levels. In order to predict linearity levels such as intermodulation distortion, harmonics, and gain compression of an intrinsically switchable BST FBAR filter, the development of a simple yet accurate circuit model is essential. Based on the physics behind the BST FBAR nonlinearity, each component of modified Butterworth–Van Dyke (mBVD) circuit model, which was originally developed for piezoelectric materials, is modified to predict its voltage-dependent behavior as a function of the applied voltage across the BST FBAR. The developed physics-based model is then implemented in a circuit simulator for easier resonator and filter simulation. Dc-bias-voltage dependent, as well as RF-power-level dependent simulation results for the 1-port BST FBAR are provided and compared with the measurement results. The measured and modeled results are in close agreement, validating the developed physics-based nonlinear model for intrinsically switchable ferroelectric BST FBAR devices.

Chapter 3 will focus on the design of intrinsically switchable BST-on-Si composite FBARs that are the basic component of FBAR filters. First, composite FBARs are designed to have high quality factors, which is suitable for the design of low-phase-noise oscillators,

as well as narrow-bandwidth filters. The temperature-dependent characteristics of high- Q BST FBARs are investigated to examine their temperature stability as it is very important in the design of frequency-reference applications. Measured temperature coefficients of frequency (TCF) for both series and parallel resonance frequencies, as well as the variation in electromechanical coupling coefficient and quality factor with temperature are provided. Second, general composite FBARs are designed for the maximum electromechanical coupling coefficient, which is important for the design of low-insertion-loss and wider-bandwidth FBAR filters. Furthermore, the method of eliminating lateral-wave spurious-modes in BST FBARs is presented to improve its quality factors and electromechanical coupling coefficient. A raised frame technique, which has been utilized for piezoelectric BAW resonators to eliminate lateral-wave spurious-modes, is first employed in the design of spurious-free switchable ferroelectric BST FBARs.

Chapter 4 will focus on the design of intrinsically-switchable radio-frequency bulk acoustic wave filters based on ferroelectric FBARs. For the first time, *a design method for ladder-type bulk acoustic wave filters* based on popular RF/microwave filter synthesis method using image parameters is presented. Not only the calculation of image impedance for filter's impedance matching, but also the calculation of propagation constant for filter's bandwidth control are performed for the first time. The developed complete set of design equations can be utilized in the design of *any ladder-type acoustic filter regardless of materials employed (i.e. piezoelectric or ferroelectric)*. Since the filter synthesis is based on a unit cell in a ladder-type acoustic filter, the unit cell can be easily cascaded to control the filter's rejection level. Moreover, the proposed filter synthesis allows for the accurate prediction of the filter insertion loss. Therefore, the filter response can be accurately

predicted and performance trade-offs involved can be easily investigated allowing for systematic filter design and minimization of optimization iterations in filter design. As an experimental verification, a pi-type ladder-type BAW filter at 2 GHz with a 1.33% fractional bandwidth is designed, fabricated, and measured based on composite FBARs with a 4% $K_{t,eff}^2$ presented in Chapter 3. The measurement results for the designed and fabricated ladder-type BST FBAR filter exhibits excellent agreement with the predicted circuit-simulation results, validating the proposed ladder-type BAW filter synthesis method based on image parameters.

Chapter 5 will summarize this work and present the future direction of BST FBAR based switchable resonators and filters. Finally, journal and conference publications out of this work will be listed.

CHAPTER II

Nonlinear Behavior and Circuit Modeling of Intrinsically Switchable Ferroelectric BST FBARs

2.1. Chapter Motivation

Ferroelectric thin films in paraelectric phase possess electric-field-dependent permittivity, as well as electric-field-induced piezoelectricity. In the absence of an external electric field, thin film ferroelectrics' piezoelectric coefficient is near zero. With the introduction of an electric field through application of a dc bias voltage, they exhibit an electric-field-induced piezoelectric effect (electrostriction). As the magnitude of electric field increases, the material's permittivity decreases while its effective piezoelectric coefficient increases. These properties have led to a growing interest in ferroelectric based tunable devices such as varactors, and more recently switchable thin film bulk acoustic resonators (FBARs) for frequency-agile circuits.

To design ferroelectric based reconfigurable circuits, an accurate yet simple, nonlinear circuit model is necessary. A nonlinear circuit model for piezoelectric AlN FBARs has already been developed [57]-[59], but the model cannot be directly applied to ferroelectric BST FBARs. This is because for ferroelectric BST FBARs nonlinearity is

responsible for their strong electrostrictive effect, which is different from the source of nonlinearity in typical piezoelectric devices. A nonlinear circuit model has been developed for ferroelectric BST varactors developed in [9], [10], however this model does not model electrostriction in the material. A theoretical model, based on the Landau-Free-Energy expansion, has been developed for ferroelectric BST acoustic resonators [16]-[18], but the model is not very practical in the design of switchable BST devices as it cannot be easily implemented in commercial circuit simulators. Therefore, the theoretical model has not been utilized for the study of ferroelectric switchable BST FBAR behavior in filters, duplexers, and oscillators. It is highly required to develop a simple yet accurate, nonlinear circuit model for ferroelectric BST FBARs to fully investigate nonlinear behavior of switchable BST FBAR devices to assess linearity levels of the devices, and device approaches for improving their linearity levels if required.

In this chapter, measurement of S parameters for a BST FBAR at different dc bias voltages and RF power levels are provided. The bias voltage dependent resonator characteristics such as capacitance, resonance frequencies, effective electromechanical coupling coefficient, and admittance and impedance levels at series and parallel resonance frequencies are investigated. A linear modified Butterworth-Van Dyke (mBVD) model, which is originally developed for piezoelectric materials, is employed to develop a *nonlinear mBVD model* for voltage-dependent intrinsically switchable ferroelectric BST FBARs. Nonlinear model parameters in the developed nonlinear model are easily measurable, so they can be extracted from simple S parameter measurements at different bias voltages. The developed nonlinear model is implemented in a circuit simulator such as ADS. Dc bias voltage and RF power level dependent simulation results for the fabricated

FBAR are in excellent agreement with the measurement results, validating the physics-based BST FBAR modeling procedure.

2.2. Fabrication Procedure and Measurements of Ferroelectric BST FBARs

A ferroelectric BST FBAR is an acoustically resonant cavity that consists of a ferroelectric thin film sandwiched between two electrodes. FBARs have both series and parallel resonances, the frequencies of which are determined by the device thickness and acoustic properties. The frequency response can be predicted either through analytical approach (1-D acoustic transmission line model) [60] or by using multi-physics simulators such as Comsol Multiphysics [61].

Ferroelectric FBARs are fabricated using micromachining technology. Figure 2.1 shows the cross section of a ferroelectric BST FBAR at each fabrication step. Fabrication begins with a high-resistivity silicon (Si) wafer with layers of silicon dioxide (SiO_2), titanium dioxide (TiO_2), and platinum (Pt) that are 500, 40, and 150 nm thick, respectively (Fig. 2.1(a)). The Pt is patterned using photolithography and etched with aqua regia (1:3, $\text{HCl}:\text{HNO}_3$, heated to 50 °C) to form the bottom electrode (Fig. 2.1(b)). A layer of BST is then deposited to be 700 nm on the patterned substrate by pulsed laser deposition (PLD) with a KrF excimer laser (248-nm wavelength, 25-ns pulse width, 10-Hz pulse repetition rate, 1.75-J/cm² energy density), in 300 mTorr oxygen environment, and at a substrate temperature of 650 °C (Fig. 2.1(c)). A 100 nm layer of Pt is deposited on the BST layer using e-beam evaporation and liftoff to form the top electrode (Fig. 2.1(d)). Layers of

aluminum (Al) and gold (Au) with thicknesses of 500 nm are also deposited using e-beam evaporation to form the probe pads for testing the device (Fig. 2.1(e)). The last processing step is to etch the thick Si substrate from beneath the device using deep reactive ion etching (DRIE) to release the device (Fig. 2.1(f)).

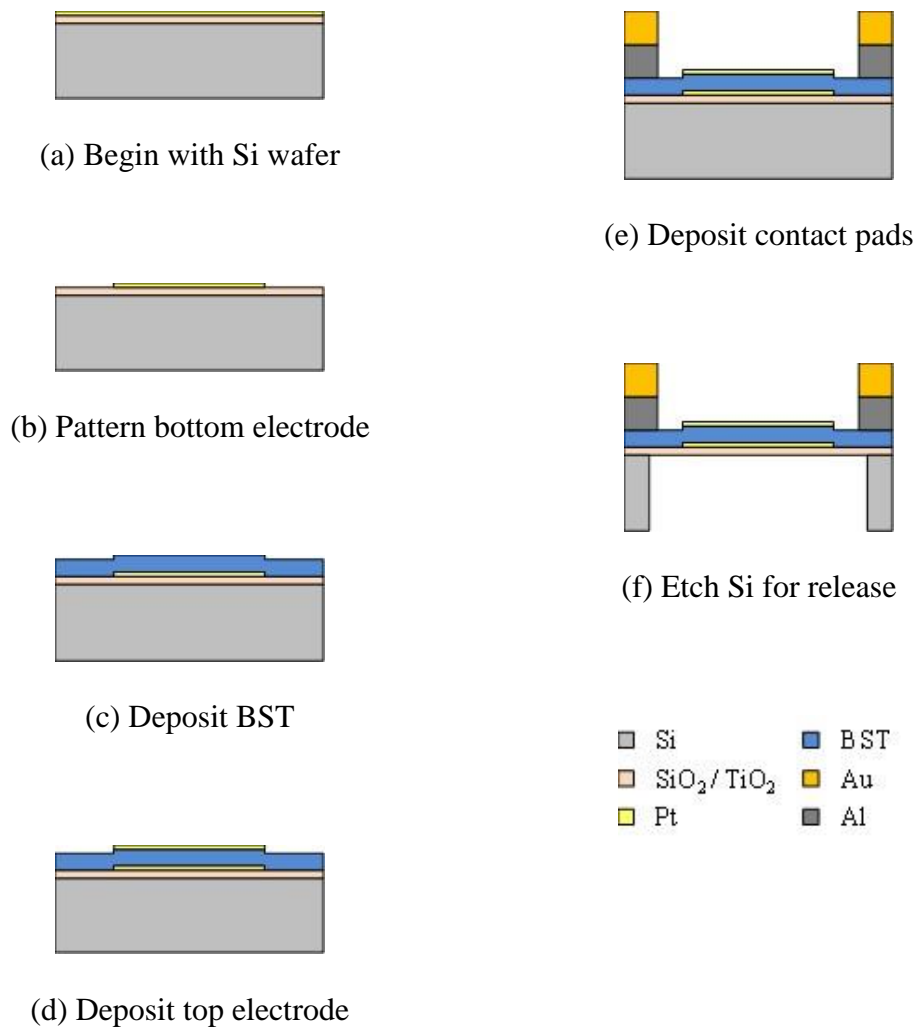


Figure 2.1: Fabrication procedure for ferroelectric BST FBARs.

Figure 2.2 shows a photograph of a typical BST FBAR that has been fabricated. The fabricated intrinsically switchable 1-port BST FBARs are measured using 150- μm pitch ground-signal-ground (GSG) probes. The measurement setup for dc-bias-voltage and RF-power-level dependent S parameters of the fabricated BST FBARs are shown in Fig. 2.3. Measurements are performed with an Agilent E8364C network analyzer from 100 MHz to 3 GHz. During the measurements, the dc bias voltage, which is provided by a dc power supply and a bias tee, is swept from 0 to 25 V while the RF power available from the source (P_{avs}), which is set by the network analyzer, is varied from -18 to 9 dBm. The dc-bias-voltage and RF-power-level measurement results for BST FBARs are provided in the following section.

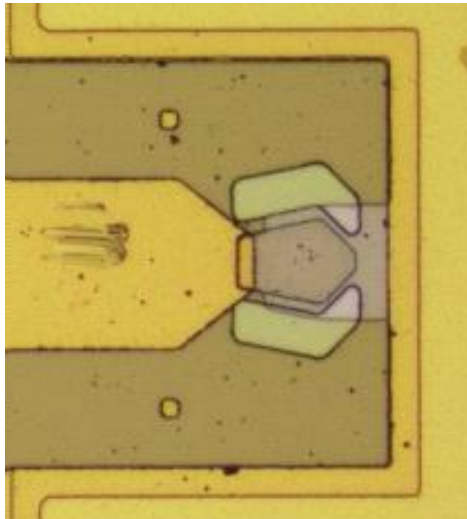


Figure 2.2: A photograph of a typical BST FBAR that has an area of $650 \mu\text{m}^2$. The device was fabricated using pulsed laser deposition (PLD).

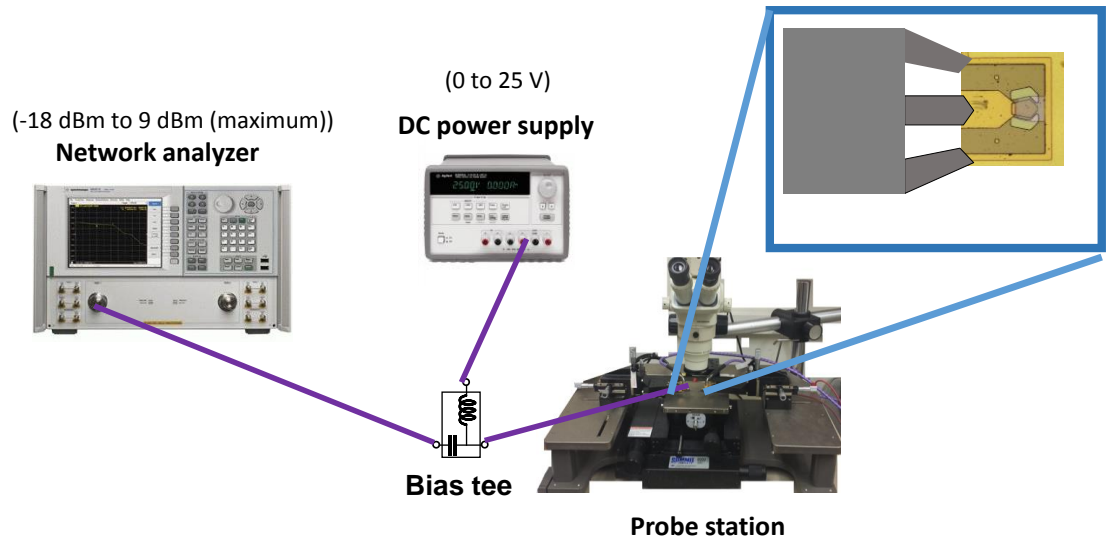


Figure 2.3: Measurement setup for dc-bias-voltage and RF-power-level dependent S parameters of a fabricated intrinsically switchable 1-port BST FBAR.

2.3. DC-Bias-Voltage and RF-Power-Level Dependence of Intrinsically Switchable Ferroelectric BST FBARs

Figures 2.4, 2.5, and 2.6 show the measured capacitance, electromechanical coupling coefficient, and series and parallel resonance frequencies, respectively, for a BST FBAR as a function of dc bias voltage. As can be seen, all parameters are dc-bias-voltage dependent. Especially, electromechanical coupling coefficient is a strong function of bias voltage, which is a very unique characteristic for intrinsically switchable ferroelectric BST FBARs. This property can be utilized to build reconfigurable RF front-end components such as switchable RF FBAR filters and oscillators. Since these parameters are bias-voltage

dependent, the linear models for BST FBARs in Fig. 1.9 for their on and off states cannot be utilized to predict device voltage-dependent behavior.

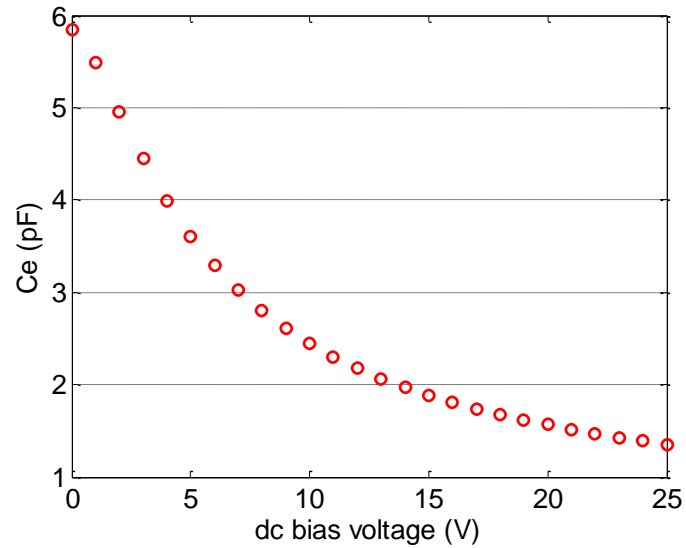


Figure 2.4: Measured capacitance for a BST FBAR as a function of dc bias voltage.

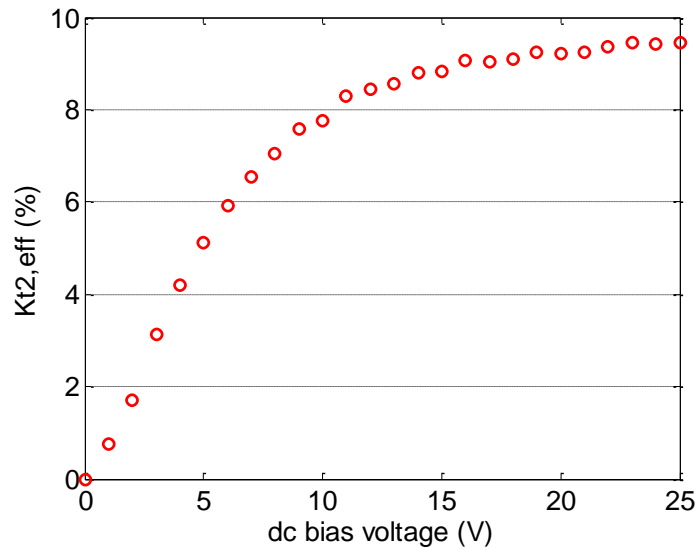


Figure 2.5: Measurement results of electromechanical coupling coefficient for the fabricated 1-port BST FBAR as a function of dc bias voltage.

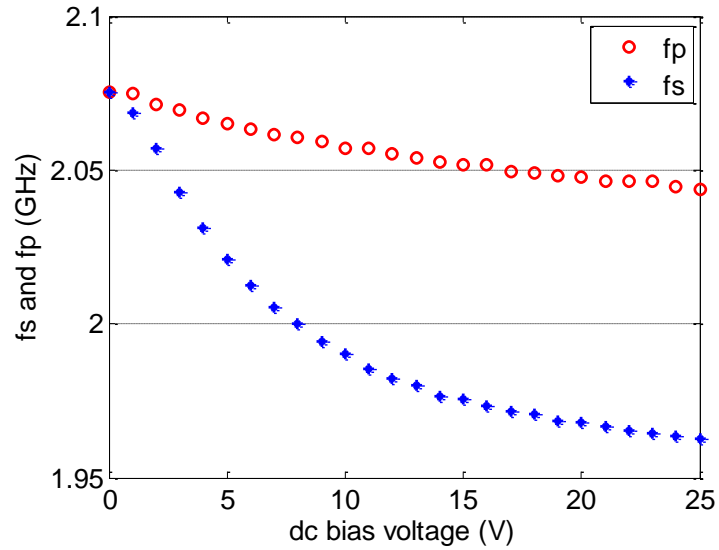


Figure 2.6: Measurement results of resonance frequencies for the fabricated 1-port BST FBAR as a function of dc bias voltage.

Figures 2.7 and 2.8 show the real part of input admittance at series resonance frequency and real part of input impedance at parallel resonance frequency, which are also a strong function of dc bias voltage. For an ideal device (lossless), the input admittance at a series resonance frequency and input impedance at a parallel resonance frequency become infinite. So, finite values of these parameters indicate the device loss characteristics, which should be modeled accurately so as to investigate filter insertion loss or oscillator phase noise.

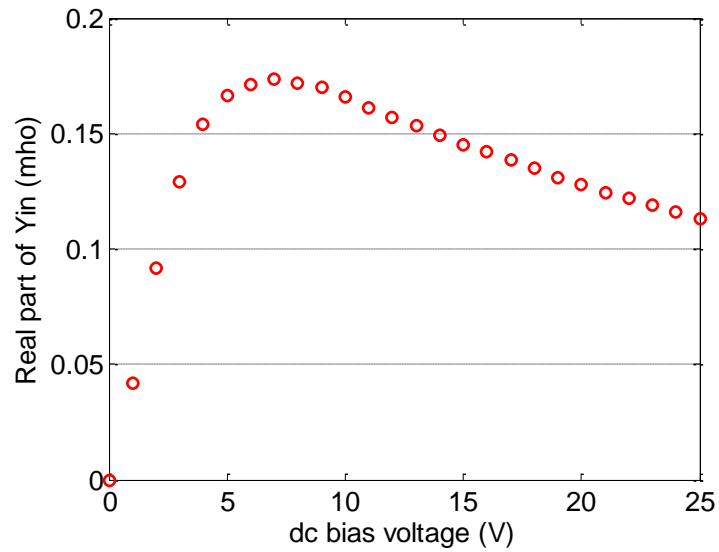


Figure 2.7: Measurement results of real part of input admittance at the series resonance frequency for the fabricated 1-port BST FBAR as a function of dc bias voltage.

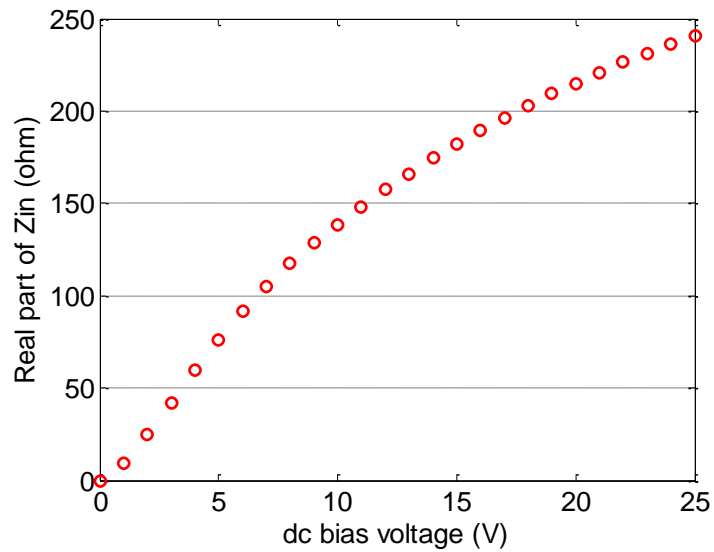


Figure 2.8: Measurement results of real part of input impedance at the parallel resonance frequency for the fabricated 1-port BST FBAR as a function of dc bias voltage.

In addition to parameters shown above, it is worthwhile to carefully examine the quality factor (Q) and effective electromechanical coupling coefficient ($K_{t,eff}^2$) for BST FBAR device design. Achieving high Q is critical for the design of low-phase-noise oscillators and low-insertion-loss FBAR filters. Furthermore, large $K_{t,eff}^2$ is required for the design of FBAR filters to satisfy bandwidth requirements in mobile communications applications [62]. In general, there is a tradeoff between these two FOMs, and depending on the application, one figure of merit can be favored over the other [62]. The equations used for calculating Q and $K_{t,eff}^2$ are provided below [60]:

$$Q = \frac{f}{2} \left| \frac{d\phi_{Zin}}{df} \right|_{f=f_s, f_p} \quad (2-1)$$

$$K_{t,eff}^2 = \frac{\pi f_s}{2 f_p} \tan \left(\frac{\pi (f_p - f_s)}{2 f_p} \right) \quad (2-2)$$

where f is the frequency and ϕ_{Zin} is the phase of the input impedance. The variables f_s and f_p denote the series and parallel resonance frequencies, respectively. The resonance frequencies f_s and f_p are determined at frequencies where the input conductance (real part of input admittance) and input resistance (real part of input impedance) are maximized [36]. The Q and $K_{t,eff}^2$ are obtained from the measurement results after de-embedding the parasitic series resistance and series inductance as described in [15], [36], [47].

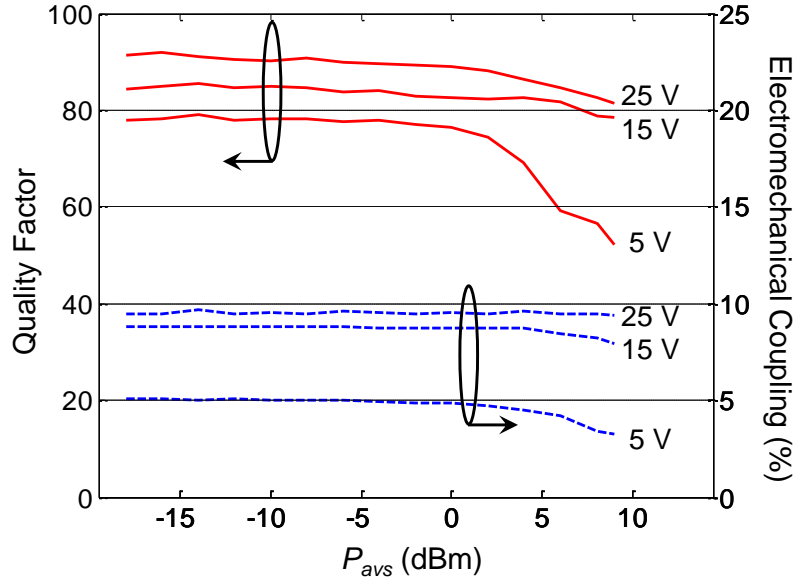


Figure 2.9: $K_{t,eff}^2$ and Q of the BST FBAR as a function of P_{avs} with different applied dc bias voltages.

The Q and $K_{t,eff}^2$ of a 2 GHz FBAR measured under the conditions discussed in the previous section (-18 to 9 dBm P_{avs} , 0 to 25 V $_{dc}$) are shown in Fig. 2.9. As the applied dc bias voltage increases, $K_{t,eff}^2$ increases. The behavior is consistent with the observations reported in the literature [45], [47], [50]. At 25 V dc bias, a $K_{t,eff}^2$ of more than 9% is obtained, which is the highest value that has been reported so far for BST FBARs (7% in [12]). This is also higher than $K_{t,eff}^2$ of piezoelectric AlN FBARs (6.9% in [55]). The tunability of the BST FBAR, defined by (2-3) and (2-4) [18]

$$n_s = \frac{f_s(V_{dc}) - f_s(0V)}{f_s(0V)} \quad (2-3)$$

$$n_p = \frac{f_p(V_{dc}) - f_p(0V)}{f_p(0V)} \quad (2-4)$$

is relatively high: -4.02% for f_s and -0.81% for f_p at 10 V and -5.11% for f_s and -1.26% for f_p at 20 V. These values are higher than previously reported results for BST FBARs (-2.4 % for f_s and -0.6% for f_p in [18]), which can be attributed to the fact that $\text{Ba}_{0.5}\text{Sr}_{0.5}\text{TiO}_3$ has higher tunability than $\text{Ba}_{0.25}\text{Sr}_{0.75}\text{TiO}_3$ due to intrinsic material properties [18], [49]. It is worthwhile to mention that BST FBARs based on the BST-on-silicon composite structures with mechanical *Quality factors as high as 970 at 2.5 GHz* have also been demonstrated (Chapter 3). In addition to the dc-bias-voltage dependent behavior of BST FBAR, its RF-power-level dependent behavior has also been studied. Figure 2.9 shows that as the P_{avs} increases, Q and $K_{t,eff}^2$ begin to notably deviate from the small signal values. However, at larger dc bias voltages, Q and $K_{t,eff}^2$ are less dependent on the applied RF power levels.

The behavior of FBAR's impedance variation as a function of RF power level can also be observed from the measured S parameters plotted on the Smith chart (Fig. 2.10). The measurement results show that at both 5 V and 25 V dc bias, the reflection coefficients begin to deviate from the small signal values as power level increases. However, the impedance variation at 25 V dc bias is significantly smaller. Based on these measurement results in Figs. 2.9 and 2.10, it can be concluded that dc bias voltages that provide high K_t^2 should be applied to minimize nonlinear behavior of ferroelectric FBARs at higher power levels. This can be attributed to measured performance in Fig. 2.4 to Fig. 2.8 in which parameters changes more linearly at higher bias voltages as compared to lower bias voltages.

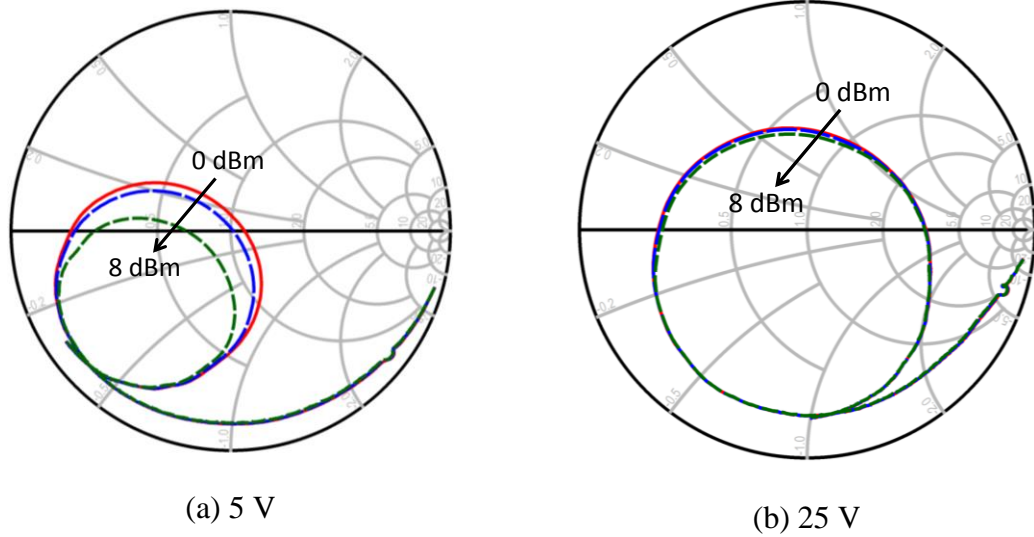


Figure 2.10: Measurement results of reflection coefficients for the BST FBAR on the Smith chart (100 MHz to 3 GHz) at a dc bias voltage of (a) 5 V and (b) 25 V with P_{avs} of 0, 4, and 8 dBm.

In the following sections, modeling procedures for the BST FBAR discussed in this section are presented.

2.4. Nonlinear Circuit Modeling of Intrinsically Switchable Ferroelectric BST FBARs

2.4.1. Existing Nonlinear Circuit Model for Capacitance $C_e(V)$

For simplicity, a lossless nonlinear circuit model is developed first, and then device losses are incorporated into the nonlinear model to accurately predict the device impedance levels. Figure 2.11 shows a schematic of lossless nonlinear model for intrinsically switchable ferroelectric BST FBARs in which parameters C_e , L_m , and C_m are a function of applied voltage.

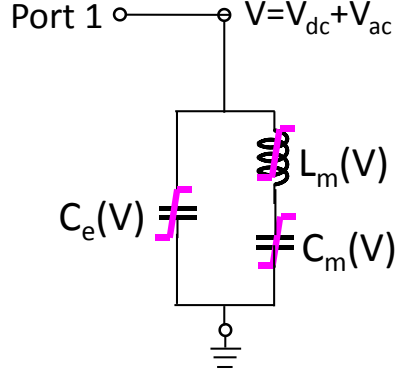


Figure 2.11: A schematic of lossless nonlinear model for intrinsically switchable ferroelectric BST FBARs. Parameters C_e , L_m , and C_m are a function of applied voltage.

The nonlinear circuit model for electrical capacitance C_e in Fig. 2.11 has been already developed in [9], and can be utilized in nonlinear modeling of ferroelectric BST FBARs. The modeling starts from the Landau-Devonshire-Ginzbur (LDG) model in the context of ferroelectric films in (2-5) [9].

$$E = \alpha_1 D + \alpha_3 D^3 \quad (2-5)$$

In (2-5), α_1 is the inverse of the zero-bias permittivity and α_3 the nonlinearity of the material [9]. A simple yet effective circuit model for the nonlinearity of BST varactors has been developed [9].

$$C_e(V) = \frac{C_{\max} - C_f}{2 \cosh \left[\frac{2}{3} \sinh^{-1} \left(\frac{2V}{V_2} \right) \right] - 1} + C_f \quad (2-6)$$

where C_{\max} is the maximum capacitance obtained at zero bias voltage, C_f is the fringe capacitance, V is the applied voltage across the device in Fig. 2.11, and V_2 is the voltage at which C_e reaches to one half of C_{\max} value as shown in Fig. 2.12. This empirical circuit model is easy to use as the capacitance and voltage are easily measurable [9].

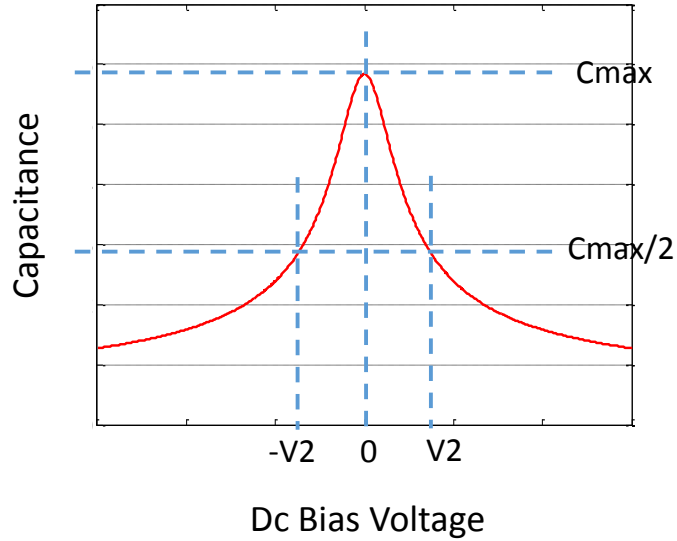


Figure 2.12: A typical capacitance-voltage curve for BST varactors.

2.4.2. Nonlinear Modeling of Electromechanical Coupling Coefficient $k_t^2(V)$

In [16]-[18], theoretical models for the dc bias dependence of induced acoustic resonances in paraelectric materials have been presented. The field-dependent piezoelectric constitutive equations is derived from the Landau Free Energy expansion [16]-[18]. As a result, theoretical models for electromechanical coupling coefficient, as well as resonance frequencies can be expressed as a function of material parameters. In this work, the models developed for the thickness-extensional mode in [16]-[18] are utilized. Detailed

information on the theoretical model can be found in [16]-[18]. The model for electromechanical coupling coefficient in [16]-[18] is provided in (2-7).

$$k_t^2(V) = \frac{e(V)^2}{c^D(V)\varepsilon(V)} \quad (2-7)$$

In (2-7), voltage-dependent piezoelectric constant ($e(V)$), stiffness constant at displacement D ($C^D(V)$), and ferroelectric material relative permittivity ($\varepsilon(V)$) can be expressed as a function of material parameters as follows [16]-[18].

$$e(V) = 2q\chi(V)P(V) \quad (2-8)$$

$$c^D(V) = c^0 \left(1 - \frac{m}{c^0} (P(V))^2 - \frac{e(V)^2 \varepsilon^b}{\chi(V) c^0 \varepsilon(V)} \right) \quad (2-9)$$

$$\varepsilon(V) = \chi(V) + \varepsilon^b \quad (2-10)$$

Ferroelectric part of the polarization P is a function of dielectric nonlinearity and voltage-dependent permittivity.

$$P(V)^2 = \frac{1}{3\beta} \left(\frac{1}{\varepsilon(V)} - \frac{1}{\varepsilon^0} \right) \quad (2-11)$$

$$\varepsilon(V) = \frac{1}{\alpha_1 + 3\beta(P(V))^2} \quad (2-12)$$

$$\varepsilon^0 = \frac{1}{\alpha_1} \quad (2-13)$$

The material parameters used in (2-7)-(2-13) [16]-[18] are summarized in Table 2.1.

Table 2.1
Field Variables and Material Parameters in (2-7)-(2-13)
for Thickness-Extensional Mode [16]-[18]

e	Piezoelectric coefficient	c^D	Stiffness (elastic) constant at D
ε	Permittivity of ferroelectric material	χ	Ferroelectric contribution to the susceptibility of the material
q	Linear electrostriction coefficient	P	Ferroelectric part of the polarization
c^0	Elastic constant at zero bias voltage	m	Nonlinear electrostriction coefficient
ε^b	Background permittivity	β	Dielectric nonlinearity coefficient
ε^0	Permittivity at zero bias	α_1	Inverse of permittivity at zero bias

Although these theoretical models are useful to understand the physics of electrostriction-based behavior of BST FBARs, models cannot be directly utilized in the circuit simulator, and necessary modification is required. By using some approximation, (2-9) and (2-10) can be simplified to (2-14) and (2-15).

$$c^D(V) = \frac{c^0}{\left(1 + \frac{m}{c^0} (P(V))^2 + \frac{e(V)^2 \varepsilon^b}{\chi(V) c^0 \varepsilon(V)}\right)} \quad (2-14)$$

$$\left(\because 1 - x = \frac{1}{1 + x} \text{ when } x \ll 1\right)$$

$$\varepsilon(V) = \chi(V) \quad (\because \chi(V) \gg \varepsilon^b) \quad (2-15)$$

In (2-14) and (2-15), approximations are based on the facts that $c^D(V)$ is a weak function of voltage and background relative permittivity ($\varepsilon_b/\varepsilon_0$) of approximately 7 is very small as compared to typical ferroelectric material relative permittivity of greater than 100 [2]-[4]. Inserting (2-14) and (2-15) into (2-7) results in (2-16).

$$k_t^2(V) = \frac{\varepsilon(V) 4q^2 P(V)^2}{c^0} \left(1 + \frac{m}{c^0} (P(V))^2 + \frac{e(V)^2 \varepsilon^b}{\chi(V) c^0 \varepsilon(V)}\right) \quad (2-16)$$

By using (2-11)-(2-13), (2-16) can be expressed as (2-17)

$$k_t^2(V) = \frac{4q^2}{3c^0\beta} \left\{ \begin{aligned} &\varepsilon(V) \left[\left(\frac{m + \varepsilon^b 4q^2}{3c^0\beta} \right) \frac{1}{(\varepsilon^0)^2} - \frac{1}{\varepsilon^0} \right] \\ &+ \left[1 - \frac{2m + 2\varepsilon^b 4q^2}{3c^0\beta\varepsilon^0} \right] + \frac{1}{\varepsilon(V)} \left[\frac{m + \varepsilon^b 4q^2}{3c^0\beta} \right] \end{aligned} \right\} \quad (2-17)$$

and can be further simplified into (2-18)

$$k_t^2(V) = A_{t1} \left\{ \frac{\varepsilon(V)}{\varepsilon^0} [-1 + A_{t2}] + [1 - 2A_{t2}] + \frac{\varepsilon^0}{\varepsilon(V)} A_{t2} \right\} \quad (2-18)$$

In (2-18), A_{t1} and A_{t2} are defined as follows:

$$A_{t1} = \frac{4q^2}{3c^0\beta} \quad (2-19)$$

$$A_{t2} = \frac{m + \varepsilon^b 4q^2}{3c^0\beta\varepsilon^0} \quad (2-20)$$

Permittivity tunability can be defined in (2-21),

$$\tau(V) = \frac{\varepsilon^0}{\varepsilon(V)} \quad (2-21)$$

and can be utilized to simplify (2-18) as follows:

$$k_t^2(V) = B_0\tau(V) + B_1 - (B_0 + B_1)\tau(V)^{-1} \quad (2-22)$$

$$B_0 = A_{r1}A_{r2} = \frac{4q^2(m + \varepsilon^b 4q^2)}{(3c^0\beta)^2 \varepsilon^0} \quad (2-23)$$

$$B_1 = A_{r1} - 2A_{r1}A_{r2} = \frac{4q^2}{3c^0\beta} - \frac{8q^2(m + \varepsilon^b 4q^2)}{(3c^0\beta)^2 \varepsilon^0} \quad (2-24)$$

It is noted that the electromechanical coupling coefficient can be expressed as a function of $\tau(V)$ and two material parameters B_0 and B_1 . For the extreme case ($V=0$) it can be easily shown that k_t^2 is zero as $\tau(V)$ is one at zero bias voltage in (2-21) as shown in (2-25).

$$k_t^2(V=0) = B_0 + B_1 - B_0 - B_1 = 0 \quad (2-25)$$

2.4.3. Nonlinear Modeling of Parallel Resonance Frequency $f_p(V)$

In a very similar way, parallel resonance frequency can be simplified to be utilized in circuit modeling. The model for the parallel resonance frequency in [16]-[18] is provided in (2-26).

$$f_p(V) = \frac{1}{2\pi \cdot 2t} \sqrt{\frac{c^D(V)}{\rho}} \quad (2-26)$$

In (2-26), ρ and t denote the density of BST material and thickness of BST layer. By using (2-9), (2-27), and (2-28),

$$f_0 = \frac{1}{2\pi \cdot 2t} \sqrt{\frac{c^0}{\rho}} \quad (2-27)$$

$$\sqrt{1-x} = 1 - \frac{1}{2}x \quad (\text{when } x \ll 1) \quad (2-28)$$

(2-26) can be further simplified as follows:

$$f_p(V) = f_0 \left[1 - \frac{1}{2} \left(\frac{m}{c^0} (P(V))^2 + \frac{e(V)^2 \varepsilon^b}{\chi^f(V) c^0 \varepsilon(V)} \right) \right] \quad (2-29)$$

Furthermore, by using (2-8), (2-11), and (2-15), (2-29) can be expressed as (2-30), and further simplified to (2-31).

$$f_p(V) = f_0 \left[1 - \frac{1}{2} \left(\frac{m + \varepsilon^b 4q^2}{3c^0 \beta} \right) \left(\frac{1}{\varepsilon(V)} - \frac{1}{\varepsilon^0} \right) \right] \quad (2-30)$$

$$f_p(V) = -\frac{1}{2} f_0 A_{r2} \tau(V) + f_0 \left(1 + \frac{1}{2} A_{r2} \right) \quad (2-31)$$

In (2-31), A_{r2} and $\tau(V)$ are defined in (2-20) and (2-21), respectively. Finally, by defining parameters A_0 and A_1

$$A_0 = -\frac{1}{2} f_0 A_{r2} = \frac{-1}{8\pi t} \sqrt{\frac{c^0}{\rho}} \left(\frac{m + \varepsilon^b 4q^2}{3c^0 \beta \varepsilon^0} \right) \quad (2-32)$$

$$A_1 = f_0 + \frac{1}{2} f_0 A_{r2} = \frac{1}{4\pi t} \sqrt{\frac{c^0}{\rho}} + \frac{1}{8\pi t} \sqrt{\frac{c^0}{\rho}} \left(\frac{m + \varepsilon^b 4q^2}{3c^0 \beta \varepsilon^0} \right), \quad (2-33)$$

the nonlinear model for f_p can be expressed as a function of $\tau(V)$ and two material parameters A_0 and A_1 .

$$f_p(V) = A_0 \tau(V) + A_1 \quad (2-34)$$

It can be easily shown that f_p converges to f_0 at zero bias voltage as $\tau(V)$ converges to one at zero bias voltage as shown in (2-35).

$$f_p(V=0) = A_0 \tau(V=0) + A_1 = -\frac{1}{2} f_0 A_{r2} + f_0 + \frac{1}{2} f_0 A_{r2} = \frac{1}{2\pi \cdot 2t} \sqrt{\frac{c^0}{\rho}} \quad (2-35)$$

2.4.4. Nonlinear Modeling of BST FBAR Impedance

Now that equations for the electromechanical coupling coefficient and parallel resonance frequency have been developed, it is straightforward to express series resonance frequency as a function of $f_p(V)$ and $k_t^2(V)$ based on the relationship between electromechanical coupling coefficient and resonance frequencies (see Appendix A).

$$f_s(V) = \frac{f_p(V)}{2} \left(1 + \sqrt{1 - \frac{16k_t^2(V)}{\pi^2}} \right) \quad (2-36)$$

Furthermore, motional inductance and capacitance can be described as (2-37) and (2-38) based on the relationship between device and circuit parameters (see Appendix A).

$$L_m(V) = \frac{1}{C_m(V)[2\pi f_s(V)]^2} \quad (2-37)$$

$$C_m(V) = C_e(V) \left[\left(\frac{f_p(V)}{f_s(V)} \right)^2 - 1 \right] \quad (2-38)$$

In order to take into account device losses such as mechanical loss represented by $R_m(V)$, dielectric/electric loss represented by $R_e(V)$ and ohmic loss due to electrodes and interconnects represented by R_s (Fig. 2.13), the measured real part of input admittance and impedance at the series and parallel resonance frequencies, respectively, are utilized for the modeling.

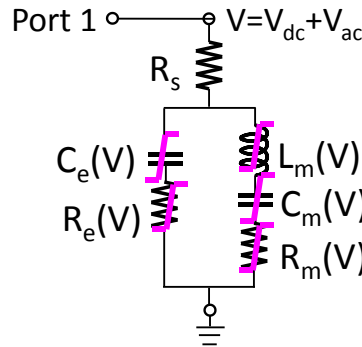


Figure 2.13: A schematic of nonlinear model for intrinsically switchable ferroelectric BST FBARs that incorporate mechanical loss, dielectric loss, and ohmic loss. Parameters C_e , L_m , C_m , R_m , and R_e are a function of applied voltage. Parameter R_s represents the device ohmic loss.

As these parameters are closely related to loss components, it can be easily shown that the real part of input admittance at the series resonance frequency is as follows.

$$\operatorname{Re}\{Y_{in}(V)\} = \frac{1}{\frac{2\pi f_s(V)L_m(V)}{Q_m(V)} + R_s} \quad (2-39)$$

Device ohmic loss term R_s can be determined through the de-embedding test structures discussed in [15], or measuring real part of impedance at high frequencies discussed in [47] and the mechanical quality factor $Q_m(V)$ can be expressed as a power series and coefficients can be found fitting them to the measurement results in (2-39) [36].

$$Q_m(V) = Q_{m,0} + Q_{m,1}V + Q_{m,2}V^2 + Q_{m,3}V^3 + \dots \quad (2-40)$$

Equations (2-36), (2-37), and (2-40) can be used to determine the motional resistance $R_m(V)$ in Fig. 2.13.

$$R_m(V) = \frac{2\pi f_s(V)L_m(V)}{Q_m(V)} \quad (2-41)$$

In a very similar way, it can be easily shown that the real part of input impedance at the parallel resonance frequency is expressed as (2-42).

$$\operatorname{Re}\{Z_{in}(V)\} = \frac{1}{\left[2\pi f_p(V)C_e(V)\right]^2 \left[R_m(V) + \frac{1}{2\pi f_p(V)C_e(V)Q_e(V)} \right]} \quad (2-42)$$

The dielectric quality factor $Q_e(V)$ can be expressed as a power series and coefficients can be found fitting them to the measurement results in (2-42) [36].

$$Q_e(V) = Q_{e,0} + Q_{e,1}V + Q_{e,2}V^2 + Q_{e,3}V^3 + \dots \quad (2-43)$$

Finally, equations (2-6), (2-35), and (2-43) lead to the nonlinear model for electrical resistance R_m in (2-44).

$$R_e(V) = \frac{1}{2\pi f_p(V)C_e(V)Q_e(V)} \quad (2-44)$$

2.5. Example Modeling Procedure based on the Measurement Results for the Intrinsically Switchable BST FBAR

This section shows a step-by-step modeling procedure for BST FBARs based on the measurement results provided in Chapter 2.3. Device parasitic inductance (L_s), ohmic loss (R_s), and low-frequency loss (R_a) are de-embedded for more accurate modeling procedure [36]. The de-embedded values of L_s , R_s , and R_a can be determined as 0.04 nH, 1.6 Ω , and 500 Ω , respectively, by performing least-squared fitting method at different bias voltages [36]. First, the capacitance nonlinear parameters C_{\max} , C_f , and V_2 in (2-6) are found

through the least squared fitting method using Matlab [63]. $C_e(V)$, C_{\max} , C_f , and V_2 in (2-6) are found to be 5.84 pF, 0.39 pF, and 6.45 V. Comparison between modeling and measurement results for the nonlinear capacitance is shown in Fig. 2.14.

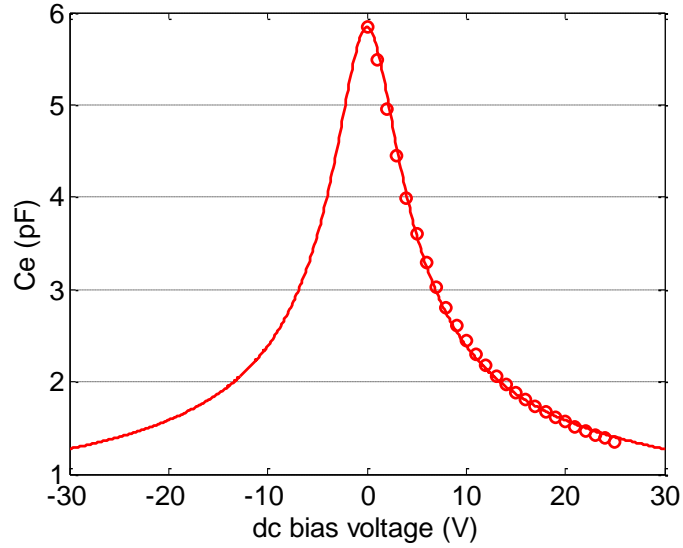


Figure 2.14: Modeling results of capacitance $C_e(V)$. C_{\max} , C_f , and V_2 in (2-6) are found to be 5.84 pF, 0.39 pF, and 6.45 V.

Capacitance tunability ($C_{\max}/C_e(V)$) is equal to permittivity tunability $\tau(V)$ in (2-21) and can be expressed as follows:

$$\tau(V) = \frac{\varepsilon^0}{\varepsilon(V)} = \frac{C_{\max}}{C_e(V)} = \left[\frac{5.45 \times 10^{-12}}{2 \cosh \left[\frac{2}{3} \sinh^{-1} \left(\frac{2V}{6.45} \right) \right] - 1} + 0.39 \times 10^{-12} \right]^{-1} \quad (2-45)$$

After determining $\tau(V)$, the electromechanical coupling coefficient nonlinear parameters B_0 and B_1 in (2-24) are then found through the least squared fitting method in Matlab. B_0 and B_1 are found to be -5.191×10^{-3} and 151.48×10^{-3} . Comparison between the modeling and measurement results for the electromechanical coupling coefficient is shown in Fig. 2.15.

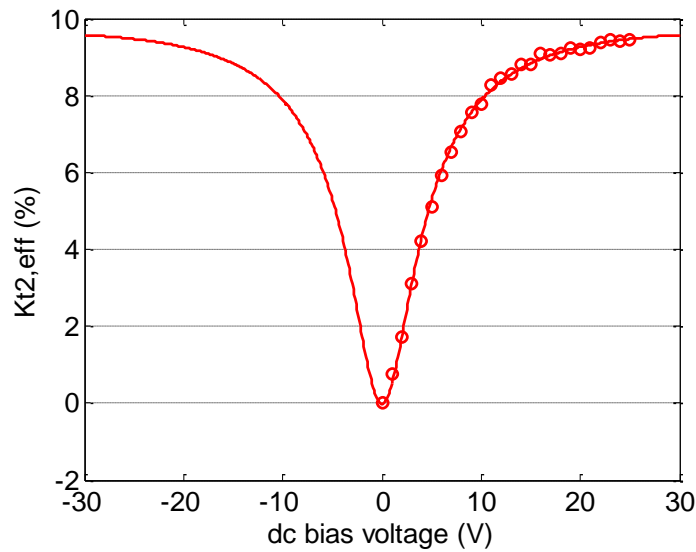


Figure 2.15: Modeling results of electromechanical coupling coefficient $k_t^2(V)$. B_0 is -5.191×10^{-3} and B_1 is 151.48×10^{-3} .

In a very similar way, the parallel resonance frequency nonlinear parameters A_0 and A_1 in (2-34) are found through the least squares fitting. A_0 and A_1 are found to be -8.9416×10^6 and A_1 is 2.0805×10^9 . It is noted that the parameter A_1 is the most sensitive parameter in the model which determines the resonance frequency. Comparison between modeling and measurement results for the FBAR parallel resonance frequency is shown in Fig. 2.16.

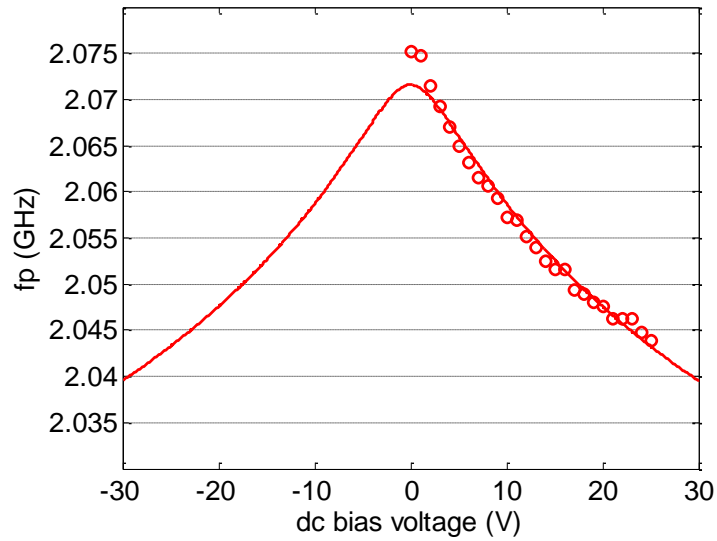


Figure 2.16: Modeling results for the parallel resonance frequency $f_p(V)$. A_0 is -8.9416×10^6 and A_1 is 2.0805×10^9 .

Subsequently, the series resonance frequency can be expressed as a function of $k_t^2(V)$ and $f_p(V)$ using (2-36) as shown in Fig. 2.17.

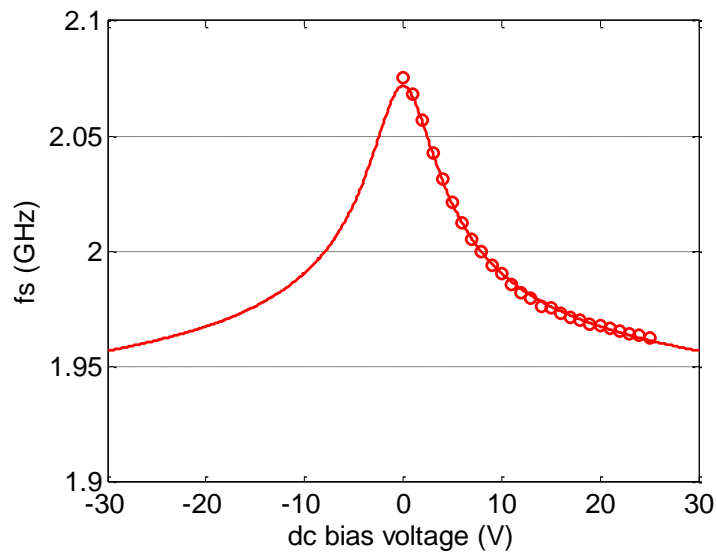


Figure 2.17: Modeling results for the series resonance frequency $f_s(V)$.

The motional inductance and capacitance can be easily expressed using (2-37)-(2-38). By using these nonlinear model parameters and measurement results, motional-quality-factor nonlinear parameter $Q_m(V)$ in (2-40) are then found using (2-39) through the least squared fitting method in Matlab. It turns out that $Q_m(V)$ can be expressed using a constant term $Q_{m0}=80.1$ over a wide range of dc bias voltage, as shown in the comparison between modeling and measurement results of real part of input admittance at the series resonance frequency (Fig. 2.18).

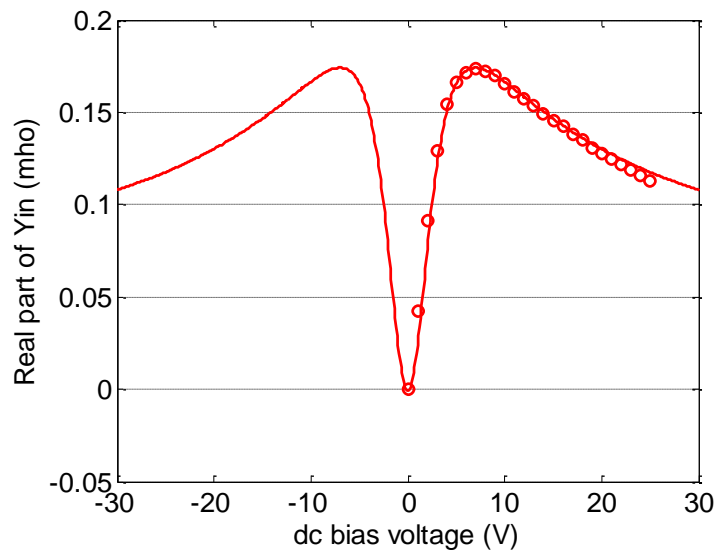


Figure 2.18: Modeling results of real part of input admittance at the series resonance frequency $\text{Real}\{Y_{in}(V)\}$. $Q_m(V)$ is 80.1.

In a very similar way, electrical quality factor nonlinear parameters $Q_e(V)$ in (2-43) are found using (2-42) through the least squares fitting. It also turns out that $Q_e(V)$ can be expressed using a constant term $Q_{e0}=14.4$ over a wide range of dc bias voltage, as shown

in the comparison between modeling and measurement results of real part of input impedance at the parallel resonance frequency (Fig. 2.19).

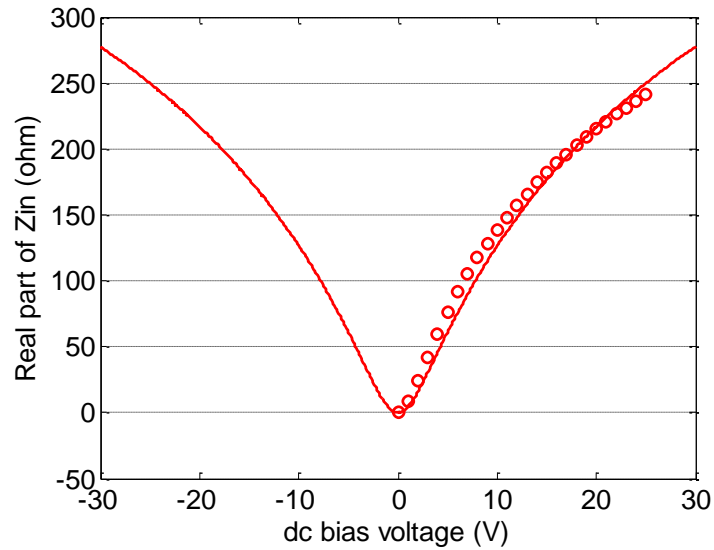


Figure 2.19: Modeling results of real part of input impedance at the parallel resonance frequency $\text{Re}\{Z_{in}(V)\}$. $Q_e(V)$ is 14.4.

Complete nonlinear circuit model parameters and the equations used are summarized in Table 2.2.

Table 2.2

Complete Equations and Nonlinear Model Parameter Values

Equations used	Parameter	Value
$C_e(V) = \frac{C_{\max} - C_f}{2 \cosh \left[\frac{2}{3} \sinh^{-1} \left(\frac{2V}{V_2} \right) \right] - 1} + C_f$	C_{\max} (pF)	5.84
	C_f (pF)	0.39
	V_2 (V)	6.45
$\tau(V) = \frac{\varepsilon_0}{\varepsilon(V)} = \frac{C_{\max}}{C_e(V)}$ $= \left[\frac{C_{\max} - C_f}{2 \cosh \left[\frac{2}{3} \sinh^{-1} \left(\frac{2V}{V_2} \right) \right] - 1} + C_f \right]^{-1}$	-	-
$f_p(V) = A_0 \tau(V) + A_1$	A_0	-8.9416×10^6
	A_1	2.0805×10^9
$k_t^2(V) = B_0 \tau(V) + B_1 - (B_0 + B_1) \tau(V)^{-1}$	B_0	-5.191×10^{-3}
	B_1	151.48×10^{-3}
$f_s(V) = \frac{f_p(V)}{2} \left(1 + \sqrt{1 - \frac{16k_t^2(V)}{\pi^2}} \right)$	-	-
$C_m(V) = C_e(V) \left[\left(\frac{f_p(V)}{f_s(V)} \right)^2 - 1 \right]$	-	-
$L_m(V) = \frac{1}{C_m(V) [2\pi f_s(V)]^2}$	-	-

$\text{Re}\{Y_m(V)\} = \frac{Q_m}{2\pi f_s(V)L_m(V)}$	Q_m	80.1
$R_m(V) = \frac{2\pi f_s(V)L_m(V)}{Q_m}$	-	-
$\text{Re}\{Z_{in}(V)\} = \frac{1}{[2\pi f_p(V)C_e(V)]^2}$ $\times \left[R_m(V) + \frac{1}{2\pi f_p(V)C_e(V)Q_e} \right]$	Q_e	14.4
$R_e(V) = \frac{1}{2\pi f_p(V)C_e(V)Q_e}$	-	-

The nonlinear model for intrinsically switchable BST FBAR is implemented in a circuit simulator such as ADS by using ADS symbolically-defined devices with the following basic relationships.

$$I_m = C_m(V) \frac{dV_{Cm}}{dt} \quad (2-46)$$

$$I_m = \frac{V_{Rm}}{R_m(V)} \quad (2-47)$$

$$V_{Lm} = L_m(V) \frac{dI_m}{dt} \quad (2-48)$$

$$I_e = C_e(V) \frac{dV_{Ce}}{dt} \quad (2-49)$$

$$I_e = \frac{V_{Re}}{R_e(V)} \quad (2-50)$$

The nonlinear circuit model is next simulated with the model parameters in Table 2.2.

2.6. Comparison between Measurement and Modeling Results

To achieve a better agreement between modeling and measurement results near the series resonance frequency, the BST capacitor nonlinearity in (2-6) is further modified (See Appendix B4).

$$C_e(V) = \frac{C_{\max} + C_{th}(V, I) - C_f}{2 \cosh \left[\frac{2}{3} \sinh^{-1} \left(\frac{2V}{V_2} \right) \right] - 1} + C_f \quad (2-51)$$

The measured reflection coefficients of the FBAR at various dc bias voltages with the P_{avs} of -18 dBm are plotted on the Smith chart (Fig. 2.20). The bias voltage is varied from 0 to 25 V in 5 V increments. It is observed that at zero bias measured and modeled results do not exhibit resonance, and the device behaves like a capacitor. Moreover, it is observed that as the dc bias increases, the electric-field-induced piezoelectricity also increases causing the impedance level to change. Also shown in the same figure are the simulated reflection coefficients based on the model developed in this Chapter. Figs. 2.21 and 2.22 compare the measured and modeled results of magnitude and phase of input impedance for the fabricated FBAR. As can be seen, the nonlinear modeling results agree very well with the measurement results over a wide range of dc bias voltages.

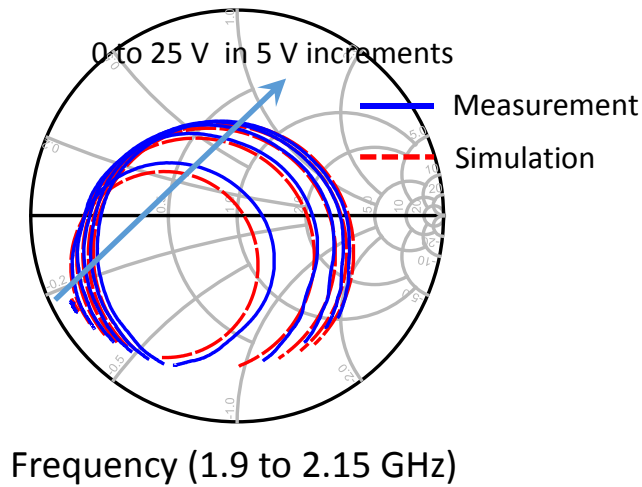


Figure 2.20: Comparison between the measurement and simulation results of reflection coefficient for intrinsically switchable ferroelectric BST FBARs on the Smith Chart. DC bias voltage is varied from 0 to 25 V in 5 V increments under -18 dBm RF power level.

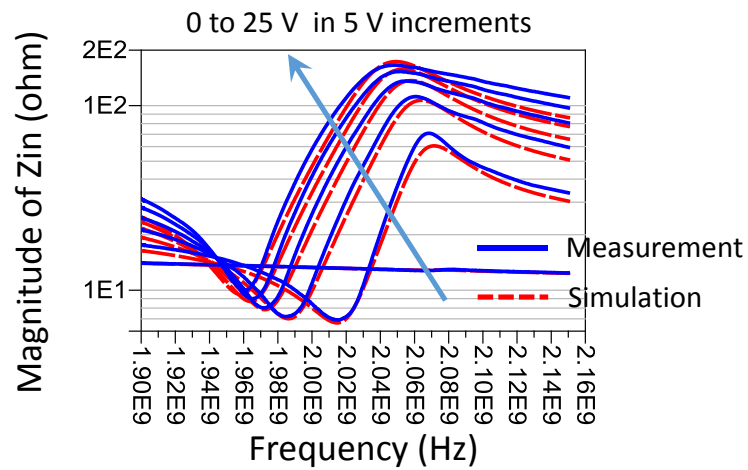


Figure 2.21: Comparison between the measurement and simulation results of magnitude of input impedance for intrinsically switchable ferroelectric BST FBARs. DC bias voltage is varied from 0 to 25 V in 5 V increments under -18 dBm RF power level.

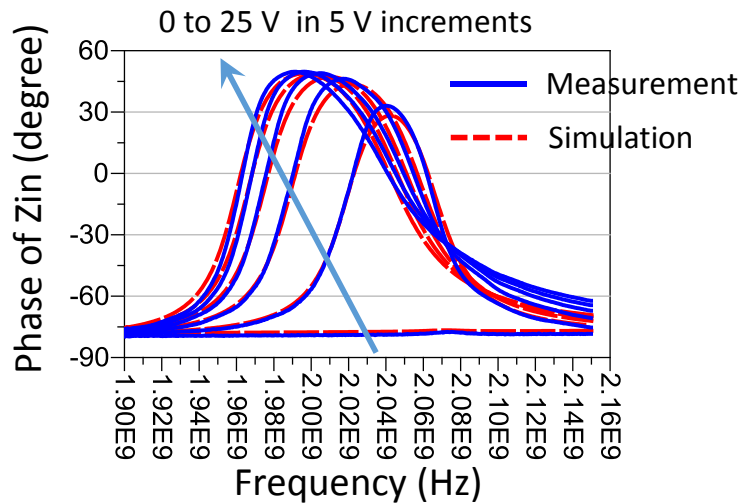
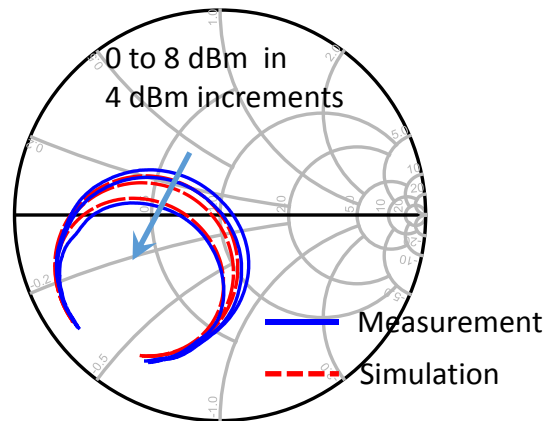


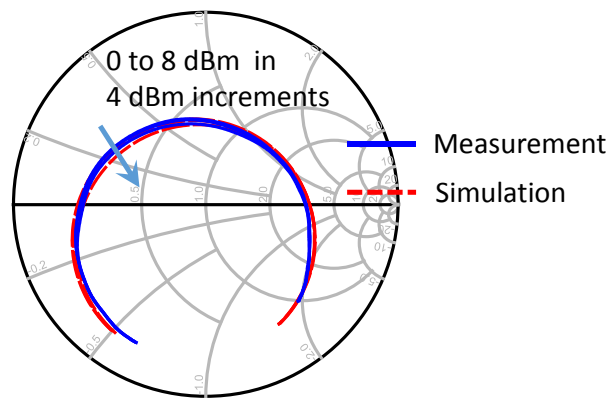
Figure 2.22: Comparison between the measurement and simulation results of phase of input impedance for intrinsically switchable ferroelectric BST FBARs. DC bias voltage is varied from 0 to 25 V in 5 V increments under -18 dBm RF power level.

A comparison between the measurement and large-signal simulation results for the BST FBAR at 5 V (lower bias voltage; the resonator is not fully on) and 25 V (higher bias voltage; the resonator is fully on) dc bias for different RF power levels is shown on the Smith chart (Fig. 2.23). The RF power level is varied from 0 dBm to 8 dBm in 4 dBm increments. A comparison of magnitude (Fig. 2.24) and phase of the device input impedance is also provided (Fig. 2.25). As can be seen in the figures, good agreement between the measurement and modeling results is achieved.



Frequency (1.9 to 2.15 GHz)

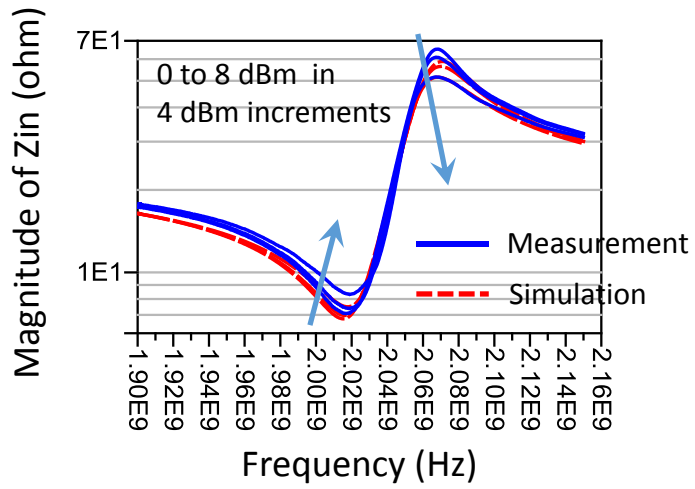
(a) 5 V



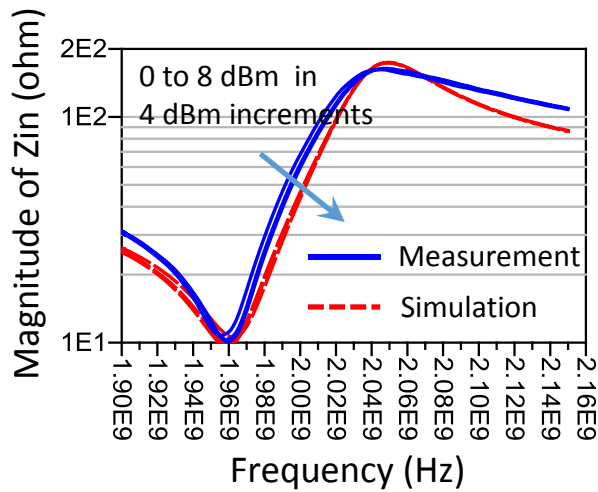
Frequency (1.9 to 2.15 GHz)

(b) 25 V

Figure 2.23: Comparison between the measurement and simulation results of reflection coefficient for intrinsically switchable ferroelectric BST FBARs on the Smith chart. RF power level is varied from 0 to 8 dBm in 4 dBm increments at (a) 5 V and (b) 25 V dc bias voltage.

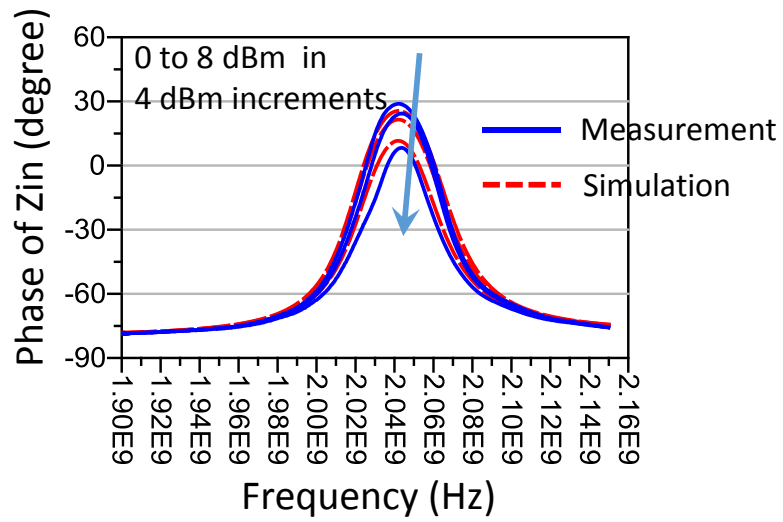


(a) 5 V

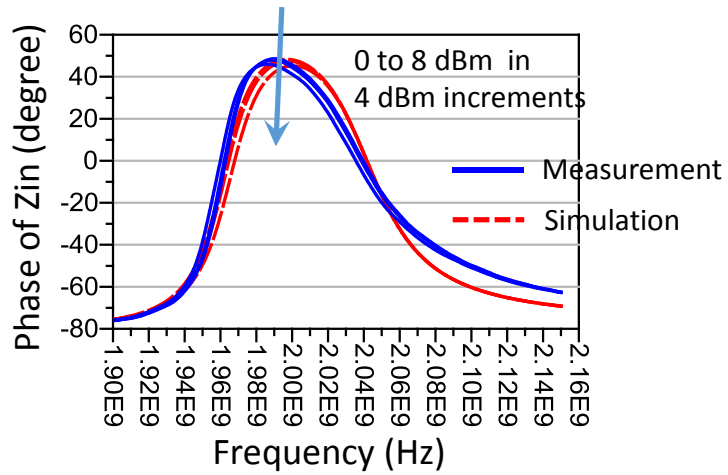


(b) 25 V

Figure 2.24: Comparison between the measurement and simulation results of magnitude of input impedance for intrinsically switchable ferroelectric BST FBARs. RF power level is varied from 0 to 8 dBm in 4 dBm increments at (a) 5 V and (b) 25 V dc bias voltage.



(a)



(b)

Figure 2.25: Comparison between the measurement and simulation results of phase of input impedance for intrinsically switchable ferroelectric BST FBARs. RF power level is varied from 0 to 8 dBm in 4 dBm increments at (a) 5 V and (b) 25 V dc bias voltage.

As discussed earlier in the measurement results, the FBAR at higher bias voltage exhibits more linear behavior as compared to lower bias voltages. Therefore, the developed model can be utilized to determine the operating bias voltage for switchable resonators that allows for higher electromechanical coupling coefficient and better linearity performance. The discrepancy between the modeling and measurement results can be attributed to the spurious resonance modes due to lateral-wave excitation, as well as device parasitic capacitance and resistance due to substrate [57], [58] that is not incorporated into the nonlinear model. It should be noted that the proposed model is applicable over a wide range of excitation voltages.

2.7. Chapter Conclusion

The nonlinear characterization and circuit modeling of intrinsically switchable ferroelectric BST FBARs are presented. Measurement results for the FBAR show the dc-bias-voltage-dependent behavior of the device capacitance, resonance frequencies, electromechanical coupling coefficient, and impedance. When the resonator is not fully “on” at lower bias voltages, the device shows highly RF-power-dependent characteristic such as reduced quality factor and electromechanical coupling coefficient as RF power increases. This can be due to the fact that the RF voltage swing over the device reduces effective device quality factor and coupling coefficient. When the resonator is fully “on” at higher bias voltages, the RF-power-dependent device behavior is significantly reduced, i.e. quality factors and electromechanical coupling coefficient are maintained as RF power level changes.

A step-by-step modeling procedure based on the physics of electrostrictive effect in BST thin film is provided to develop a simple yet effective nonlinear circuit model. Small-signal and large-signal nonlinear mBVD modeling results are presented and compared to the measurement results. The developed model is necessary for the material and device characterization of switchable BST FBARs, and thus the design of reconfigurable ferroelectric FBAR devices. Moreover, BST FBAR resonators and filters with enhanced linearity can be designed based on the developed model for further linearity improvement.

It is noted that the developed nonlinear model can be further improved for better accuracy by incorporating temperature-dependent characteristics for ferroelectric BST FBARs due to heating effects; the resonator breakdown voltage which will determine the device maximum power handling capacity; spurious resonance modes due to lateral waves; and device parasitic capacitance and resistance due to the substrate.

CHAPTER III

Design and Characterization of Intrinsically Switchable

Ferroelectric BST-on-Si Composite FBARs

3.1. Chapter Motivation

The characteristics of bulk acoustic wave resonators are strongly dependent on the mechanical properties and quality of the piezoelectric or ferroelectric thin films. Composite FBARs have been studied as a way of increasing the Q of zinc oxide (ZnO)- and aluminum nitride (AlN)-based piezoelectric acoustic resonators [60], [64]–[67]. Similarly, a low-mechanical-loss single crystal silicon layer can be added to underneath a ferroelectric BST layer sandwiched between the top and bottom electrodes in order to tailor resonator characteristics.

In this work, BST-on-Si composite FBARs are first designed to have significantly higher quality factors at the cost of the reduced effective electromechanical coupling coefficient (K_t^2) in composite FBARs. By designing a composite FBAR, device quality factor can be improved due to the low-mechanical-loss Si layer, which confines most of the acoustic displacement. K_t^2 is reduced due to the fact that the Si layer does not provide electromechanical transduction. The composite FBARs, which are designed to have higher

quality factors, can be utilized in the design of switchable low-phase-noise oscillators for multiband and frequency-agile communication systems, since the oscillator phase-noise is inversely proportional to the resonator Q^2 [68]. The K_t^2 is less important as compared to Q for the oscillator performance; however, a very small K_t^2 may prevent oscillations from starting up [69]. In order for a resonator to provide an inductive response between the series and parallel resonance frequencies, where a majority of the oscillators operate [69], [70], a K_t^2Q product of more than approximately 2.5 is required [47]. Therefore, a detailed study of the K_t^2 and Q as a function of BST-to-Si thickness ratio in BST-based composite FBARs is performed. It will be shown that through a careful selection of BST and Si thicknesses as well as the resonance mode, switchable ferroelectric composite FBARs with high Q s can be fabricated.

In addition to the BST-on-Si composite FBARs with high Q and small K_t^2 , composite FBARs for maximum K_t^2 and moderate Q are also designed. These resonators are useful for the design of ladder-type FBAR filters in which a high K_t^2Q is essential for low filter insertion loss and high K_t^2 is critical for wider filter bandwidth [62]. Because of the limitations of the 1-D acoustic transmission line model, various effects such as spurious resonances, edge effect, and acoustic energy leakage toward the lateral direction (then into the substrate) cannot be simulated using 1-D acoustic transmission line model [23], [24], [60]. To further improve the quality factors in such resonators, it is required to perform fundamental studies on loss mechanisms in BST acoustic resonators based on Multiphysics simulation. Important loss mechanisms in BST FBARs include lateral-wave spurious modes generation, scattering from defects and surface roughness, and acoustic attenuation in amorphous layer [48].

According to the published report, one of the dominant loss factors in thickness-extensional mode FBAR devices is the generation of spurious lateral waves [71]. It is very important to confine acoustic waves within the resonator in order to improve resonator quality factor [71]. This can be achieved by carefully designing the geometry of FBARs. More specifically, a well-designed raised or recessed frame can be made on the edges of device top electrode depending on resonator's dispersion characteristics. This technique was first proposed by J. Kaitila, et al. in [72] and has been widely used in state-of-the-art piezoelectric FBARs and SMRs [73]. In this work, such a frame design technique is first applied to intrinsically switchable ferroelectric BST-on-Si composite FBARs in which strong lateral-wave spurious modes are observed. By carefully designing a frame, only the main lateral mode can be excited effectively confining acoustic waves within the resonators. 2-D Multiphysics simulations are performed to design such a frame. Based on the simulation results, FBAR devices with and without a frame are fabricated, measured, and compared, validating the design method. This work is the first demonstration of BST based acoustic resonators with a frame structure helping to eliminate lateral-wave spurious modes.

3.2. BST-on-Si Composite FBARs with High Quality Factors

3.2.1 Design Procedure based on 1-D Acoustic Transmission Line Model

By carefully determining composite FBAR design parameters such as the BST to silicon thickness ratio (t_{BST}/t_{Si}); each layer's absolute thickness; and resonance mode number, the desired resonator characteristics such as Q and K_t^2 can be achieved [23], [24]. As can be seen in Fig. 3.1, the device vertical dimensions (thickness of each layer), as well

as the horizontal dimensions (FBAR area) need to be determined given the material parameters. The parameters include the acoustic impedance, acoustic velocity, mechanical quality factor of each layer and the electromechanical coupling coefficient (K_t^2) of the BST material in its fully on state.

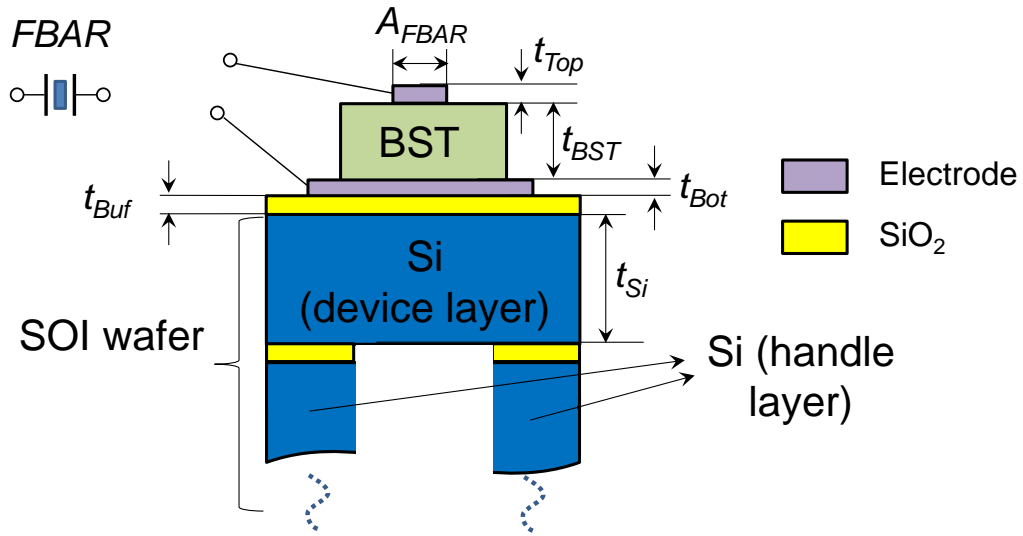


Figure 3.1: A cross section of a BST-on-Si composite FBAR. This is not to scale.

The 1-D acoustic transmission line model [60] that predicts electrical input impedance as a function of layer thicknesses, as well as material parameters is utilized to qualitatively determine the characteristics of the resonator. The acoustic transmission line model simulation procedure is as follows. First, the air in Fig. 3.1 is represented by its acoustic characteristic impedance $Z_{0,air}$ and it is transformed to acoustic impedances of Z_{top} and Z_{bot} , through the successive impedance transformations [23].

$$Z = Z_0 \frac{Z_L + Z_0 \tanh(\gamma t)}{Z_0 + Z_L \tanh(\gamma t)} \quad (3-1)$$

In (3-1), γ , t , Z_0 and Z_L , are each layer's acoustic propagation constant, thickness, acoustic characteristic impedance, and acoustic impedance seen looking into previous layer, respectively. The propagation constant (γ) is calculated using as follows [74]:

$$\gamma = \alpha + j\beta \quad (3-2)$$

$$\alpha = \frac{\beta}{2Q_m}, \quad \beta = \frac{\omega}{v} \quad (3-3)$$

In (3-2) and (3-3), α , β , Q_m , ω , and v denote each layer's attenuation constant, phase constant, mechanical quality factor, angular frequency, and acoustic velocity, respectively. Once Z_{top} and Z_{bot} are determined and normalized by BST layer's acoustic impedance ($Z_{0,BST}$)

$$z_{top} = \frac{Z_{top}}{Z_{0,BST}}, \quad z_{bot} = \frac{Z_{bot}}{Z_{0,BST}}, \quad (3-4)$$

the electrical input impedance of the composite FBAR in Fig. 3.1 can be calculated as follows [60]:

$$Z_{in} = \frac{1}{j\omega C_e} \cdot \left[1 - K^2 \frac{\tan(\frac{\phi}{2})}{\frac{\phi}{2}} \cdot \frac{(z_t + z_b) \cos^2(\frac{\phi}{2}) + j \sin(\phi)}{(z_t + z_b) \cos(\phi) + j(z_t z_b + 1) \sin(\phi)} \right] \quad (3-5)$$

In (3-5), K^2 , ϕ , and C_e are the intrinsic electromechanical coupling coefficient of the BST, the acoustic phase across the BST layer, and the capacitance, respectively. Most of the acoustic material parameters for each layer used in the acoustic transmission line model simulation in Chapter 3.2 are obtained from [23] and provided in Table 3.1.

Table 3.1

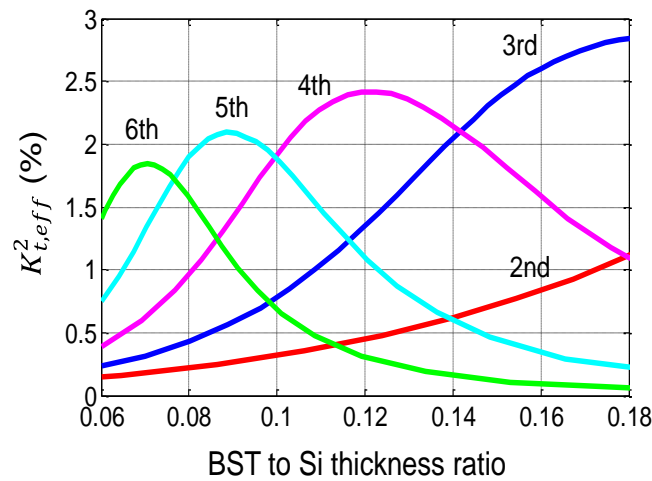
Acoustic Parameters used in 1-D Acoustic Transmission Line Model

Simulations in Chapter 3.2

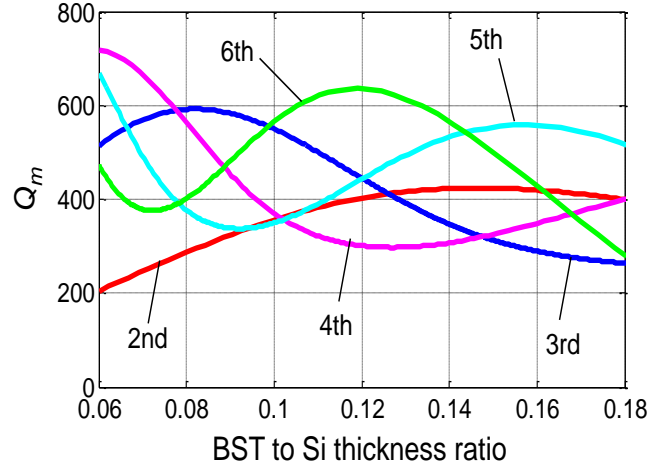
Layer	Acoustic velocity ν (m/s)	Acoustic impedance Z_0 (kg/m ² ·s)	Mechanical quality factor Q_m	Electromechanical coupling coefficient K^2 (%)
Air	360	400	-	-
Pt	3300	69.8×10^6	130	-
BST	5600	33.0×10^6	300	4
Pt	3300	69.8×10^6	130	-
SiO ₂	5100	12.5×10^6	130	-
Si	8100	19.5×10^6	2500	-
Air	360	400	-	-

As an example, composite FBARs are designed to have the resonance frequency of 2.5 GHz. In the simulation, the thicknesses of Pt top electrode (t_{Top}), Pt bottom electrode (t_{Bot}), and SiO₂ buffer layer (t_{Buf}) are set to 100 nm, 100 nm, and 200 nm, respectively, similar to [23]. The electromechanical coupling coefficient (K_t^2) of the BST material is set to 4%. This value is approximated from the preliminary measurement results for BST FBARs, which were fabricated under the similar conditions in this work. Other parameters are the same as used in [23].

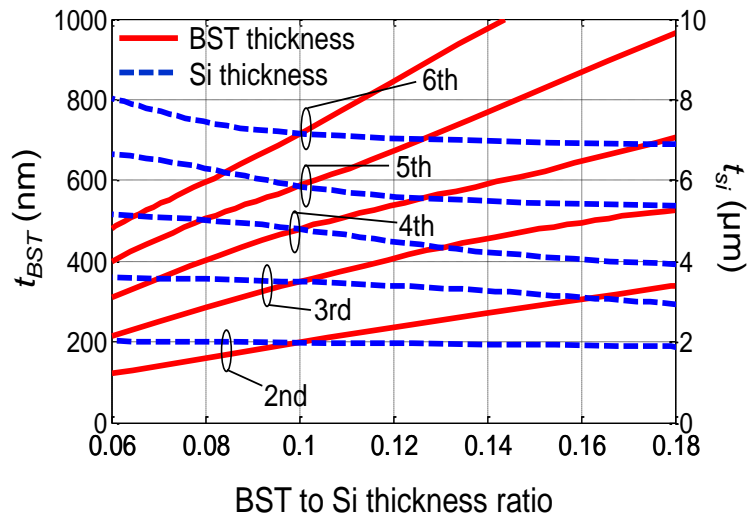
Figure 3.2 shows the $K_{t,eff}^2$, mechanical quality factor (Q_m), and thicknesses of BST (t_{BST}) and Si (t_{Si}) for 2.5-GHz FBARs as a function of BST to Si thickness ratio and mode number. Figures. 3.2(a) and 3.2(b) reveal that the different combination of mode number and BST to Si thickness ratio is required for obtaining the specific values of $K_{t,eff}^2$ and Q_m . Also, as the mode number increases, the required absolute thicknesses of BST and Si increase for the same thickness ratio as seen in Fig. 3.2(c).



(a)



(b)



(c)

Figure 3.2: Simulated (a) $K_{t,eff}^2$, (b) quality factor, (c) BST thickness and Si thickness as a function of BST to Si thickness ratio and different thickness-extensional resonance mode number. The simulation is based on the 1-D acoustic transmission line model.

Based on the desired $K_{t,eff}^2$ and Q_m , the mode number along with BST to Si thickness ratio can be chosen so that they are in a practical range. As a proof of concept,

the 4th thickness-extensional resonance mode and 0.08 BST to Si thickness ratio is chosen in order to utilize an off-the-shelf 5- μm SOI wafer. The required BST thickness is calculated to be 400 nm. The expected $K_{t,eff}^2$ and Q_m are approximately 0.9% and 600, respectively. Once the BST thickness (t_{BST}) is determined, BST area can be determined as follows.

$$A_{FBAR} = \frac{C_e t_{BST}}{\epsilon_0 \epsilon_r} \quad (3-6)$$

In (3-6), ϵ_0 is the permittivity of free-space and ϵ_r is the relative permittivity of BST when resonators are biased when the device is in fully on. By determining the thicknesses of each layer in a composite FBAR and the device area, a composite FBAR's electrical response can be predicted. For an experimental verification, the high- Q composite FBAR designed here is fabricated.

3.2.2. Fabrication Procedure using RF Magnetron Sputtering

A switchable BST-on-Si composite FBAR is fabricated on a pre-platinized silicon-on-insulator (SOI) wafer with 100-nm platinum (Pt), 200-nm SiO₂-buffer, 5- μm Si-device, 200-nm buried-oxide, and 500- μm Si-handle layer thicknesses. First, the Pt layer is selectively patterned to serve as the bottom electrode using reactive ion etching (RIE). Subsequently, a 400-nm-thick BST (Ba_{0.5}Sr_{0.5}TiO₃) layer is deposited using RF magnetron sputtering where the growth temperature is set to 650 °C with 3:1 Ar/O₂ total pressure of 45 mTorr. Another 100-nm-thick Pt layer is then deposited and patterned using e-beam

evaporation and liftoff. After annealing is performed at 500 °C for 30 minutes, the BST layer is etched in diluted HF (10:1) solution.

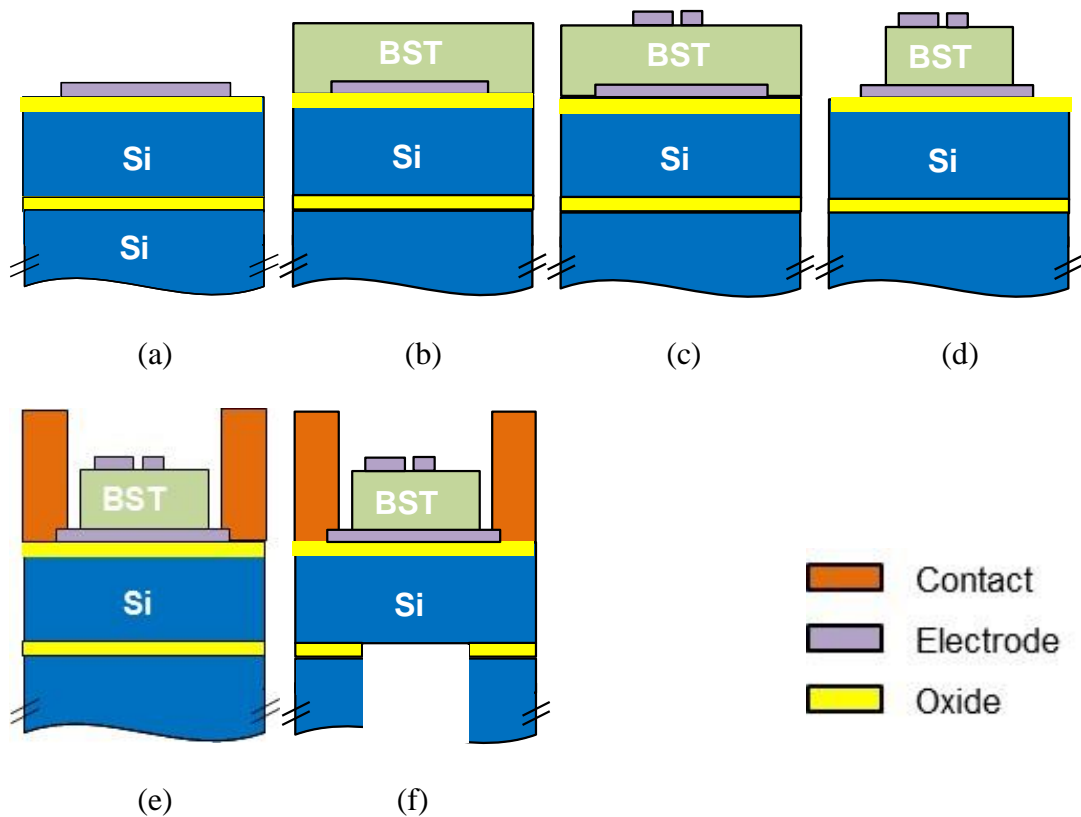


Figure 3.3: Fabrication process for a BST-on-Si composite FBAR: (a) bottom electrode, (b) BST deposition, (c) top electrode, (d) BST etching, (e) contact, and (f) Si DRIE.

Subsequently, a thick metal layer (50/600/50/100-nm-thick Ti/Al/Ti/Au) is deposited as a contact layer. Finally, the BST-on-Si composite FBAR device is released by etching the 500- μm -thick Si-handle layer using deep reactive ion etching (DRIE) and then etching the

200-nm-thick buried-oxide layer in BHF solution. A step-by-step fabrication procedure for a BST-on-Si composite FBAR is shown in Fig. 3.3. A photograph of a fabricated 1-port BST FBAR that has an area of $1600 \mu\text{m}^2$ is shown in Fig. 3.4.

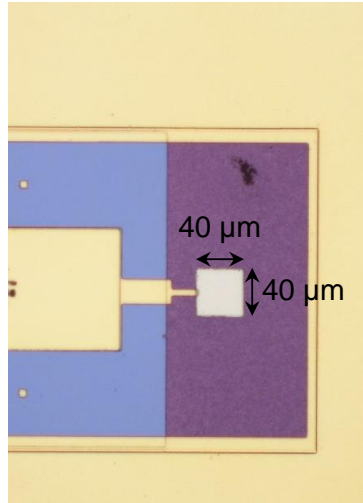
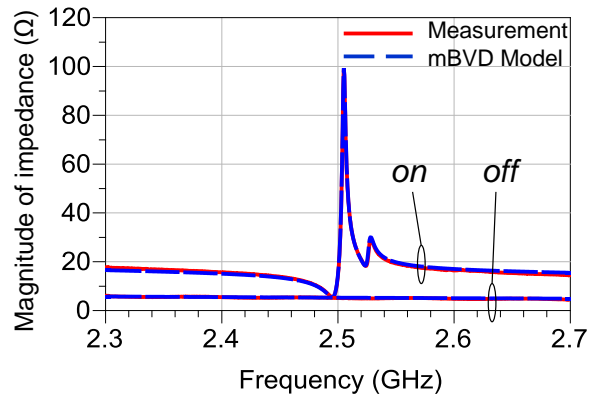


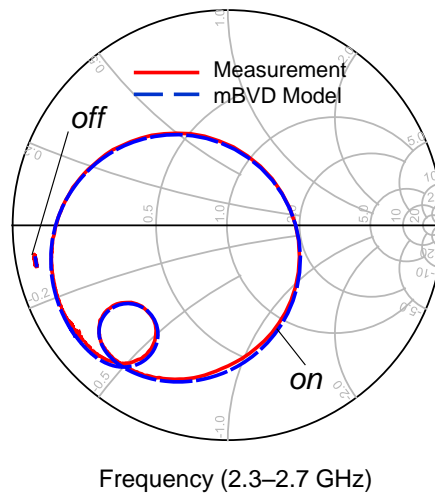
Figure 3.4: A photograph of a fabricated 1-port BST FBAR ($A_{FBAR}=1600 \mu\text{m}^2$). The vertical dimensions for fabricated devices are as follows: $t_{Top}=100 \text{ nm}$, $t_{BST}=400 \text{ nm}$, $t_{Bot}=100 \text{ nm}$, $t_{Buf}=200 \text{ nm}$, $t_{Si}=5 \mu\text{m}$.

3.2.3 Measurement Results and Discussion

The S parameters of the fabricated devices are measured using 250- μm pitch ground-signal-ground (GSG) probes and an Agilent E8364C network analyzer. The open-short-load calibration is performed from 0.1 to 5 GHz in the 50- Ω system impedance. A dc-bias voltage is applied through a bias tee. Measurement results for a designed 1-port BST-on-Si composite FBAR ($A_{FBAR}=1600 \mu\text{m}^2$) are provided in Fig. 3.5.



(a)



(b)

Figure 3.5: Measurement and modeling results for a 1-port switchable BST FBAR when the resonator is in *on* ($V_{dc}=40$ V) and *off* (0 V) states. (a) Magnitude of input impedance and (b) reflection coefficients on the Smith chart.

The series resonance frequency f_s , at which the input conductance is maximized, is measured to be 2.496 GHz and the parallel resonance frequency f_p , at which the input

resistance is maximized, is measured to be 2.505 GHz. The measured Q_s , Q_p , and $K_{t,eff}^2$ are 409, 847, and 0.86%, respectively using (2-1) and (2-2). The measured $K_{t,eff}^2$ and f_s match well with the predicted values of 0.9% and 2.5 GHz. Figure 3.5 shows the undesired spurious resonance mode after the parallel resonance frequency, approximately at 2.53 GHz. This spurious resonance can be eliminated by designing a frame [72], [73] that will be introduced later in this Chapter or smoothed out over the frequency by adopting the apodization technique [75].

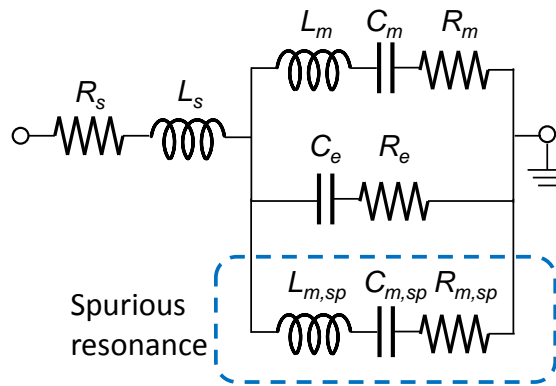


Figure 3.6: A schematic of mBVD model that includes an additional branch for spurious resonance and the parasitic inductance L_s for better fitting to measurements. The model is for when the BST FBAR is in its *on* state.

In addition to the measurement results, modeling results are necessary for better understanding and characterization of FBARs. In order to examine the resonator figures of merit when the device is in fully on state, linear mBVD model in Fig. 3.6 is utilized. As seen in Fig. 3.6, an additional branch is added to the typical mBVD model to consider the spurious resonance mode observed in the measurements results. The series inductor L_s is

also added to the model for better fitting to measurement results. Complete model parameter values of mBVD model in Fig. 3.6 are provided in Table 3.2.

Table 3.2
Parameter Values of mBVD Model in Fig. 3.6

Parameter	Value	Parameter	Value
R_s	3.5 Ω	C_e	3.9 pF
L_s	0.05 nH	R_e	0.19 Ω
L_m	142.36 nH	$L_{m,sp}$	1281.2 nH
C_m	28.555 fF	$C_{m,sp}$	3.1 fF
R_m	2.3 Ω	$R_{m,sp}$	39 Ω

As can be seen in Fig. 3.5, the modeling results are in excellent agreement with the measurement results. The Q_m , which is useful for characterizing the ferroelectric material quality, is calculated by (3-7) using the parameters in Table 3.2.

$$Q_m = \frac{2\pi f_s L_m}{R_m} = \frac{1}{R_m} \sqrt{\frac{L_m}{C_m}} \quad (3-7)$$

The Q_m of 971, as well as the $Q_m \times f_s$ of 2423 GHz is highest to date among switchable acoustic resonators based on ferroelectric BST thin films. When the BST FBAR is in the off state, the $C_{e,off}$ of 11.7 pF, R_s of 2.5 Ω , and L_s of 0.05 nH are used in the modeling (see the off response in Fig. 3.6).

3.2.4 Temperature Dependent Characteristics of Intrinsically Switchable Ferroelectric Composite FBARs

In addition to voltage-dependent characteristics of intrinsically switchable ferroelectric FBARs, it is necessary to characterize FBARs' temperature dependent characteristics. Therefore, the temperature dependent characterization of intrinsically switchable ferroelectric BST-on-Si composite FBARs is performed. In frequency reference applications such as oscillators, it is essential to have temperature-stable BAW resonators (i.e. resonance frequencies, quality factors, and electromechanical coupling coefficients should be temperature stable). Temperature-dependent characteristics of $\text{Ba}_{0.25}\text{Sr}_{0.75}\text{TiO}_3$ SMRs and $\text{Ba}_{0.5}\text{Sr}_{0.5}\text{TiO}_3$ SMRs have been reported in [46] and [52], respectively. In this Chapter, temperature dependence of composite FBARs using $\text{Ba}_{0.5}\text{Sr}_{0.5}\text{TiO}_3$ thin films grown with RF magnetron sputtering is investigated for the first time. Measured temperature dependence of resonance frequencies, quality factors, and effective electromechanical coupling coefficients as a function of various bias voltages is reported.

Figures 3.7(a) and 3.7(b) show a photograph of a fabricated composite FBAR with the area of $1325 \mu\text{m}^2$, and a schematic cross section of the fabricated composite FBAR, respectively. The fabrication conditions are the same as the ones in Chapter 3.2.2. Measurements are performed with an Agilent E8364C network analyzer. A 150- μm pitch ground-signal-ground (GSG) probe is used. Devices are measured on a temperature controller stage from 30 °C to 100 °C in 5 °C increments. The dc bias voltage is varied from 0 V to 40 V in 5 V increments. Measurement results of magnitude of input impedance for the fabricated BST-on-Si composite FBAR (Fig. 3.7(a)) are plotted in Fig. 3.8 as a function of temperature at various dc bias voltages.

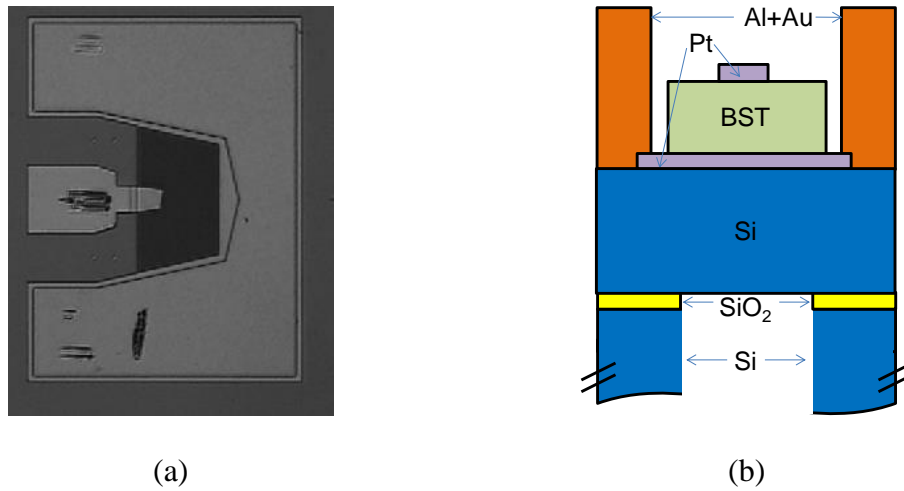


Figure 3.7: (a) A photograph of a fabricated composite FBAR with the area of 1325 μm^2 and (b) a schematic cross section of a composite FBAR.

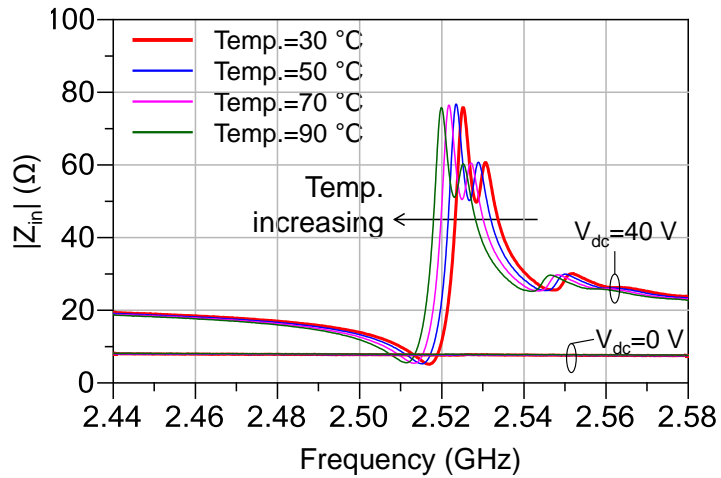


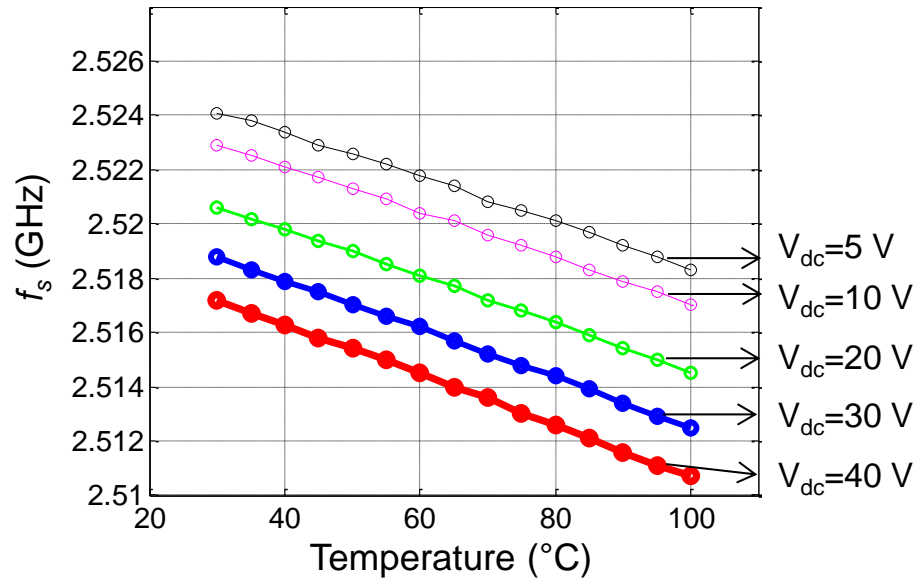
Figure 3.8: Measured magnitude of input impedance (Z_{in}) results for the BST-on-Si composite FBAR with various temperatures (Temp.=30°C, 50°C, 70°C, 90°C) when the resonator is switched on ($V_{dc}=40$ V) and off ($V_{dc}=0$ V).

The results for the 4th resonance mode, which has the highest quality factors compared to other resonance modes, are plotted in Fig. 3.8. Without a dc bias voltage

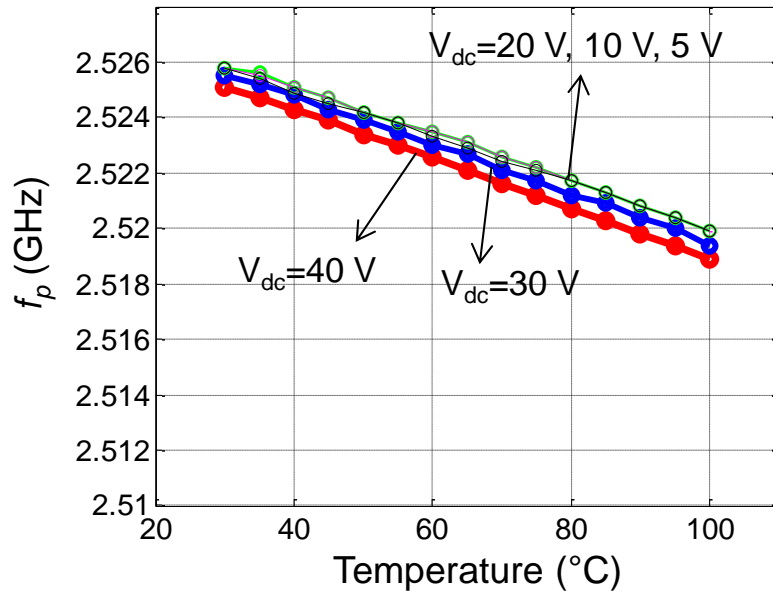
($V_{dc}=0$ V), the resonator is in its *off* state, exhibiting no resonance. By applying a dc bias voltage (e.g., $V_{dc}=40$ V), the resonator is in its on-state, in which the strength of resonance increases with the bias voltage. The measurement results show that series and parallel resonance frequencies decrease as a function of temperature while the resonance strength or impedance level remains almost constant with temperature.

Figure 3.9 shows the change in series (f_s) and parallel (f_p) resonance frequencies with respect to the temperature (30°C to 100 °C) at the different bias voltage (5 V to 40 V). Both f_s and f_p decrease with the temperature increasing. The temperature coefficient of frequency (TCF) at series resonance is calculated to be -37 ppm/°C at 40 V, -36 ppm/°C at 30 V, -35 ppm/°C at 20 V, -33 ppm/°C at 10 V, and -33 ppm/°C at 5 V. The TCF at parallel resonance is calculated to be -35 ppm/°C at 40 V, -35 ppm/°C at 30 V, -33 ppm/°C at 20 V, -33 ppm/°C at 10 V, and -33 ppm/°C at 5 V.

These results show that regardless of the bias voltage levels and the type of resonance, the TCF of fabricated composite FBARs is approximately -35 ppm/°C. The reported value of -35 ppm/°C for a BST FBAR is smaller than the value of -75 ppm/°C for a BST SMR in [46]. The TCF value for a BST SMR in [46] is estimated from the measurement results in the range of 300 K to 370K which is a similar temperature range in this work. Smaller TCF of the composite FBAR in this work can be attributed that the most of acoustic signal is confined in the layer of Si which has the TCF of approximately -31 ppm/°C [76]. As the Si layer (5 μ m) is much thicker than the BST layer (400 nm) in this work, it is believed that the TCF of the composite BST-on-Si FBAR approaches the TCF of Si.



(a)

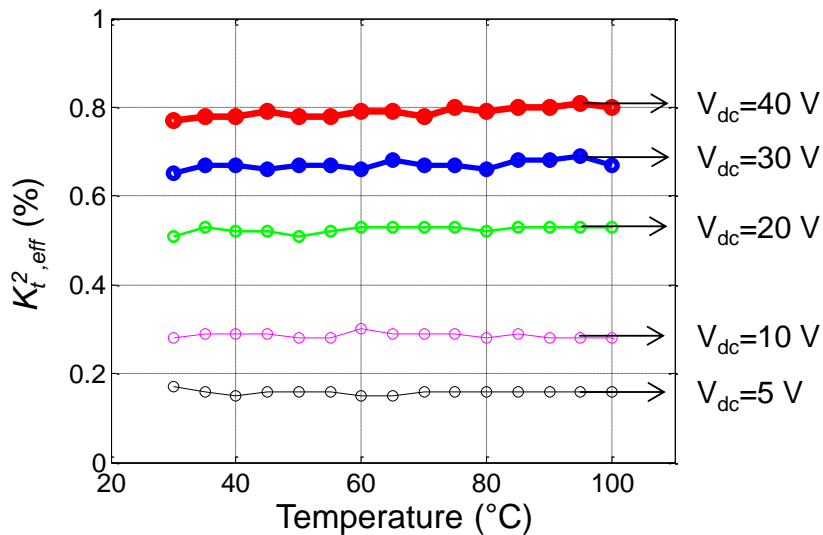


(b)

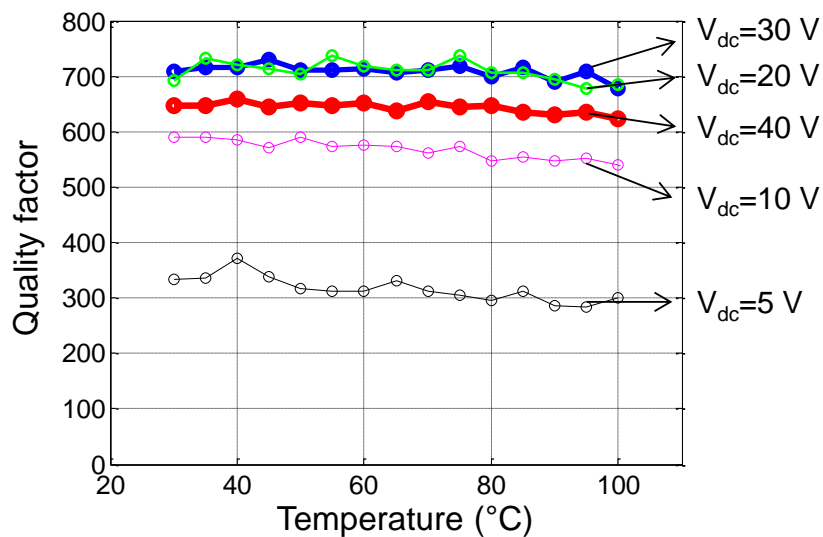
Figure 3.9: The change in (a) series and (b) parallel resonance frequencies with respect to temperature. The results are shown at a bias of 5, 10, 20, 30, and 40 V.

In the range of temperature measurement (30 °C to 100 °C), the change in resonance frequency is less than 0.26%. The TCF and therefore the change in resonance frequency can be reduced by utilizing the temperature stabilization technique such as including a layer of SiO₂ which has the positive temperature coefficient of elasticity (TCE) [76]. The two main figures of merit for BAW resonators are the effective electromechanical coupling coefficient ($K_{t,eff}^2$) and the quality factor (Q) which are calculated using (2-1) and (2-2).

Figure 3.10 shows the change in $K_{t,eff}^2$ and Q with respect to the temperature (30°C to 100 °C) at the different bias voltage (5 V to 40 V). As can be seen in Fig. 3.10, both $K_{t,eff}^2$ and Q remain almost constant over the temperature. The variation of $K_{t,eff}^2$ over the measured temperature range is calculated to be 5.2% at 40 V, 6.2% at 30 V, 3.9% at 20 V, 7.1% at 10 V, and 11.8% at 5 V. The variation of Q over the measured temperature range is calculated to be 3.6% at 40 V, 4.5% at 30 V, 6.5% at 20 V, 8.3% at 10 V, and 15.0% at 5 V. The percentage variation of $K_{t,eff}^2$ and Q is in general much smaller than the one in BST SMRs [52].



(a)



(b)

Figure 3.10: The change in (a) $K_{t,eff}^2$ and (b) Q with respect to temperature. The results are shown at a bias voltage of 5, 10, 20, 30, and 40 V.

3.3. BST-on-Si Composite FBARs for Maximum K_t^2

3.3.1. Design Procedure based on 1-D Acoustic Transmission Line Model

It is important to maximize K_t^2 in the design of ladder-type BAW filters so as to achieve low insertion loss, as well as wide bandwidth [62], [71], [75]. Therefore, the composite FBAR is designed to maximize its K_t^2 . Similar to the design method based on 1-D acoustic transmission line model described in Chapter 3.2, the K_t^2 and absolute thickness of each layer can be plotted as a function of the BST to Si thickness ratio (t_{BST}/t_{Si}) with the different resonance mode number for the desired resonance frequency f_s .

Table 3.3

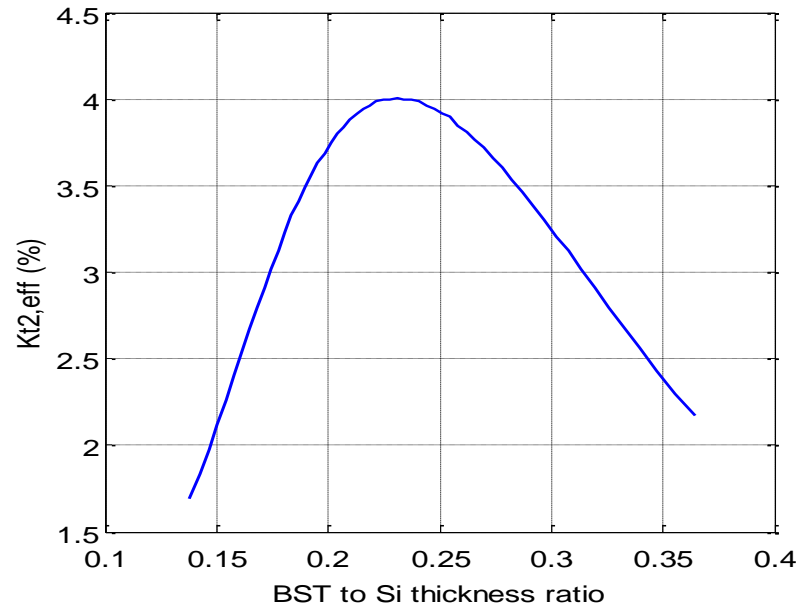
Acoustic Parameters used in 1-D Acoustic Transmission Line Model

Simulations in Chapter 3.3

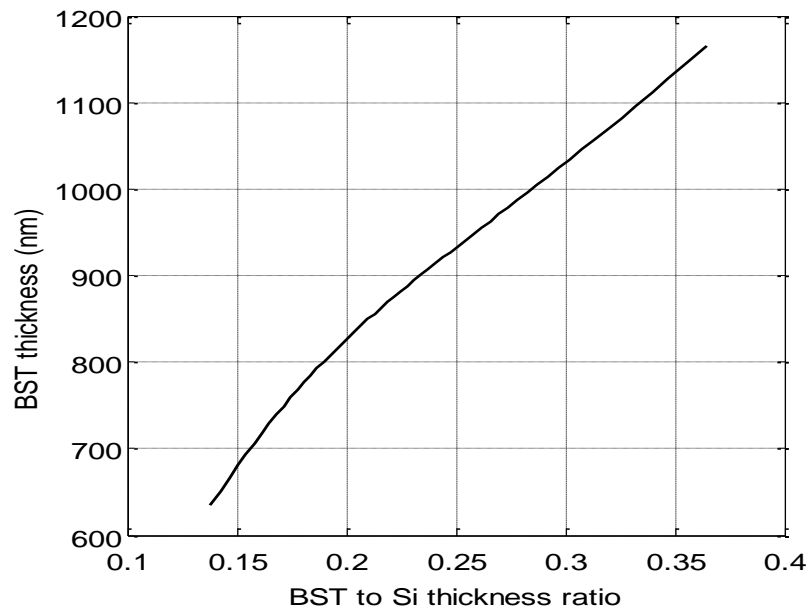
Layer	Acoustic velocity ν (m/s)	Acoustic impedance Z_0 (kg/m ² ·s)	Electromechanical coupling coefficient K^2 (%)
Air	360	400	-
Pt	3236	69.4×10^6	-
BST	6307	35.3×10^6	6
Pt	3236	69.4×10^6	-
SiO ₂	5848	12.9×10^6	-
Si	8446	19.7×10^6	-
Air	360	400	-

Based on the previous measurement results in Chapter 3.2, acoustic parameters in Table 3.2 have been modified to ones in Table 3.3 for better fitting to measurement results. Since mechanical quality factors have not been characterized well for resonators grown by RF magnetron sputtering and prediction do not match well with measurement results due to other effects such as lateral waves and edge effects, quality factors are not considered in 1-D simulation.

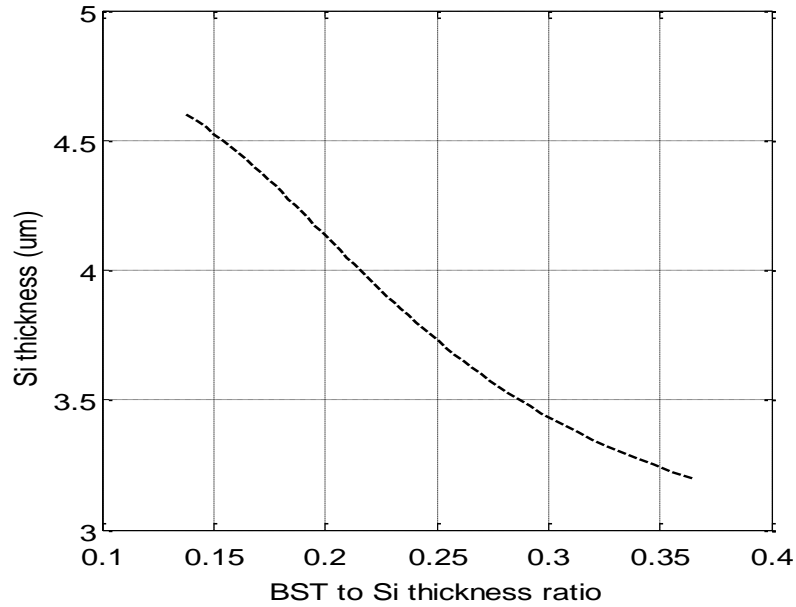
The ratio t_{BST}/t_{Si} along with the mode number can be chosen to maximize $K_{t,eff}^2$ at the given frequency while maintaining a thickness of each layer within a practical range. As a proof of concept, 2-GHz resonator is designed and the third resonance mode has been selected to utilize the off-the-shelf 4 μm SOI wafer. $K_{t,eff}^2$, BST thickness, and Si thickness are plotted as a function of BST to Si thickness ratio in Fig. 3.11. As can be seen, BST to Si thickness ratio of 0.2157 can maximize the value of $K_{t,eff}^2$. The required BST thickness is calculated to be 863 nm. The Matlab code used for this acoustic transmission line simulation is attached in Appendix C which can be modified to simulate BST-on-Si composite FBARs with a specific resonance frequency and resonance mode as similar to Fig. 3.11. Based on the 1-D analytic simulation, 2-D Multiphysics simulation is performed next to predict spurious resonance modes due to unwanted lateral waves and to eliminate them.



(a)



(b)



(c)

Figure 3.11: Simulated (a) $K^2_{t,eff}$, (b) BST thickness, and (c) Si thickness as a function of BST to Si thickness ratio at the third resonance mode for a 2-GHz resonator. Simulation is based on the 1-D acoustic transmission line model.

3.3.2. Design Procedure based on 2-D Multiphysics Simulation for Lateral-Wave Spurious-Modes Elimination

Measurement results for the BST-on-Si composite FBARs at different thickness-extensional resonance modes in Chapter 3.2 are shown in Fig. 3.12. As can be seen, depending on the thickness-extensional resonance mode in composite FBARs, the effect of lateral modes on the overall resonator performance is different; however, it is clear that

each mode suffers from lateral-wave spurious modes, lowering device qualities, regardless of the mode number. Therefore, it is highly desirable to eliminate such spurious modes.

It is noted that the spurious modes are observed after the series resonance frequencies shown in Fig. 3.12. This indicates that a BST-on-Si composite structure used in this work belongs to a class of resonators with dispersion type I characteristic [72], [73], in which wave number β increases with frequency f as shown in Fig. 3.13(a). Therefore, a raised frame shown in Fig. 3.13(b) should be utilized so as to eliminate such spurious modes [72], [73]. Only the main lateral mode is excited due to the new boundary condition between the active and outside regions [72], [73].

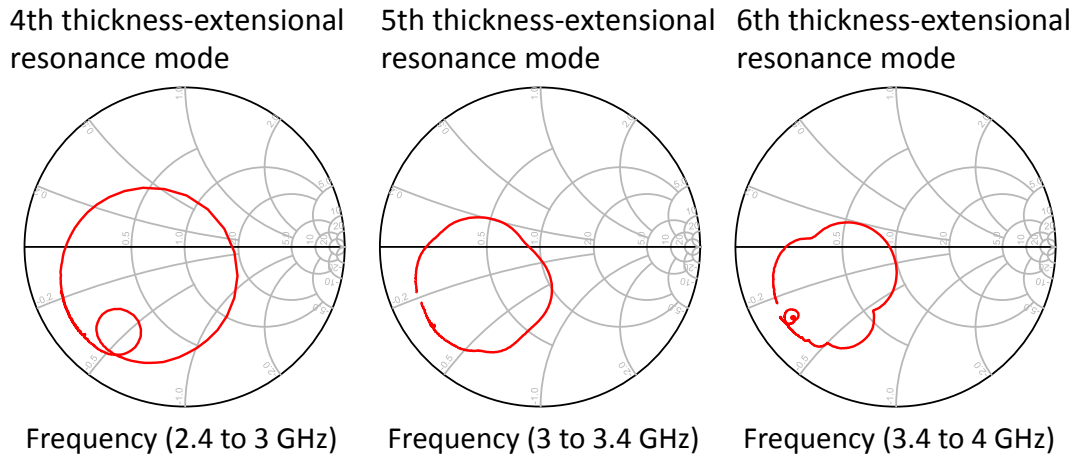


Figure 3.12: Measurement results for a typical BST-on-Si composite FBARs at different resonance mode. The FBAR area is $1600 \mu\text{m}^2$.

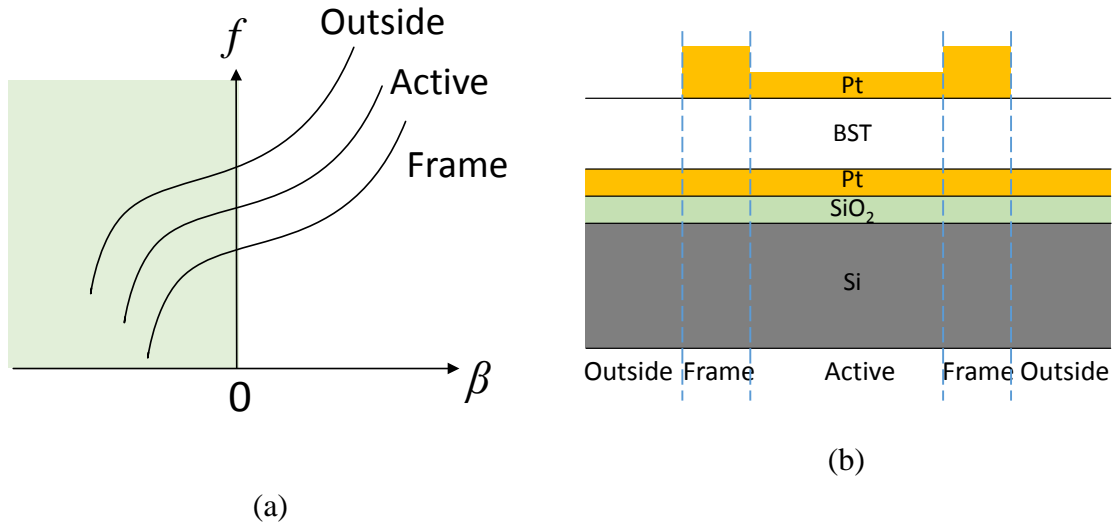


Figure 3.13: (a) Typical dispersion diagram for a type I resonator and (b) a cross-sectional view of BST-on-Si composite FBAR with a raised frame. This is not to scale.

The frame can be designed either by analyzing the dispersion diagram and solving for the new boundary conditions [72], [73] or by using FEM simulators like COMSOL Multiphysics. In this work, 2-D COMSOL simulations are performed to design a raised frame to eliminate higher-order lateral-wave spurious modes. Since material parameters for BST are not available in COMSOL Multiphysics, BST parameters are estimated from 1-D acoustic transmission line model simulation parameters in Table 3.3. Other than BST material parameters, COMSOL library parameters for other layers such as Pt, SiO_2 , and Si are used in the simulations. Once BST material parameters are found, optimal frame dimensions for the elimination of spurious modes can be selected through simulations. BST material parameters used in this work are provided in Chapter 3.3.4. The composite FBARs designed to have a maximized K_f^2 of 4% at 2 GHz with a raised frame for the lateral-wave spurious-modes elimination are fabricated for experimental verification.

3.3.3. Fabrication Procedure for Spurious-Free Composite BST FBARs for Maximum K_t^2

Fabrication of composite BST-on-Si FBARs is performed using a pre-platinized silicon-on-insulator (SOI) wafer. The SOI wafer is composed of a 4- μm -thick high-resistivity (100)-oriented device layer on a 1- μm -thick thermally-grown buried oxide layer. A 100-nm-thick platinum layer is patterned using reactive ion etching (RIE) to form the bottom electrode. A $\text{Ba}_{0.5}\text{Sr}_{0.5}\text{TiO}_3$ layer is deposited using an RF magnetron sputtering system with a substrate temperature of 650 °C so that the resonator frequency is 2 GHz. BST deposition is done using two sputtering guns with RF power levels of 300 W under a 25 mTorr pressure of Ar (80 sccm) and O_2 (20 sccm). Subsequently, a 100-nm-Pt layer is deposited and patterned by e-beam evaporation and lift-off to serve as the top electrode.

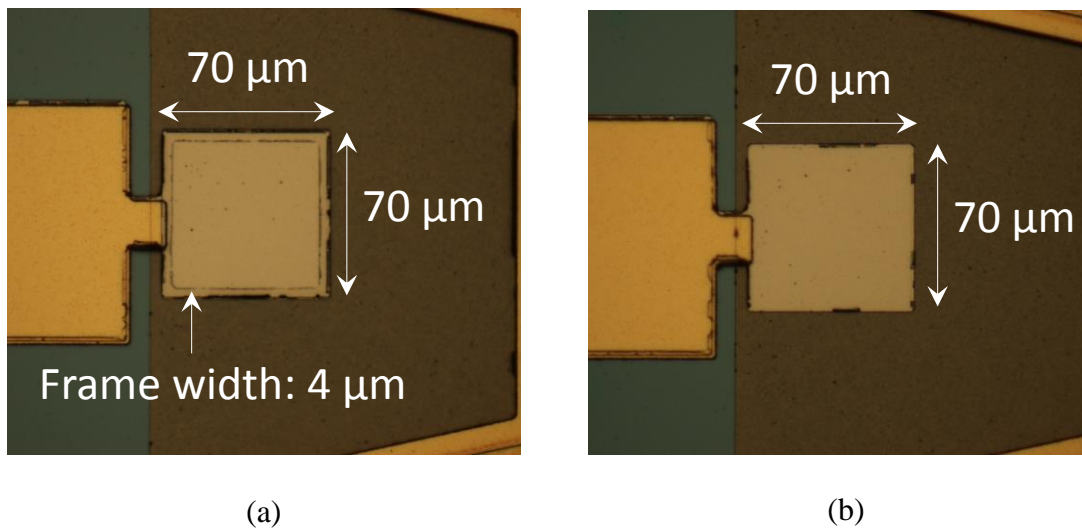
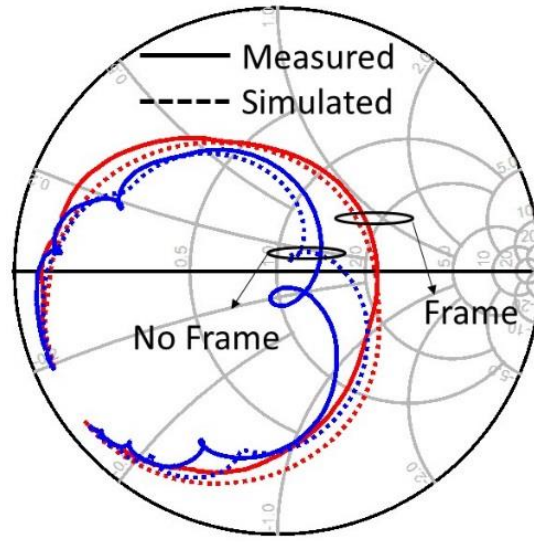


Figure 3.14: A photograph of a fabricated BST-on-Si composite FBAR (a) with a frame and (b) without a frame.

BST thin film is then selectively etched in diluted hydrofluoric acid (HF) to provide contact to the bottom electrode. Next, a Ti/Al/Ti/Au (50/1300/50/100 nm) layer is deposited and patterned to serve as a contact layer. A 30-nm-thick Pt layer is deposited to form a raised frame on edges of the top electrode. The 300- μm -thick Si-handling-layer is removed from backside using deep reactive ion etching (DRIE). Finally, a remaining buried oxide layer is wet etched in buffered HF (BHF) solution. A photograph of a fabricated resonator with and without a frame is shown in Fig. 3.14. Dimensions of both devices are identical except for the use of frame.

3.3.4. Measurement and Modeling Results

On-wafer measurements are performed on a probe station using a network analyzer and a ground-signal-ground (GSG) probe. On wafer short-open-load (SOL) calibration is performed. Measurement results of reflection coefficients for fabricated BST-on-Si composite FBARs are plotted on the Smith chart (Fig. 3.15) when devices are biased. Only the designed thickness extensional mode (3rd mode) is plotted. As can be seen, the use of frame helps eliminate dominant lateral-wave spurious modes. Shown in the same plot are corresponding COMSOL Multiphysics simulation results. In general, measurement and simulation results are in good agreement. In order to match the resonance frequency between measurement and simulation results, a silicon thickness in the simulation is adjusted from 4 to 4.07 μm . BST material parameters used in the COMSOL Multiphysics simulations are provided in Table 3.4, in which s , d , ϵ , ρ , η_{sE} , and $\eta_{\epsilon S}$ denote the compliance matrix component, coupling matrix component, relative permittivity, density, loss factor for compliance matrix, and loss factor for electrical permittivity, respectively.



Frequency (1.9 to 2.1 GHz)

Figure 3.15: Measured and simulated reflection coefficients on the Smith chart for fabricated BST-on-Si composite FBARs with and without a frame in Fig. 3.14.

Table 3.4

BST Material Parameters used in COMSOL Multiphysics Simulations

Parameter	Value	Parameter	Value
s_{11} (1/Pa)	5.8824×10^{-12}	d_{33} (C/N)	24×10^{-12}
s_{12} (1/Pa)	-1.7059×10^{-12}	d_{31} (C/N)	-9.6×10^{-12}
s_{44} (1/Pa)	1.5176×10^{-12}	d_{15} (C/N)	0
ϵ_{33}	115	ρ (kg/m ³)	5600
η_{sE}	1/300	η_{eS}	1/100

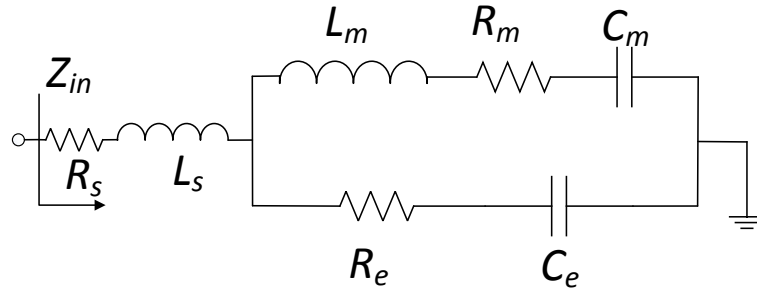


Figure 3.16: A schematic of mBVD model.

The linear modified Butterworth Van Dyke (mBVD) model in Fig. 3-16 is used for further analysis. The model parameters in Fig. 3.16 are found by fitting them to the measurement results. The complete model parameters are provided in Table 3.5.

Table 3.5

mBVD Model Parameters

Parameter	L_m (nH)	C_m (fF)	R_m (Ω)	C_e (pF)	R_e (Ω)	R_s (Ω)	L_s (nH)
Value	39.4	166	1.88	5.4	0.15	1.7	0.09

Figure 3.17 shows measured and modeled magnitude of input impedance for the FBAR with a frame in Fig. 3.14(a). FBAR figures of merit such as K_t^2 and quality factors can then be calculated from the model parameters in Table 3.5 and using (3-10)-(3-12).

$$Q_s = \frac{\omega_s L_m}{R_m + R_s} \quad (3-10)$$

$$Q_p = \frac{\omega_p L_m}{R_m + R_e} \quad (3-11)$$

$$Q_m = \frac{\omega_s L_m}{R_m} \quad (3-12)$$

K_t^2 , Q_s , Q_p , and Q_m are calculated to be 3.65%, 136, 244, and 259, respectively. Due to the presence of strong spurious modes for the FBAR without a frame in Fig. 3.14(b), FBAR quality factors and K_t^2 are difficult to calculate. However, it is obvious that such strong spurious modes in FBARs without a frame significantly degrade switchable BST FBAR performance.

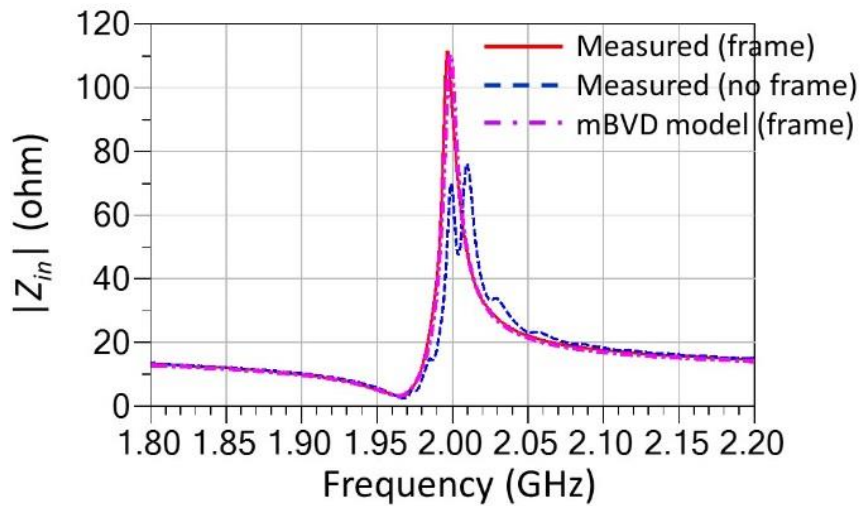


Figure 3.17: Magnitude of input impedance for measured/modeled FBAR with a frame and measured FBAR without a frame.

3.4. Chapter Conclusion

The design methods for intrinsically switchable ferroelectric BST-on-Si Composite FBARs are presented in this Chapter. First, the 1-D acoustic-transmission-line-model-based simulation is performed to design High- Q BST-on-Si composite FBARs. Using the 1-D model, the Q and K_t^2 are calculated as a function of BST-to-Si thickness ratio at the series resonance frequency of 2.5 GHz. Suitable BST and Si thicknesses and resonance mode are chosen to obtain a high- Q resonance response. Several switchable composite FBARs are fabricated and measured, exhibiting higher *quality factors* (>970) compared with BST based non-composite FBARs and SMRs. The composite FBARs are also suitable for low-power, low-phase-noise oscillator design.

Furthermore, temperature-dependent characteristics of high- Q intrinsically switchable $\text{Ba}_{0.5}\text{Sr}_{0.5}\text{TiO}_3$ -on-Si composite FBARs are presented. Measurement results show that the TCF is approximately -35 ppm/ $^\circ\text{C}$ for both f_s and f_p at the different bias voltage from 5 V to 40 V. The TCF value of switchable ferroelectric composite FBARs is comparable to that of Si resonators (-31 ppm/ $^\circ\text{C}$ [76]) and AlN resonators (-25 ppm/ $^\circ\text{C}$ [55]). The TCF of switchable composite FBARs can be reduced by including a SiO_2 layer with a positive TCF in the design of composite FBARs.

Based on the measurement results for high- Q composite BST FBARs, 1-D acoustic transmission line model parameters are modified to better represent BST material parameters fabricated using RF magnetron sputtering. 1-D acoustic transmission line model simulation is performed to design BST-on-Si composite FBAR so that the value of device K_t^2 is maximized, which is useful for the design of low-insertion-loss, wider-bandwidth filters. Furthermore, 2-D Multiphysics simulations are performed to design

frames in order to eliminate lateral-wave spurious-modes in intrinsically Switchable Ferroelectric BST-on-Si Composite FBARs. Measured results for fabricated devices show that careful design of a frame could eliminate the parasitic lateral modes, verifying the utility of using a frame to improve BST FBAR device performance.

Based on the BST-on-Si composite FBAR filter with the K_r^2 of 4% at 2 GHz presented here, a FBAR filter with a fractional bandwidth of 1.33% at 2 GHz is designed. Detailed design approach based on image parameter method, as well as comparison between measurement and simulation results are provided in Chapter 4.

CHAPTER IV

Design of Intrinsically Switchable RF Bulk Acoustic Wave Filters

4.1. Chapter Motivation

Bulk acoustic wave (BAW) filters are widely used in today's cell phones, especially since the number of frequency bands covered by the radio's RF front-end has been increased. Although the BAW filter's working principle is well known [77] and the state-of-the-art piezoelectric BAW filters provide excellent performance [56], [78], there has been less effort spent on the development of a complete set of design equations for BAW filters [79], [80]. The absence of a simple yet accurate, complete set of design equations makes filter designers rely on experience, empirical concepts, optimization and trial-and-error based design for such filters. This makes it hard to fully investigate the filter performance tradeoffs for the optimal filter design based on a given technology. The problem is magnified especially when a new technology is used for filter design, for example, recently-introduced switchable ferroelectric BAW resonators such as film bulk acoustic resonators (FBARs) and solidly mounted resonators (SMRs).

This section presents the design method for intrinsically switchable RF bulk acoustic wave filters based on ferroelectric BST-on-Si composite FBARs. Closed-form

design equations for ladder-type BAW filters based on the popular filter synthesis method using image parameters are introduced for the first time. The image impedance and propagation constant for a BAW filter are accurately calculated as a function of resonator and filter specifications including the resonator electromechanical coupling coefficient and filter fractional bandwidth. Moreover, the equations that can predict filter insertion loss, as well as rejection level are provided. To verify the validity of the design equations, a pi-type ladder bulk acoustic wave filter based on intrinsically switchable ferroelectric BST FBAR is designed, fabricated, and measured. Measurement results for a fabricated filter validate the proposed design method for ladder-type BAW filters.

4.2. Image Parameter Method Applicable to a Periodic Structure

Although the BST FBAR filter can be designed based on empirical approaches and optimization, it is extremely difficult to fully investigate the filter performance tradeoffs involved for the best filter design using empirical designs. Here, a BAW filter synthesis method that can allow accurate design of BAW filters is presented based on image parameter method. Figure 4.1 shows a schematic of a ladder-type BAW filter. Subscripts 1 and 2 denote series and shunt resonators, respectively. Since the ladder-type filter in Fig. 4.1 can be viewed as a periodic structure, the popular RF/microwave filter synthesis method called image parameter method [86]-[88] can be applied to the design of ladder-type filters.

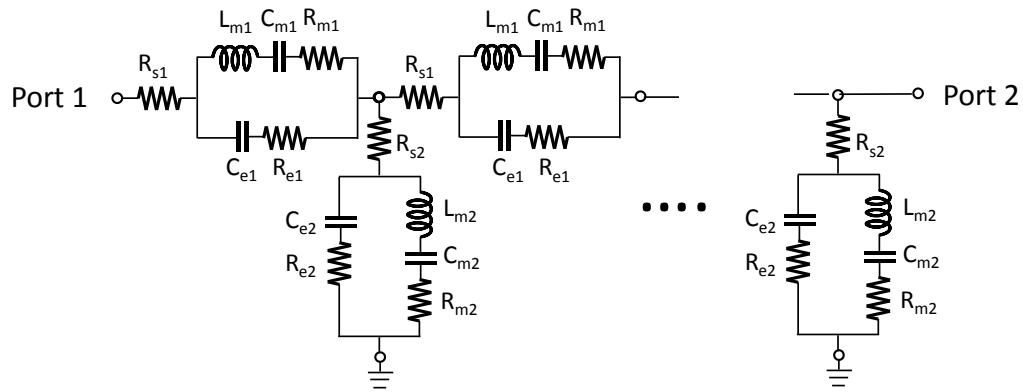


Figure 4.1: A schematic of a ladder-type BAW filter starting with a series resonator.

The idea of image parameter method is to design a unit cell for the filter first so that it exhibits the designed response, and then cascade unit cells to tailor filter rejection levels (Fig. 4.2). The design of a unit cell begins with determining two parameters: the image impedance and propagation constant. First, the image impedance (Z_i) of a unit cell is determined so that the input impedances at ports of a unit cell are matched to the system impedance Z_0 at the filter center frequency (Fig. 4.3). Next, the propagation constant ($\gamma = \alpha + j\beta$) is determined at the filter cutoff frequencies so that the signal passes through the unit cell with no attenuation in the passband, and be rejected in the stopband (Fig. 4.4).

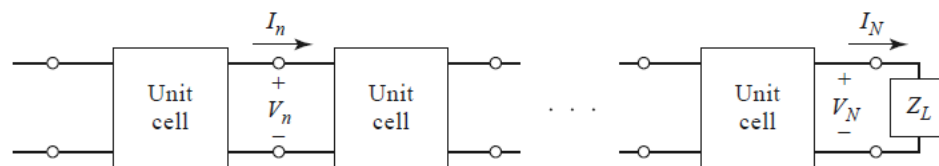


Figure 4.2: A schematic of a filter consisting of unit cells for which image parameter method can be applied in the filter design (reproduced from [88]).

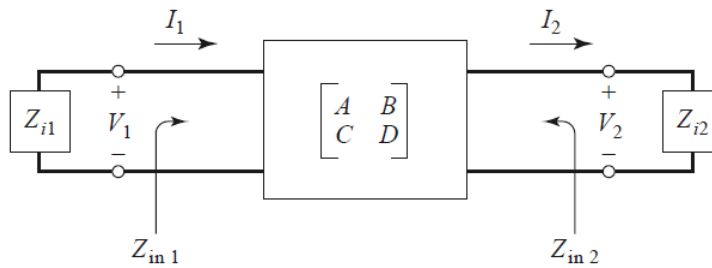


Figure 4.3: A filter unit cell terminated in its image impedances (reproduced from [88]).

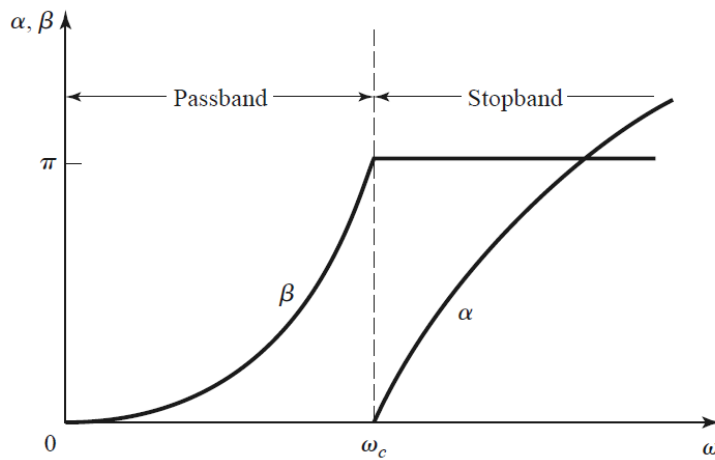


Figure 4.4: Typical propagation constant (γ) characteristics of a bandpass filter in the passband and the stopband. Attenuation constant (α) and phase constant (β) are shown (reproduced from [88]).

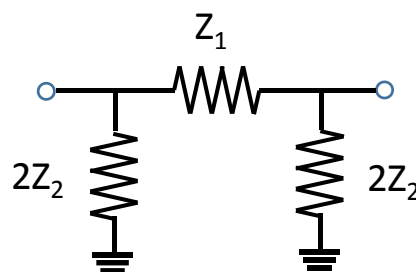


Figure 4.5: Schematic of a general pi-type network.

Shown in Fig. 4.5 is a schematic of a general pi-type network, for which Z_i , e^γ , and $\cosh(\gamma)$ can be expressed as a function of Z_1 and Z_2 in Fig. 4.5 [88].

$$Z_{i\pi} = \sqrt{Z_1 Z_2} / \sqrt{1 + Z_1 / 4Z_2} \quad (4-1)$$

$$e^\gamma = 1 + Z_1 / 2Z_2 + \sqrt{Z_1 / Z_2 + Z_1^2 / 4Z_2^2} \quad (4-2)$$

$$\cosh(\gamma) = 1 + Z_1 / 2Z_2 \quad (4-3)$$

This basic structure and its image parameters are used to form and synthesize a unit cell for the ladder-type BAW filter.

4.3. Calculation of Image Impedance for BAW Filters

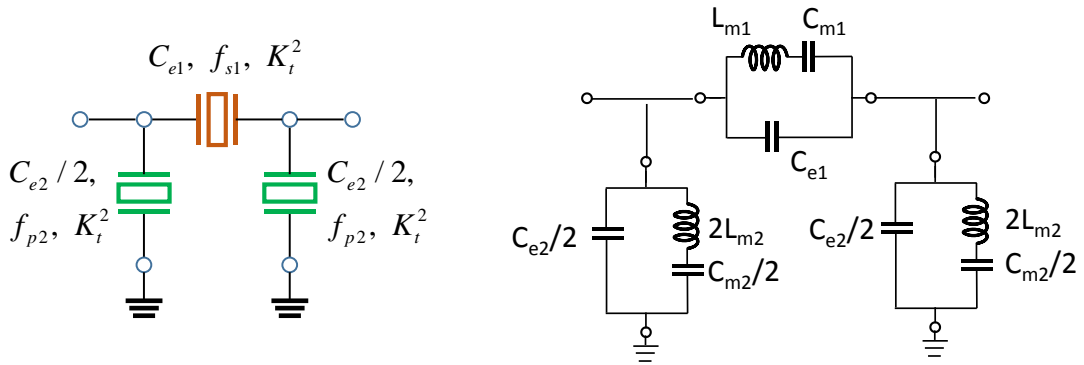


Figure 4.6: A schematic of a pi-type unit cell for ladder-type BAW filter in terms of (a) device parameters C_e, f_{s1} (or f_{p1}), and K_t^2 and (b) circuit parameters C_e, C_m , and L_m .

Figures 4.6(a) and 4.6(b) show a π -type unit cell for a ladder-type FBAR filter where device parameters are C_e, K_t^2, f_s (or f_p) and circuit parameters are C_e, C_m , and L_m ,

respectively. The relationship between these parameters and ADS models can be found in Appendix A and B. Subscripts 1 and 2 denote series and shunt resonators, respectively. The series and shunt impedances in Fig. 4.6(b) can be expressed as follows:

$$Z_1 = \left[\left(j\omega L_{m1} + \frac{1}{j\omega C_{m1}} \right)^{-1} + \left(\frac{1}{j\omega C_{e1}} \right)^{-1} \right]^{-1} = j \frac{\omega^2 L_{m1} C_{m1} - 1}{\omega(C_{m1} + C_{e1}) - \omega^3 L_{m1} C_{m1} C_{e1}} \quad (4-4)$$

$$2Z_2 = 2 \left[\left(j\omega L_{m2} + \frac{1}{j\omega C_{m2}} \right)^{-1} + \left(\frac{1}{j\omega C_{e2}} \right)^{-1} \right]^{-1} = j \frac{2(\omega^2 L_{m2} C_{m2} - 1)}{\omega(C_{m2} + C_{e2}) - \omega^3 L_{m2} C_{m2} C_{e2}} \quad (4-5)$$

By setting the series resonance frequency of a series resonator (f_{s1}) and the parallel resonance frequency of shunt resonators (f_{p1}) in Fig. 4.6(a) to the center frequency of a filter (f_c)

$$f_{s1} = f_c \quad (4-6)$$

$$f_{p2} = f_c, \quad (4-7)$$

the circuit parameters in Fig. 4.6(b) can be related to the device parameters in Fig. 4.6(a) as shown below.

$$L_{m1} C_{m1} = \frac{1}{\omega_c^2} \quad (4-8)$$

$$L_{m2}C_{m2} = \frac{1}{\omega_c^2} \left(\frac{C_{e2} + C_{m2}}{C_{e2}} \right) = \frac{1}{\omega_c^2} A \quad (4-9)$$

in (4-9), A is defined as follows (see Appendix A for the derivation):

$$A = 1 + \frac{C_m}{C_e} = \frac{4}{\left(1 + \sqrt{1 - \frac{16K_t^2}{\pi^2}} \right)^2} \quad (4-10)$$

It is noted that Z_1 in (4-4) and Z_2 in (4-5) approaches zero and infinity at the filter center frequency ($\omega = \omega_c$) with (4-8) and (4-9). Therefore, (4-1) can be simplified to (4-11).

$$Z_{i\pi} = \sqrt{Z_1 Z_2} / \sqrt{1 + Z_1 / 4Z_2} = \sqrt{Z_1 Z_2} \quad (4-11)$$

Substituting Z_1 in (4-4) and Z_2 in (4-5) into (4-11) leads to

$$Z_{i\pi} = \sqrt{\frac{\omega^2 L_{m1} C_{m1} - 1}{\omega(C_{m1} + C_{e1}) - \omega^3 L_{m1} C_{m1} C_{e1}}} \times \frac{1 - \omega^2 L_{m2} C_{m2}}{\omega(C_{m2} + C_{e2}) - \omega^3 L_{m2} C_{m2} C_{e2}}. \quad (4-12)$$

Inserting (4-8)-(4-10) into (4-12) leads to (4-13).

$$Z_{i\pi} = \frac{1}{\omega} \sqrt{\frac{\omega^2 - \omega_c^2}{\omega_c^2 A C_{e1} - \omega^2 C_{e1}}} \times \frac{\omega_c^2 - \omega^2 A}{(\omega_c^2 - \omega^2) A C_{e2}} \quad (4-13)$$

By using (4-14) and (4-15)

$$\omega = \omega_c + \delta\omega_c \quad (0 < \delta\omega_c \ll \omega_c) \quad (4-14)$$

$$\omega^2 = \omega_c^2 + 2\omega_c\delta\omega_c + (\delta\omega_c)^2 = \omega_c^2 + 2\omega_c\delta\omega_c \quad (4-15)$$

(4-13) can be simplified to (4-16)

$$Z_{i\pi} = \frac{1}{\omega_c + \delta\omega_c} \sqrt{\frac{1}{C_{e1}C_{e2}A} \times \frac{(\omega_c^2 + 2\omega_c\delta\omega_c)A - \omega_c^2}{\omega_c^2A - (\omega_c^2 + 2\omega_c\delta\omega_c)}}, \quad (4-16)$$

and further to (4-17) by letting $\delta\omega_c$ approach zero and using $Z_{i\pi}=Z_0$.

$$Z_0 = \frac{1}{\omega_c} \sqrt{\frac{1}{C_{e1}C_{e2}A}} \quad (4-17)$$

Therefore, the multiplication of C_{e1} and C_{e2} is expressed as a function of filter center frequency, system impedance, A and thus K_f^2 (see (4-10)).

$$C_{e1}C_{e2} = \frac{1}{(\omega_c Z_0)^2 A} \quad (4-18)$$

It is noted that when $K_t^2 \ll 1$, (4-18) can be approximated by (4-19) as reported in [79], [80].

$$C_{e1}C_{e2} = \frac{1}{(\omega_c Z_0)^2} \quad (4-19)$$

4.4. Calculation of Propagation Constant for BAW Filters

The calculation of propagation constant for BAW filters has never been reported, and the analytical method of bandwidth control has not been available. Therefore, often BAW filter design usually relies on experience and optimization to meet the required filter specifications [77], [78], [81]. At the bandpass filter cutoff frequencies, the $\cosh(\gamma)$ should be zero [88], which leads to the following relationship.

$$\cosh \gamma = 1 + \frac{Z_1}{2Z_2} = 0 \text{ at } \omega_1 \text{ and } \omega_2 \quad (4-20)$$

in (4-20), ω_1 and ω_2 can be expressed as a function of the filter angular center frequency (ω_c) and filter fractional bandwidth (Δ).

$$\omega_1 = \omega_c (1 - \Delta/2) \quad (4-21)$$

$$\omega_2 = \omega_c (1 + \Delta/2) \quad (4-22)$$

Inserting Z_1 in (4-4) and Z_2 in (4-5) into (4-20) results in (4-23), which can be further simplified into (4-24) using (4-10).

$$\frac{\omega^2 L_{m1} C_{m1} - 1}{(C_{m1} + C_{e1}) - \omega^2 L_{m1} C_{m1} C_{e1}} = \frac{-2\omega^2 L_{m2} C_{m2} + 2}{(C_{m2} + C_{e2}) - \omega^2 L_{m2} C_{m2} C_{e2}} \quad (4-23)$$

$$\frac{C_{e2}}{C_{e1}} \times \frac{\omega^2 - \omega_c^2}{\omega_c^2 A - \omega^2} = \frac{-2\omega^2 A + 2\omega_c^2}{(\omega_c^2 - \omega^2) A} \quad (4-24)$$

Equation (4-24) can be expressed as (4-25) in which X , B , and Y are defined in (4-26).

$$B \times \frac{X - Y}{YA - X} = \frac{-2XA + 2Y}{AY - AX} \quad (4-25)$$

$$X = \omega^2, \quad B = \frac{C_{e2}}{C_{e1}}, \quad Y = \omega_c^2 \quad (4-26)$$

Equation (4-25) is a quadratic function with respect to X , and two solutions X_2 and X_1 are expressed as (4-27) and (4-28) using (4-21) and (4-22).

$$X_2 = [\omega_c (1 + \Delta / 2)]^2 \quad (4-27)$$

$$X_1 = [\omega_c (1 - \Delta / 2)]^2 \quad (4-28)$$

Solving (4-25) for X , and simplifying it using (4-27) and (4-28) results in (4-29).

$$\Delta = \frac{(A-1)\sqrt{A^2 + 2A + 1 + 2AB}}{A(B+2)} \quad (4-29)$$

Eventually (4-29) can be simplified to (4-30):

$$\frac{C_{e2}}{C_{e1}} = \frac{(A-1)^2}{\Delta^2 A} \left(1 + \sqrt{1 + \Delta^2}\right) - 2 \quad (4-30)$$

Therefore, the ratio of C_{e2} to C_{e1} is expressed as a function of filter fractional bandwidth (Δ), as well as A and thus K_f^2 (see (4-10)). At this point, given (4-18) and (4-30) along with (4-8)-(4-10), circuit parameters of a pi-type BAW filter unit cell in Fig. 4.6 can be expressed as closed-form equations given by (4-31)-(4-36).

$$C_{e1} = \left(\frac{1}{\omega_c Z_0 \sqrt{A}} \right) \div \sqrt{\frac{(A-1)^2}{\Delta^2 A} \left(1 + \sqrt{1 + \Delta^2}\right) - 2} \quad (4-31)$$

$$C_{e2} = \left(\frac{1}{\omega_c Z_0 \sqrt{A}} \right) \times \sqrt{\frac{(A-1)^2}{\Delta^2 A} \left(1 + \sqrt{1 + \Delta^2}\right) - 2} \quad (4-32)$$

$$C_{m1} = C_{e1} \times \left[4 \div \left(1 + \sqrt{1 - \frac{16K_f^2}{\pi^2}} \right)^2 - 1 \right] \quad (4-33)$$

$$C_{m2} = C_{e2} \times \left[4 \div \left(1 + \sqrt{1 - \frac{16K_f^2}{\pi^2}} \right)^2 - 1 \right] \quad (4-34)$$

$$L_{m1} = \frac{1}{C_{m1}\omega_c^2} \quad (4-35)$$

$$L_{m2} = \frac{1}{C_{m2}\omega_c^2} \times \left[4 \div \left(1 + \sqrt{1 - \frac{16K_t^2}{\pi^2}} \right)^2 - 1 \right] \quad (4-36)$$

4.5. Filter Insertion Loss and Rejection Level Prediction

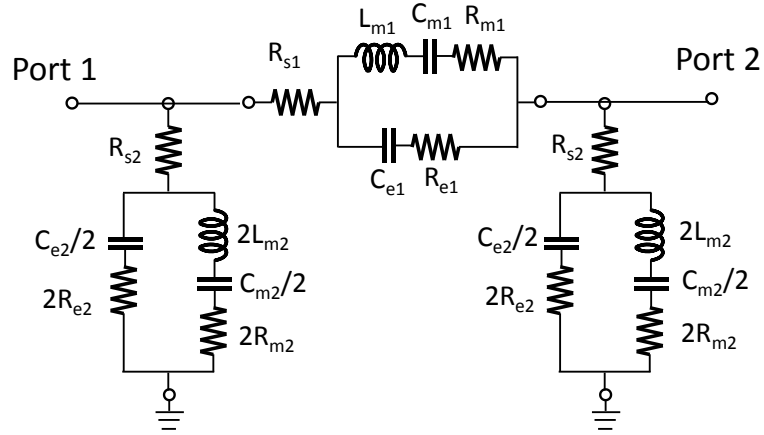


Figure 4.7: A schematic of a pi-type unit cell for ladder-type BAW filter including device loss terms (R_m , R_s , and R_e).

Since practical FBARs are lossy, their loss characteristics should also be modeled to predict FBAR filter insertion loss. For this purpose, the commonly-used FBAR mBVD (modified Butterworth Van Dyke) model in Fig. 4.7 is used, which includes FBAR device loss components such as R_m , R_e , and R_s [89]. Here, R_m and R_e are a function of mechanical quality factor in (4-37) and electrical quality factor in (4-38). R_s represents ohmic loss from electrodes and interconnects.

$$Q_m = \omega_s \frac{L_m}{R_m} \quad (4-37)$$

$$Q_e = \frac{1}{\omega_p C_e R_e} \quad (4-38)$$

To predict any filter insertion loss, it is important to build the equivalent circuit at the filter center frequency [82]. Similar to the analysis made for transformation between series and parallel RLC tanks [90], the BAW filter equivalent circuit can be drawn as seen in Fig. 4.8.

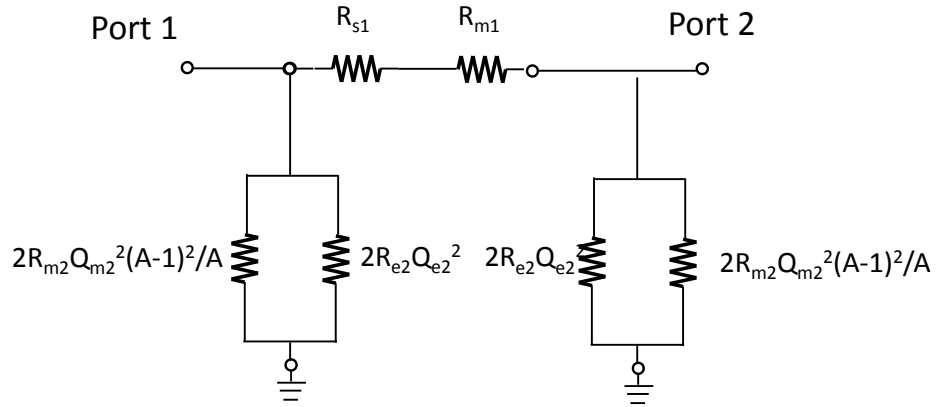


Figure 4.8: Equivalent circuit of Fig. 4.7 at the filter center frequency. The circuit consists of resistors which represent device loss terms (R_m , R_s , and R_e).

Once the filter's equivalent circuit at the center frequency which consists of resistors is made, the filter insertion loss in Fig. 4.8 can be calculated similar to [82].

$$IL_\pi = 4.343 \times \left[\frac{R_{m1} + R_{s1}}{Z_0} + \frac{Z_0 A}{R_{m2} Q_{m2}^2 (A-1)^2} + \frac{Z_0}{R_{e2} Q_{e2}^2} \right] \text{ (dB)} \quad (4-39)$$

Similarly, filter rejection level in the stopband can be predicted by determining its equivalent circuit in the stopband, which is shown in Fig. 4.9.

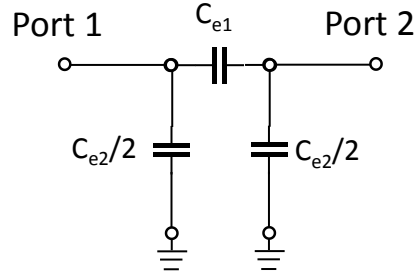


Figure 4.9: Equivalent circuit of Fig. 4.7 in the stopband. The circuit consists of electrical capacitors only (C_{e1} and C_{e2}).

It is noted that due to the narrow bandwidth characteristic of BAW resonators, only C_e is needed to model the BAW filter response in its stopband [56], [78], [81]. By calculating the ABCD parameters of the circuit in Fig. 4.9 in (4-40) and converting it into S_{21} (4-41), one can accurately predict filter rejection level.

$$ABCD = \begin{bmatrix} 1 + \frac{C_{e2}}{2C_{e1}} & \frac{1}{\omega C_{e1}} \\ \omega C_{e2} & 1 + \frac{C_{e2}}{2C_{e1}} \end{bmatrix} \quad (4-40)$$

$$S_{21} = \frac{2}{A + B/Z_0 + CZ_0 + D} \quad (4-41)$$

4.6. Design Considerations for BAW Filters

It should be noted that a complete set of design equations presented here can be applied to the design of any type of BAW filters, regardless of type of materials employed (i.e. piezoelectric materials such as AlN, PZT, ZnO, etc. or ferroelectric materials such as BST, STO, BTO, etc.). This is because their equivalent circuit models are the same as the one shown in Fig. 4.7. Furthermore, since the filter unit cell in Fig. 4.7 is symmetric and has the same image impedance seen at both ports looking into the network, the unit cell can be simply cascaded to form a higher-order filter. It can provide a higher rejection level at the cost of increased insertion loss, which can be estimated by modifying (4-39)-(4-41) to (4-42)-(4-44). In (4-42)-(4-44), n is the number of cascaded unit cells.

$$IL_{\pi,n} = 4.343 \times \left[\frac{R_{m1} + R_{s1}}{Z_0} + \frac{Z_0 A}{R_{m2} Q_{m2}^2 (A-1)^2} + \frac{Z_0}{R_{e2} Q_{e2}^2} \right] \times n \text{ (dB)} \quad (4-42)$$

$$ABCD_n = \begin{bmatrix} 1 + \frac{C_{e2}}{2C_{e1}} & \frac{1}{\omega C_{e1}} \\ \omega C_{e2} & 1 + \frac{C_{e2}}{2C_{e1}} \end{bmatrix}^n = \begin{bmatrix} A_n & B_n \\ C_n & D_n \end{bmatrix} \quad (4-43)$$

$$S_{21,n} = \frac{2}{A_n + \frac{B_n}{Z_0} + C_n Z_0 + D_n} \quad (4-44)$$

The development of closed-form design equations presented here enables BAW filter designers to accurately predict filter performance and tradeoffs involved, so as to obtain

the best possible filter design, while reducing the number of optimization iteration in the design of BAW filters.

4.7. Ladder-Type BAW Filter Design Example

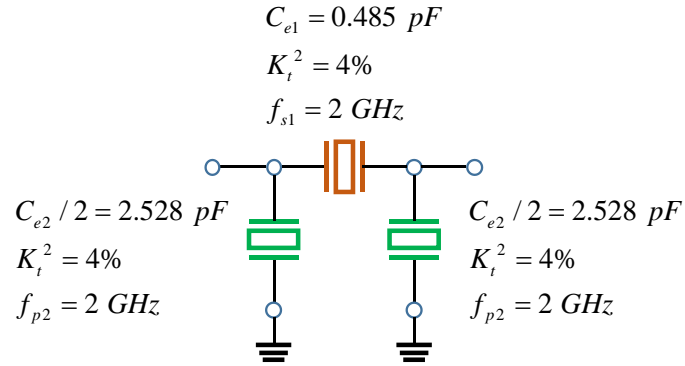
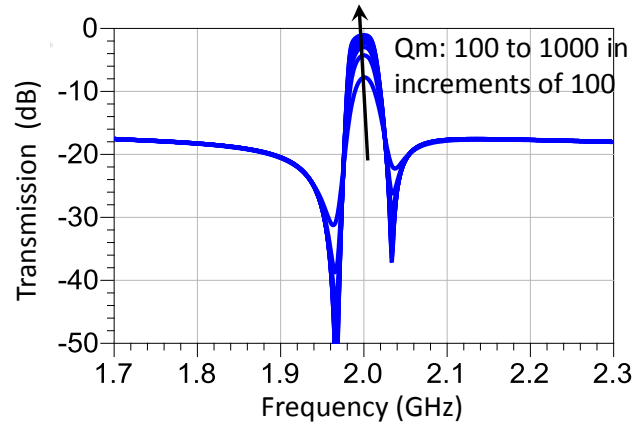
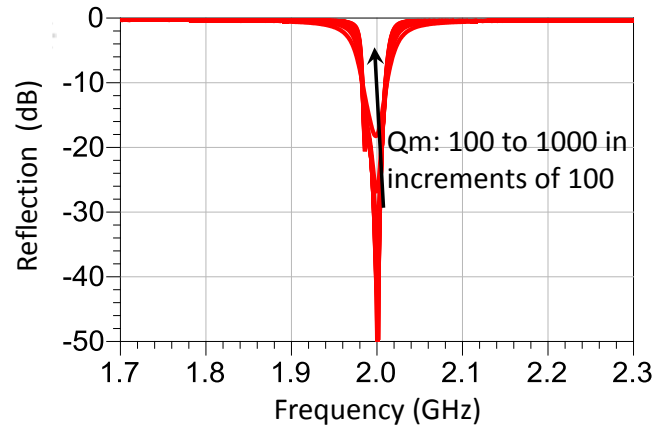


Figure 4.10: Schematic of the designed filter with calculated device parameters.

As a design example, an intrinsically switchable FBAR filter based on ferroelectric thin film BST is designed, fabricated, and measured. As a proof-of-concept, a simple π -network filter in Fig. 4.10 is designed. A fractional bandwidth (FBW) is intentionally selected to become a third of FBAR K_t^2 at a filter design frequency of 2 GHz to show the ability of bandwidth control presented in this work. In conventional BAW filter design [81], FBW is empirically determined by $FBW=2K_t^2$ and FBW is not a design parameter.



(a)



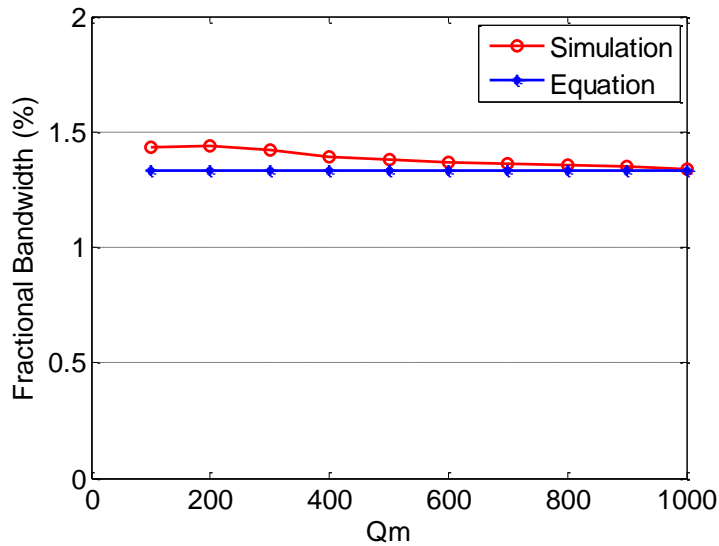
(b)

Figure 4.11: ADS simulation results of (a) transmission (S21) and (b) reflection (S11) for the designed filter in Fig. 4.10. Q_m is varied from 100 to 1000 in increments of 100.

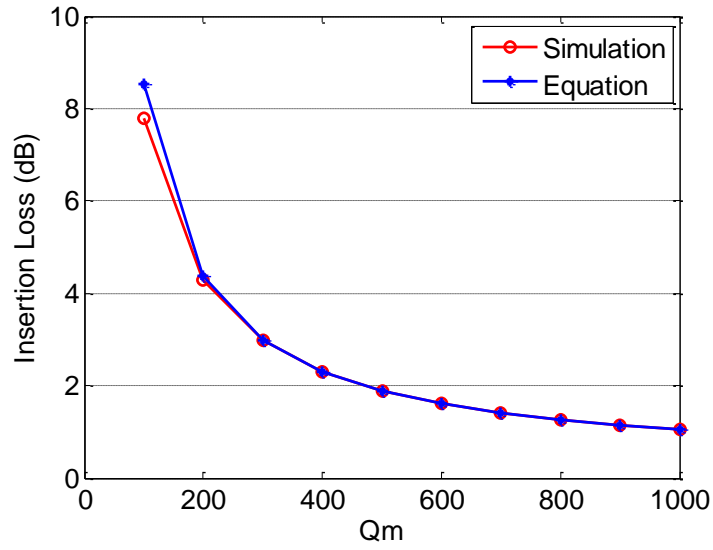
The ferroelectric BST-on-Si composite FBAR K_t^2 is estimated to be 4% when the resonator is at its on-state, therefore, the expected filter fractional bandwidth is 1.33% at 2 GHz. With these specifications, FBAR filter electrical parameters are calculated using a complete set of design equations using (4-31) and (4-32); C_{e1} and C_{e2} are calculated to be

0.5 pF and 5.058 pF, respectively. Other circuit parameters are then determined by (4-33)-(4-38). Filter insertion loss and rejection level can be predicted by (4-42)-(4-44). Schematics of the designed filter with calculated device parameters and circuit parameters are shown in Fig. 4.10(a) and Fig. 4.10(b), respectively. Figure 4.11 shows ADS [91] circuit simulation results for the designed filter in Fig. 4.10 with Q_m varied from 100 to 1000 in increments of 100.

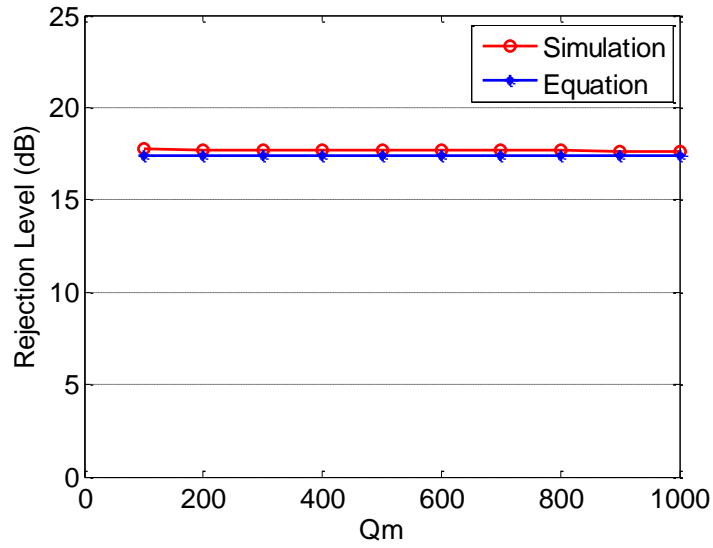
Figure 4.12 shows the comparison between circuit simulation and predicted results for fractional bandwidth, insertion loss, and rejection level as a function of quality factor from 100 to 1000 in increments of 100. As seen in Figs. 4.11 and 4.12, the circuit simulation results clearly indicate the accuracy of the proposed design method based on image parameters. The designed filter here is fabricated for the experimental verification.



(a)



(b)



(c)

Figure 4.12: Comparison between circuit simulation and predicted results for (a) fractional bandwidth defined as frequency in which $S_{11} < -10$ dB, (b) minimum insertion loss, and (c) rejection level with quality factors from 100 to 1000 in increments of 100.

4.8. Fabrication Procedure and Measurement Setup for BAW Filters

A switchable BST-on-Si composite FBAR filter is fabricated on a pre-platinized silicon-on-insulator (SOI) wafer with 100-nm platinum (Pt), 200-nm SiO₂-buffer, 5- μ m Si-device, 200-nm buried-oxide, and 300- μ m Si-handle layer thicknesses. First, the Pt layer is selectively patterned to serve as the bottom electrode using reactive ion etching (RIE). Subsequently, a BST (Ba_{0.5}Sr_{0.5}TiO₃) layer is deposited using RF magnetron sputtering so that its resonance frequency is 2 GHz. In the RF magnetron sputtering system, the growth temperature is set to 650 °C with 4:1 Ar/O₂ total pressure of 25 mTorr.

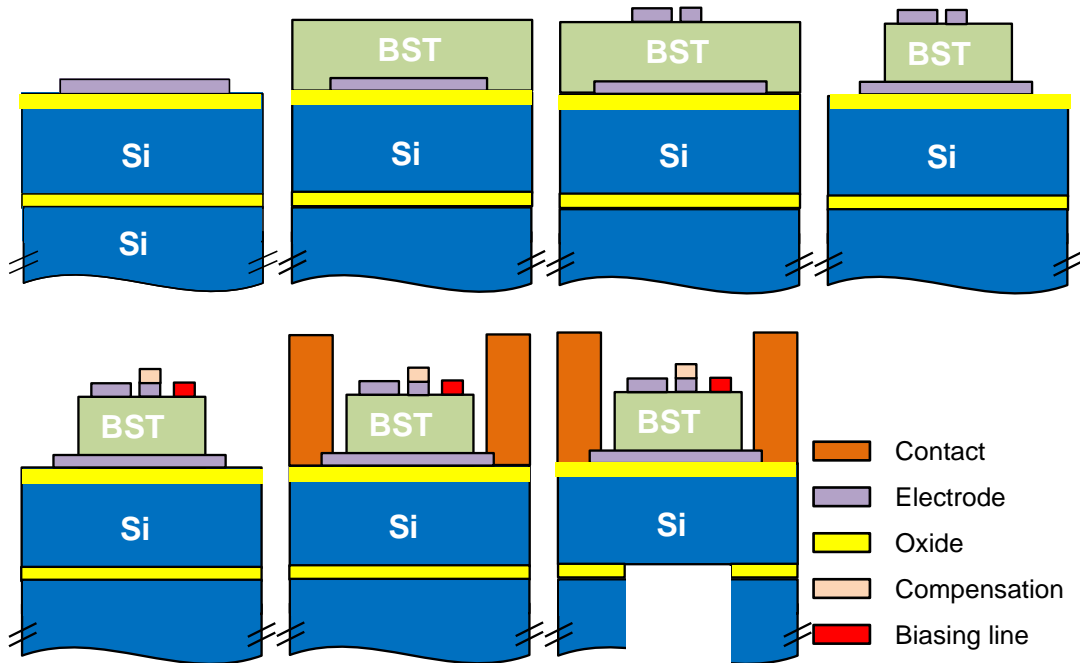


Figure 4.13: Intrinsic switchable BST FBAR filter fabrication procedure.

Another 100-nm-thick Pt layer is then deposited and patterned using e-beam evaporation and liftoff. After annealing is performed at 500 °C for 30 minutes, the BST

layer is etched in diluted HF (10:1) solution. In order to shift the resonance frequencies of shunt resonators in a filter, a thin Ti/Pt layer is deposited as a mass-loading layer on shunt resonators. Subsequently, biasing lines are fabricated using a high-resistivity NiCr layer. A thick metal layer (50/1300/50/100-nm-thick Ti/Al/Ti/Au) is deposited as contact layer. Finally, the BST-on-Si composite FBAR device is released by etching the 300- μm -thick Si-handle layer using deep reactive ion etching (DRIE) and then etching the 200-nm-thick buried-oxide layer in BHF solution. A step-by-step BST FBAR filter fabrication procedure is provided in Figure 4.13. The microphotograph of a BST FBAR filter is shown in Fig. 4.14(a) and its corresponding circuit schematic is provided in Fig. 4.14(b).

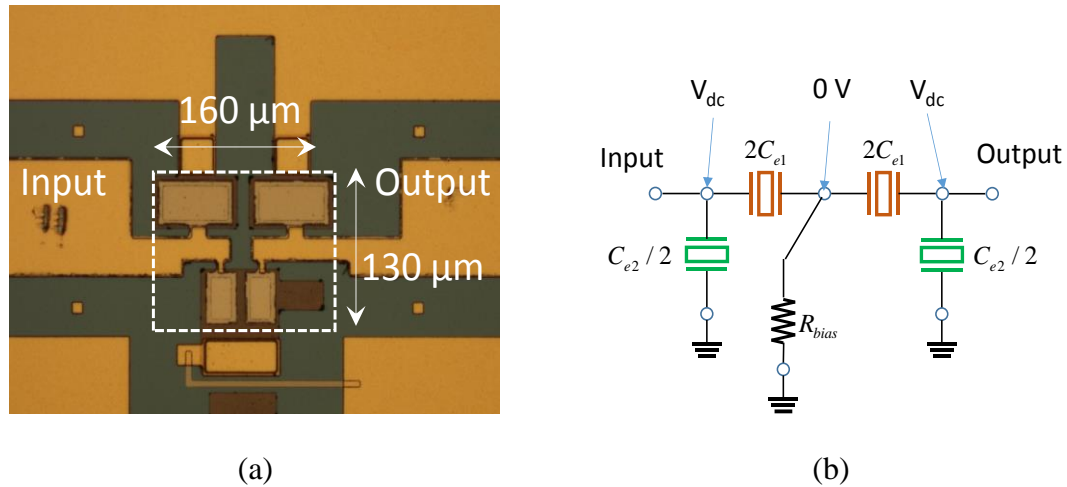


Figure 4.14: (a) A photograph of the fabricated π -type switchable ferroelectric BST FBAR filter and (b) its corresponding circuit schematic. R_{bias} is designed to be 1 kohm. Two double-sized FBARs are connected in series for easier biasing.

Measurements are performed on a probe station with an Agilent E8364C network analyzer. Short-open-load-thru (SOLT) calibration is performed with 250- μm pitch

ground-signal-ground (GSG) probes. Bias tees are used at the filter input and output to provide a dc bias voltage to turn on ferroelectric BST material's voltage-induced piezoelectricity (electrostriction) [3], [4], leading to a switchable filter.

The S parameters of the fabricated devices are measured using 250- μm pitch ground-signal-ground (GSG) probes and an Agilent E8364C network analyzer. The open-short-load-through calibration is performed from 0.1 to 5 GHz in the 50- Ω system impedance. The measurement setup is shown in Fig. 4.15.

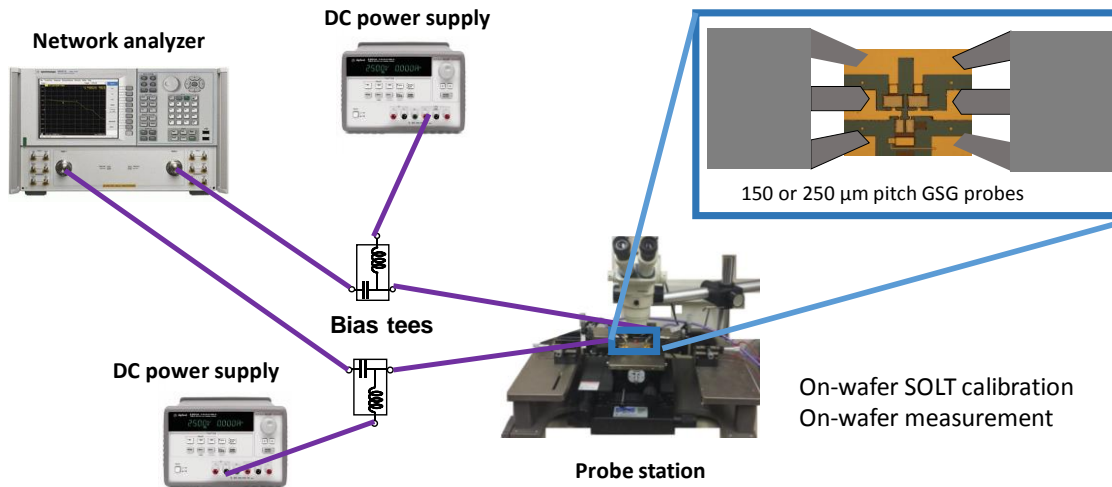
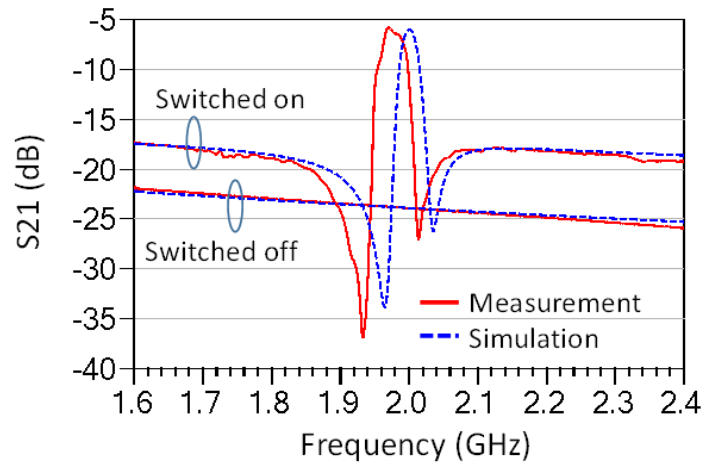


Figure 4.15: Intrinsicly Switchable BST FBAR Filter measurement setup.

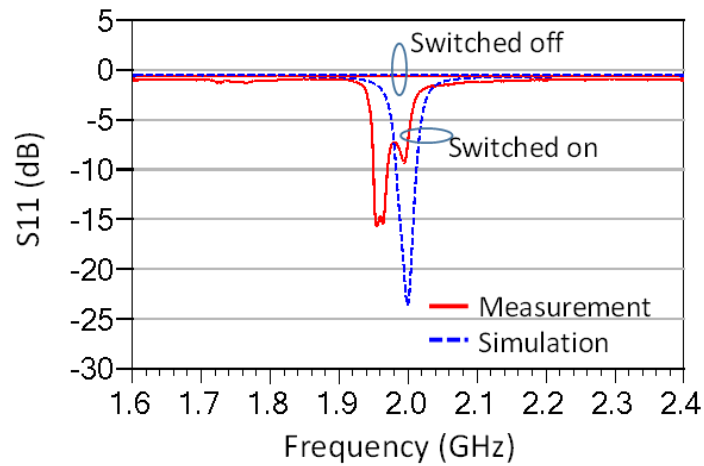
4.9. BST FBAR Filter Measurement Results

Measurement results for a fabricated switchable filter are provided in Fig. 4.16. When a bias voltage ($V_{dc}=65\text{ V}$) is applied, the device exhibits bandpass filter response as shown in Fig. 4.16. The minimum insertion loss is measured to be 5.77 dB and a 1-dB filter bandwidth is measured to be 24 MHz equivalent to 1.22% at a filter center frequency of

1.97 GHz. The device is in its off-state when the bias voltage is turned off (i.e. $V_{dc}=0$), providing more than 22-dB isolation between input and output ports.



(a)



(b)

Figure 4.16: Measured and simulated (a) transmission and (b) reflection results for a fabricated switchable ferroelectric BST FBAR filter.

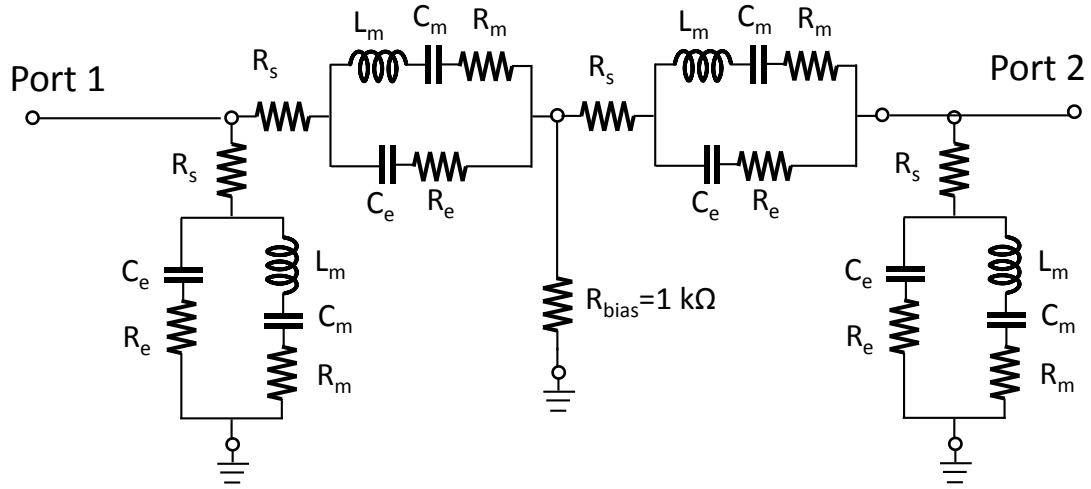


Figure 4.17: Equivalent circuit for the FBAR filter shown in Fig. 4.14(b). Circuit parameters are given in Table 4.2.

Shown in the same figure are filter circuit simulation results. The estimated Q value for each FBAR device is 150. As can be seen, the simulation results are in very good agreement with the measurement results. Due to the tolerance in fabrication, the measured filter center frequency is down-shifted. Complete device and circuit parameters used in the simulation (Fig. 4.16) are provided in Tables 4.1 and 4.2. The filter equivalent circuit for Fig. 4.14(b) consisting of mBVD models is provided in Fig. 4.17. Despite of high insertion loss (5.77 dB) due to the relatively low film quality in BST sputtered in this work, the described filter design method predicts the device performance very well, validating the proposed method.

Table 4.1

Complete Simulation Parameters (Device Parameters)

FBARs	f_s (GHz)	f_p (GHz)	K_t^2 (%)	C_e (pF)	Q_m	Q_e	R_s (Ω)
Shunt	1.967	2	4	2.528	150	100	2
Series	2	2.033	4	0.969	150	100	2

Table 4.2

Complete Simulation Parameters (Circuit Parameters)

FBARs	L_m (nH)	C_m (pF)	C_e (pF)	R_m (Ω)	R_e (Ω)	R_s (Ω)
Shunt	76.62	0.0854	2.528	6.31	0.31	2
Series	193.30	0.0328	0.969	16.19	0.81	2

4.10. Chapter Conclusion

The design method for BAW filters is presented based on the filter synthesis method using the image impedance and propagation constant. A complete set of design equations is derived for the first time. Measurement results for a switchable BST FBAR filter are in agreement with circuit simulation results, which validates the proposed design method presented here. It is noted that the derived closed-form design equations can be utilized for the design of general BAW filters as the equivalent circuit model is identical, regardless of the materials used in the implementation of BAW filters.

It is worthwhile to mention that there is much room to reduce the insertion loss of BST FBAR filters by optimizing thin-film growth conditions in an RF magnetron

sputtering system. Many thin-film BST growth conditions used so far are optimized for high-tunability BST varactor fabrication. The growth conditions in this work have not been characterized and optimized yet for BST FBAR applications. It is recently found that the Q_m of BST SMRs can improve approximately by a factor of 3 with the growth temperature using an RF magnetron sputtering system [48]. Similarly, optimal growth conditions for BST FBARs could allow for the significant improvement in Q_m , which will in turn reduce filter insertion loss considerably. Moreover, filter insertion loss can be further reduced by optimizing the geometry of the plates and interconnects to reduce the associated ohmic losses.

CHAPTER V

Conclusion

5.1. Summary of contribution

This dissertation presents a new promising technology for the design of *switchable BAW filters* based on *electrostrictive effect in BST thin films for frequency-agile communication systems*. Contributions of this work are categorized into three major parts. First, the *nonlinear circuit modeling* procedure for intrinsically switchable ferroelectric BST FBARs has been presented for the first time. The nonlinear circuit model, which is essential for the material characterization as well as device characterization, has been developed based on the physics of electrostriction-based intrinsically switchable FBARs. The developed model has been implemented in a circuit simulator and modeling results are in close agreement with measured bias-voltage and RF-power-level dependent behavior of BST FBAR devices.

Second, the BST-on-Si composite FBAR *design methods* have been presented. The high- Q BST-on-Si composite FBAR has been designed based on 1-D acoustic transmission line model, exhibiting *a record measured Q of 970 at 2.5 GHz* among switchable BST FBARs (previously reported Q is 800 at 1.28 GHz achieved by our group [23]).

Furthermore, a raised-frame technique, which has been used to *eliminate lateral-wave spurious-modes* in piezoelectric BAW resonators, has been employed for switchable ferroelectric BST FBARs, demonstrating the effectiveness of the frame technique. The design is based on 2-D Multiphysics simulation to predict and eliminate spurious lateral-wave mode excitations.

Finally, a *filter design method* for ladder-type BAW filters has been presented. The *filter synthesis approach for BAW filters has been developed based on image parameter method*. Closed-form equations have been derived for the first time enabling one to accurately design BAW filters. A systematically-designed pi-type intrinsically switchable BST FBAR filter has been fabricated and measured, exhibiting a 5.77-dB insertion loss and 1.22% bandwidth at 1.97 GHz with an isolation of greater than 22 dB, having a very small device size of 0.021 mm^2 . The predicted results are in close agreement with measurement results, validating the developed BAW filter design method, applicable for the design of both piezoelectric and ferroelectric ladder-type filters.

5.2. Future Direction

5.2.1. BST Growth Condition Characterization and Optimization using RF Magnetron Sputtering

The work presented in this dissertation has focused on the design and modeling aspects of intrinsically switchable BST FBARs and FBAR filters, which are categorized into the area of devices and circuits. In order to improve device quality factors, it is indispensable to perform fundamental *material studies* including BST growth condition

characterization and optimization. In the past years, the research group has been investigating the dependence of microwave characteristics of BST thin film varactors on various growth parameters in a pulsed laser deposition (PLD) system. A strong dependence between the material permittivity and tunability on the degree of crystallinity of the thin film has been observed. The degree of crystallinity may be primarily controlled by growth temperature or through post-growth annealing, as characterized through X-ray diffraction (XRD) measurements. Increasing the deposition temperature or applying a post-deposition annealing step results in an increase in crystallinity and grain size of BST, with a clear trade-off, resulting in altering the stoichiometry of the material. Consequently, altered stoichiometry (metal deficiency) was found to lead material loss tangent increase and dispersion at microwave frequencies. *Qualitatively the same results are expected for the sputtered BST films using the recently-installed RF magnetron sputtering system.*

Many different growth conditions in RF magnetron sputtering system affect the properties/quality of the BST. Deposition parameters, such as partial pressure, Ar/O₂ ratio, substrate temperature, growth rate, source to target distance, etc. can be considered. The composition of the film, which can vary due to the different atomic weights of Ba, Sr, Ti, and O, can be determined by using Rutherford backscattering spectrometry (RBS). The crystallinity of the film can be characterized by XRD. The film roughness, which determines the quality factor of resonators, can be measured using atomic force microscopy (AFM). The electrostrictive and electric-field-induced piezoelectric coefficients can be characterized using piezoresponse force microscopy (PFM). The aim of this part of the future work is to achieve higher device quality factors and electromechanical coupling

coefficients, lower TCF values, and higher breakdown voltages for low insertion-loss, temperature-stabilized, and high power-handling resonators.

5.2.2. Linearity Improvement of BST FBARs and FBAR Filters

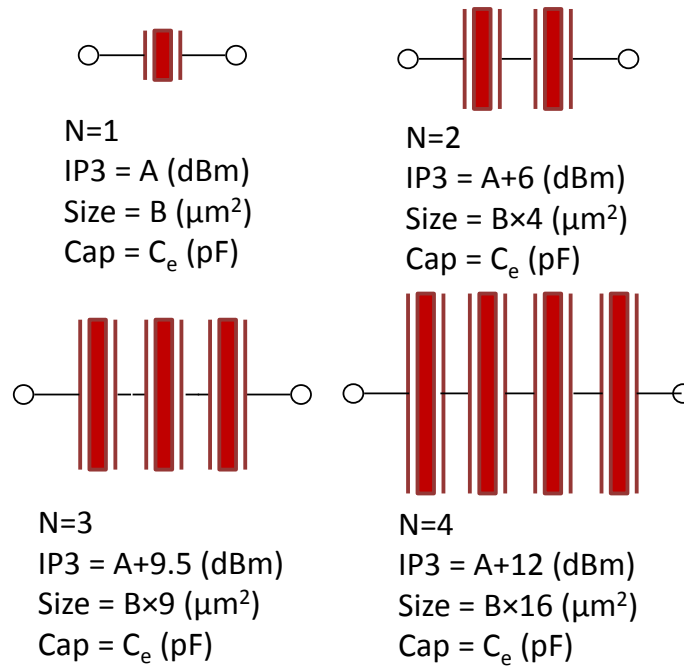


Figure 5.1: Schematics of an FBAR with different number of resonators connected in series for improved linearity.

The nonlinear circuit model for BST FBARs has been presented in this dissertation that can accurately predict both their dc and RF behavior. The model can be utilized for the prediction of the device behavior over a wide range of dc bias voltages and RF power levels and can be employed to study the linearity of BST FBAR based filters. The linearity level of a BST FBAR can be improved by cascading several series FBARs that have larger

areas compared to a single FBAR in order to maintain their overall capacitance (impedance). The idea is to reduce the level of RF voltage swing across each FBAR, leading to the improvement of entire FBAR structure. By using a series-connected FBAR structure, the third-order intercept point (IP3), which is the measure of the linearity level of nonlinear devices, is improved by $20 \cdot \log_{10} N$ (dB) where N is the number of FBARs that are connected in series as shown in Fig. 5.1.

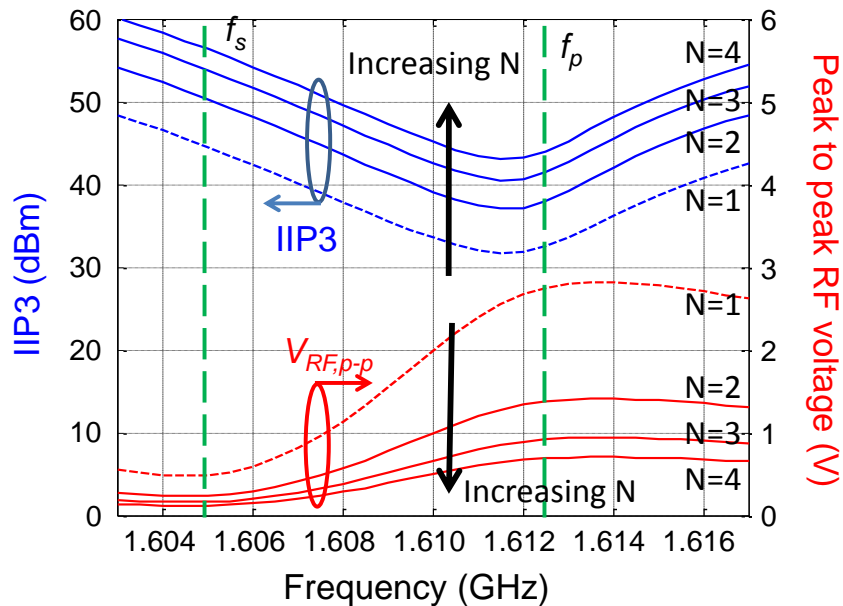


Figure 5.2: Input-referred third-order intercept point (IIP3) and peak-to-peak RF voltage swing simulation results for a BST FBAR based on the developed nonlinear model.

Based on the developed model, an FBAR with various values of N is simulated to examine the input-referred IP3 level (IIP3) and peak to peak RF voltage swing near resonator resonance frequencies (Fig. 5.2). As can be seen, the IP3 level is improved due

to the reduced RF voltage swing over the entire range of simulation frequency. Although the size of FBAR structure increases with the number of resonators (N), the increase in FBAR size is not a significant issue due to the inherent compact-size nature of BST FBARs. This high-linearity BST FBARs can be utilized for the design of high linearity BST FBAR filters. For example, a switchable BST FBAR filter with an IIP3 of 26 dBm and the area of $130 \mu\text{m} \times 100 \mu\text{m}$ in [37] can be designed to provide a higher linearity level by replacing each series/shunt resonator of the filter with series connected FBAR devices. For example, for $N=4$, FBAR filter provides an IIP3 of 38 dBm while maintaining its compact size (based on the layout, the filter size is $225 \mu\text{m} \times 475 \mu\text{m}$).

Since the effect of each resonator within the filter on the overall filter performance can be different, during the course of the future work, the effects of individual resonator linearity on the overall filter linearity can be investigated in order to develop possible approaches that allow the design of high linearity filters with minimal impact on the insertion loss and size. Furthermore, the trade-off between insertion loss, size, and linearity level of a switchable filter can be studied with respect to the number of series-connected resonators (N). In this way, the filter performance can be fully optimized according to the required filter linearity requirements.

5.2.3. Reconfigurable Filter Bank based on Switchable BST FBAR Filters

A switched BST FBAR filter bank consisting of several filters covering the required frequency bands can be designed and implemented on the same substrate. Figure 5.3 shows the schematic of a designed filter bank which utilizes two series BST varactors at the input and output of each filter together with shunt inductors at the filter bank input and output

ports. The filter highlighted in yellow is in its ON state. The OFF-state filters (shown in by the dashed box) together with shunt inductors exhibit a parallel resonance response, thereby exhibiting an open-circuit response, hence preventing RF signal from being transmitted through the OFF-state filters. BST varactors in series with OFF state filters are set to their minimum value (non-zero bias voltage, i.e. only varactors are biased).

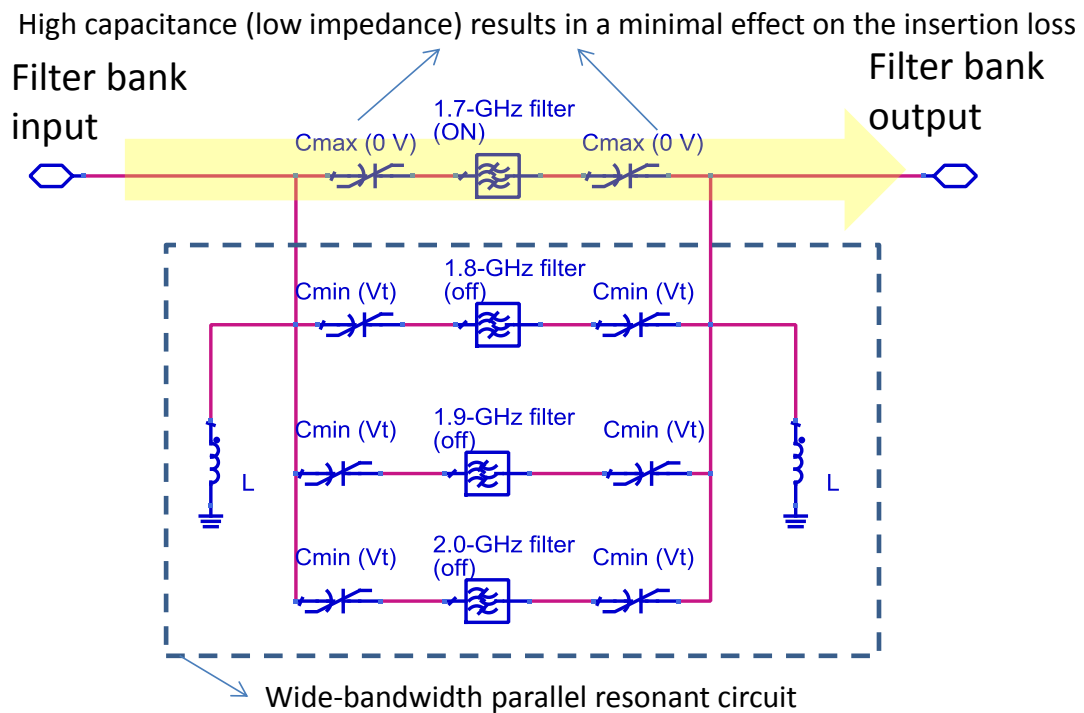


Figure 5.3: Proposed switched BST filter bank circuit diagram consisting of four filters with series connected BST varactors.

BST varactors connected to the ON-state filter, are set to their maximum value (zero biased), providing their highest capacitance value. The higher the tunability of BST

capacitance, the better performance of filter bank. BST varactor tunabilities achieved are within 3:1 to 5:1 range [36], however higher than 10:1 tunabilities have also been demonstrated [8]. The implementation of series BST varactors within the filter bank does not add to the required processing steps. BST varactors fabrication require the same processing steps as the BST FBARs except that the substrate beneath the BST varactors is not removed using etching process.

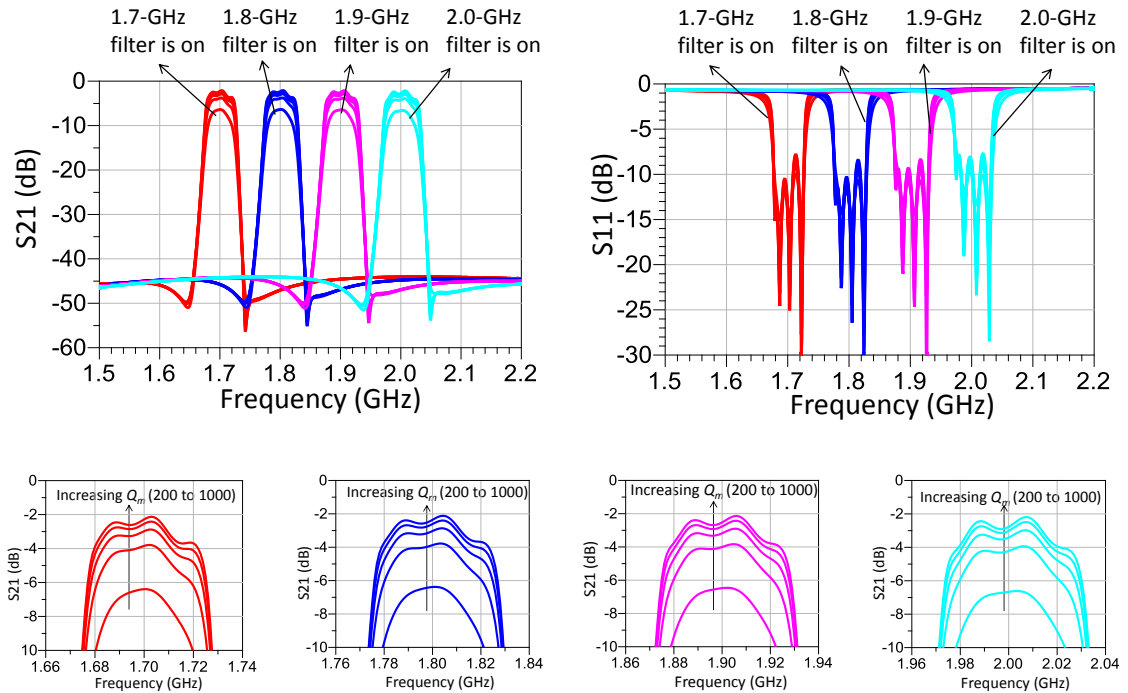


Figure 5.4: Simulation results for the proposed switched filter bank consisting of four 2.5-stage filters with matching networks comprising two shunt inductors as well as eight BST varactors.

Figure 5.4 shows the simulation results for a switched filter bank using the proposed circuit topology consisting of four 2.5-stage filters. A stand-alone FBAR filter is designed based on the image parameter method, which is first introduced in this work (Chapter 4.3). Each filter's center frequency is set to 1.7, 1.8, 1.9 and 2.0 GHz all having 3% fractional bandwidth. A modest capacitance tunability of 4:1 for BST varactors ($Q_{\text{var}}=100$) is assumed and the value of shunt inductance is set to 3.5 nH ($Q_{\text{ind}}=50$) such that the center frequency of a parallel resonance circuit is at 1.85 GHz.

The performance of the filter bank is similar to a single filter response, indicating the effectiveness of the proposed filter bank design approach. It is noted that the proposed filter bank can be implemented on a single substrate. Each filter center frequency is adjusted simply by a mass-loading layer deposited on top of electrodes for each of FBARs. A required mass-loading (platinum) layer thickness is less than approximately 210 nm for 300-MHz frequency down shift. Therefore, the entire filter is fabricated through one growth process using the same BST film thickness. The next step of this future work is to implement this fully-integrated filter bank.

5.3. Publications

Based on the work in this dissertation, the following peer-reviewed journal and conference publications have been published. Some work are currently under review or to be submitted for publication.

5.3.1. Journal publications

1. **S. Lee** and A. Mortazawi, "An intrinsically switchable ladder-type ferroelectric BST-

- on-Si composite FBAR filter,” *IEEE Trans. Ultrasonics, Ferroelectrics, and Frequency Control (TUFFC)*, vol. 63, no. 3, pp. 456-462, Mar. 2016.
2. S.A. Sis, **S. Lee**, V. Lee, and A. Mortazawi, “An intrinsically switchable, monolithic BAW filter using ferroelectric BST,” *IEEE Microwave and Wireless Components Letters (MWCL)*, vol. 26, no. 1, pp. 25-27, Jan. 2016.
 3. S.A. Sis, **S. Lee**, V. Lee, A. Bayraktaroglu, J. Philips, and A. Mortazawi, "Intrinsically switchable, high- Q ferroelectric-on-silicon composite film bulk acoustic resonators,” *IEEE Trans. Ultrasonics, Ferroelectrics, and Frequency Control (TUFFC)*, vol. 61, no. 2, pp. 231-238, Feb. 2014.
 4. **S. Lee**, V. Lee, S.A. Sis, and A. Mortazawi, "Large-signal performance and modeling of intrinsically switchable ferroelectric FBARs,” *IEEE Trans. Microwave Theory and Techniques (TMTT)*, vol. 61, no. 1, pp. 415-422, Jan. 2013.

5.3.2. Conference publications

1. M. Zolfagharloo Koochi, **S. Lee**, and A. Mortazawi, "Design of BST-on-Si composite FBARs for switchable BAW filter application," in *2016 European Microwave Conference (EuMC)*, London, UK, to be presented in Oct. 2016.
2. **S. Lee** and A. Mortazawi, “BAW filter design method based on intrinsically switchable ferroelectric BST FBARs," in *2016 IEEE MTT-S International Microwave Symposium (IMS) Dig.*, San Francisco, CA, to be presented in May 2016.
3. **S. Lee**, M. Zolfagharloo Koochi, and A. Mortazawi, “Lateral-wave spurious-modes elimination in switchable ferroelectric BST-on-Si composite FBARs," in *2016 IEEE MTT-S International Microwave Symposium (IMS) Dig.*, San Francisco, CA, to be

- presented in May 2016.
4. M. Zolfagharloo Koochi, **S. Lee**, V. Lee, S.A. Sis, and A. Mortazawi, "Un-cooled Resonant IR Detectors Based on Barium Strontium Titanate Switchable FBARs," in *2015 European Microwave Conference (EuMC)*, Paris, France, pp. 948-951, September 2015.
 5. **S. Lee**, M. Zolfagharloo Koochi, V. Lee, S.A. Sis, and A. Mortazawi, "Temperature dependent characteristics of intrinsically switchable ferroelectric composite FBARs," in *2015 IEEE MTT-S International Microwave Symposium (IMS) Dig.*, Phoenix, AZ, pp. 1-4, May 2015.
 6. V. Lee, **S. Lee**, S.A. Sis, and A. Mortazawi, "Switching reliability and switching speed of barium strontium titanate (BST) BAW devices," in *2014 European Microwave Conference (EuMC)*, Rome, Italy, pp. 500-503, October 2014.
 7. **S. Lee**, V. Lee, S.A. Sis, and A. Mortazawi, "Physics-based large-signal modeling of intrinsically tunable and switchable ferroelectric FBARs," in *2014 IEEE MTT-S International Microwave Symposium (IMS) Dig.*, Tampa, FL, pp. 1–4, June 2014.
 8. V. Lee, **S. Lee**, S.A. Sis, and A. Mortazawi, "Switchable dual-frequency barium strontium titanate film bulk acoustic resonators," in *2014 IEEE MTT-S International Microwave Symposium (IMS) Dig.*, Tampa, FL, pp. 1–4, June 2014.
 9. **S. Lee**, V. Lee, S.A. Sis, and A. Mortazawi, "A simple nonlinear mBVD model parameter extraction method for intrinsically switchable ferroelectric FBARs," in *2013 European Microwave Conference (EuMC)*, Nuremberg, Germany, pp. 1355-1358, October 2013.
 10. V. Lee, S.A. Sis, **S. Lee**, X. Zhu, and A. Mortazawi, "Lateral mode intrinsically

- switchable barium titanate film bulk acoustic wave resonators," in *2013 European Microwave Conference (EuMC)*, Nuremberg, Germany, pp. 1347-1350, October 2013.
11. **S. Lee**, V. Lee, S.A. Sis, and A. Mortazawi, "Linearity analysis of intrinsically switchable ferroelectric FBAR filters," in *2013 IEEE MTT-S International Microwave Symposium (IMS) Dig.*, Seattle, WA, pp. 1–4, June 2013.
 12. V. Lee, **S. Lee**, S.A. Sis, and A. Mortazawi, "Switching reliability of tunable ferroelectric resonators and filters," in *2013 IEEE MTT-S International Microwave Symposium (IMS) Dig.*, Seattle, WA, pp. 1–4, June 2013.
 13. V. Lee, S.A. Sis, **S. Lee**, and A. Mortazawi, "Intrinsically switchable ferroelectric bulk acoustic wave filters based on barium strontium titanate thin films," in *2013 IEEE MTT-S International Wireless Symposium (IWS) Dig.*, Beijing, China, pp. 1–4, April 2013.
 14. S.A. Sis, V. Lee, **S. Lee**, and A. Mortazawi, "Intrinsically switchable thin film ferroelectric resonators utilizing electric field induced piezoelectric effect," in *2013 IEEE MTT-S International Wireless Symposium (IWS) Dig.*, Beijing, China, pp. 1–4, April 2013.
 15. **S. Lee**, V. Lee, S.A. Sis, and A. Mortazawi, "Large signal modeling of switchable ferroelectric FBARs," in *2012 European Microwave Integrated Circuits Conference (EuMIC)*, Amsterdam, Netherlands, pp. 24-27, October 2012.
 16. V. Lee, **S. Lee**, S.A. Sis, and A. Mortazawi, "Large signal performance of ferroelectric FBARs." in *2012 IEEE MTT-S International Microwave Symposium (IMS) Dig.*, Montreal, QC, pp. 1–3, June 2012.

5.3.3. Under Review or In-Preparation

1. **S. Lee** and A. Mortazawi, “A synthesis method for ladder-type bulk acoustic wave filters based on image parameter method,” *IEEE Trans. Microwave Theory and Techniques (TMTT)*, to be submitted for the special issue of IMS 2016 (in preparation).
2. V. Lee, **S. Lee**, S.A. Sis, and A. Mortazawi, “Intrinsically switchable, frequency reconfigurable, barium strontium titanate resonators and filters,” *IEEE Trans. Microwave Theory and Techniques (TMTT)*, submitted for publication (under review).

APPENDICES

Appendix A

Relationship between Device and Circuit Parameters

From the second order Taylor approximation [57], electromechanical coupling coefficient can be expressed as a quadratic function in terms of the series or parallel resonance frequency as shown below

$$\begin{aligned}
 K_t^2 &= \frac{\pi^2}{4} \left(\frac{f_s}{f_p} \right) \left(\frac{f_p - f_s}{f_p} \right) \\
 \Rightarrow \frac{4K_t^2}{\pi^2} &= \frac{f_s f_p - f_s^2}{f_p^2} \\
 \Rightarrow 4K_t^2 f_p^2 - f_s f_p \pi^2 + f_s^2 \pi^2 &= 0 \\
 \Rightarrow f_s^2 - f_p f_s + \frac{4K_t^2 f_p^2}{\pi^2} &= 0 \\
 \Rightarrow f_s &= \frac{f_p \pm \sqrt{f_p^2 - \frac{16K_t^2}{\pi^2} f_p^2}}{2} \\
 \Rightarrow f_s &= \frac{f_p}{2} \left(1 \pm \sqrt{1 - \frac{16K_t^2}{\pi^2}} \right) \\
 \Rightarrow f_s &= \frac{f_p}{2} \left(1 + \sqrt{1 - \frac{16K_t^2}{\pi^2}} \right) \quad (\because f_p < 2f_s \text{ for general FBARs})
 \end{aligned} \tag{A.1}$$

Therefore, f_s or f_p can be expressed as shown below

$$\begin{aligned}
f_s &= \frac{f_p}{2} \times \left(1 + \sqrt{1 - \frac{16K_t^2}{\pi^2}} \right) \\
f_p &= 2f_s \div \left(1 + \sqrt{1 - \frac{16K_t^2}{\pi^2}} \right)
\end{aligned} \tag{A.2}$$

Furthermore, f_s and f_p can be expressed as a function of mBVD model parameters (L_m , C_m , and C_e):

$$\begin{aligned}
f_s &= \frac{1}{2\pi\sqrt{L_m C_m}} \\
f_p &= \frac{1}{2\pi\sqrt{L_m C_m}} \sqrt{1 + \frac{C_m}{C_e}}
\end{aligned} \tag{A.3}$$

These conditions lead to the following relationship between motional and static/electrical capacitances used throughout this dissertation.

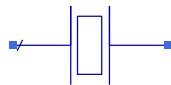
$$\begin{aligned}
\frac{f_p}{f_s} &= \frac{2}{\left(1 + \sqrt{1 - \frac{16K_t^2}{\pi^2}} \right)} = \sqrt{1 + \frac{C_m}{C_e}} \\
\Rightarrow \frac{C_m}{C_e} &= \frac{4}{\left(1 + \sqrt{1 - \frac{16K_t^2}{\pi^2}} \right)^2} - 1
\end{aligned} \tag{A.4}$$

It should be noted that (A.4) is an analytic function that can be easily analyzed while maintaining its accuracy. The error associated with the approximation used is less than 0.16% with K_t^2 of 10%. Therefore (A.4) can be used as a standard like 2nd order Taylor approximation for K_t^2 is regarded as a standard expression [57].

Appendix B

ADS Circuit Models

B1: mBVD model implementation in ADS using device parameters including f_s and f_p (useful for the simulation based on measurements)



Model_FBAR_linear_fs_fp

X4

$f_s=2$ GHz

$f_p=2.06$ GHz

$C_e=2$ pF

$Q_m=1000$

$Q_e=200$

$R_s=1$ Ohm

Var
Eqn

VAR

VAR3

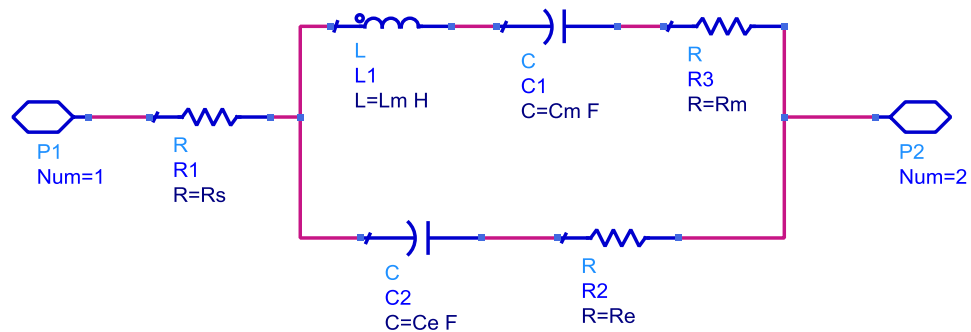
$C_m=C_e*((f_p/f_s)*(f_p/f_s)-1)$

$\omega_s=2*\pi*f_s$

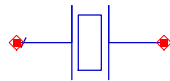
$L_m=1/C_m/\omega_s/\omega_s$

$R_m=\omega_s*L_m/Q_m$

$R_e=1/(2*\pi*f_p*C_e*Q_e)$



B2: mBVD model implementation in ADS using device parameters including f_s and K_t^2 (useful for the simulation of a series resonator in a filter)



Model_FBAR_linear_fs_Kt2

X3

fs=2 GHz

Kt2_percent=7

Ce=2 pF

Qm=1000

Qe=200

Rs=1 Ohm

Var Eqn

VAR

VAR2

Kt2=if (Kt2_percent == 0) then 0 else Kt2_percent/100 endif

ws=2*pi*fs

fp=2*fs/(1+sqrt(1-16*Kt2/pi/pi))

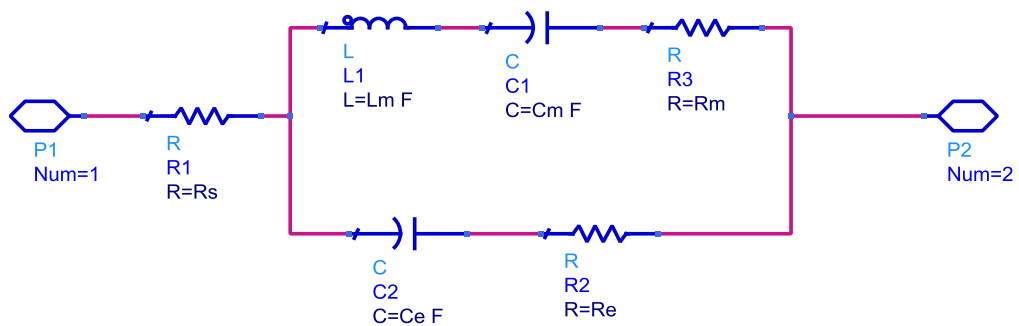
wp=2*pi*fp

Cm=if Kt2==0 then 1 else Ce*((fp/fs)*(fp/fs)-1) endif

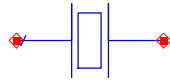
Lm=if Kt2==0 then 1 else 1/Cm/ws/ws endif

Rm=if Kt2==0 then 1e10 else ws*Lm/Qm endif

Re=1/(wp*Ce*Qe)



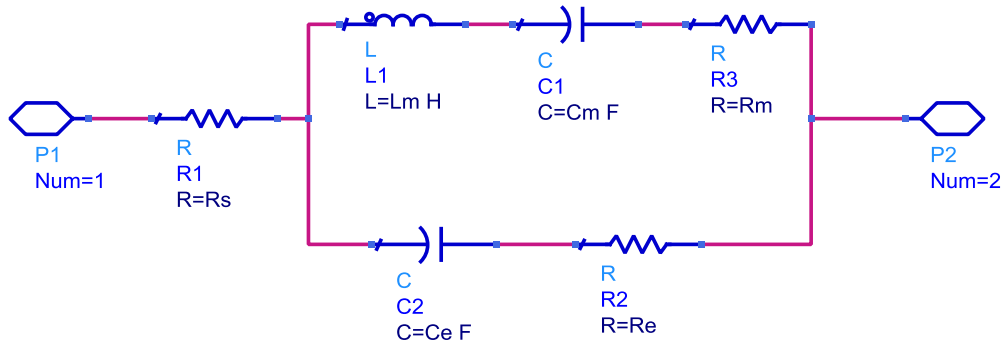
B3: mBVD model implementation in ADS using device parameters including f_p and K_t^2 (useful for the simulation of a shunt resonator in a filter)



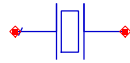
Model_FBAR_linear_fp_Kt2
 X2
 fp=2 GHz
 Kt2_percent=7
 Ce=2 pF
 Qm=1000
 Qe=200
 Rs=1 Ohm

```

Var
Eqn
VAR
VAR2
Kt2=if (Kt2_percent == 0) then 0 else Kt2_percent/100 endif
wp=2*pi*fp
fs=fp*(1+sqrt(1-16*Kt2/pi/pi))/2
ws=2*pi*fs
Cm=if Kt2==0 then 1 else Ce*((fp/fs)*(fp/fs)-1) endif
Lm=if Kt2==0 then 1 else 1/Cm/ws/ws endif
Rm=if Kt2==0 then 1e10 else ws*Lm/Qm endif
Re=1/(wp*Ce*Qe)
  
```

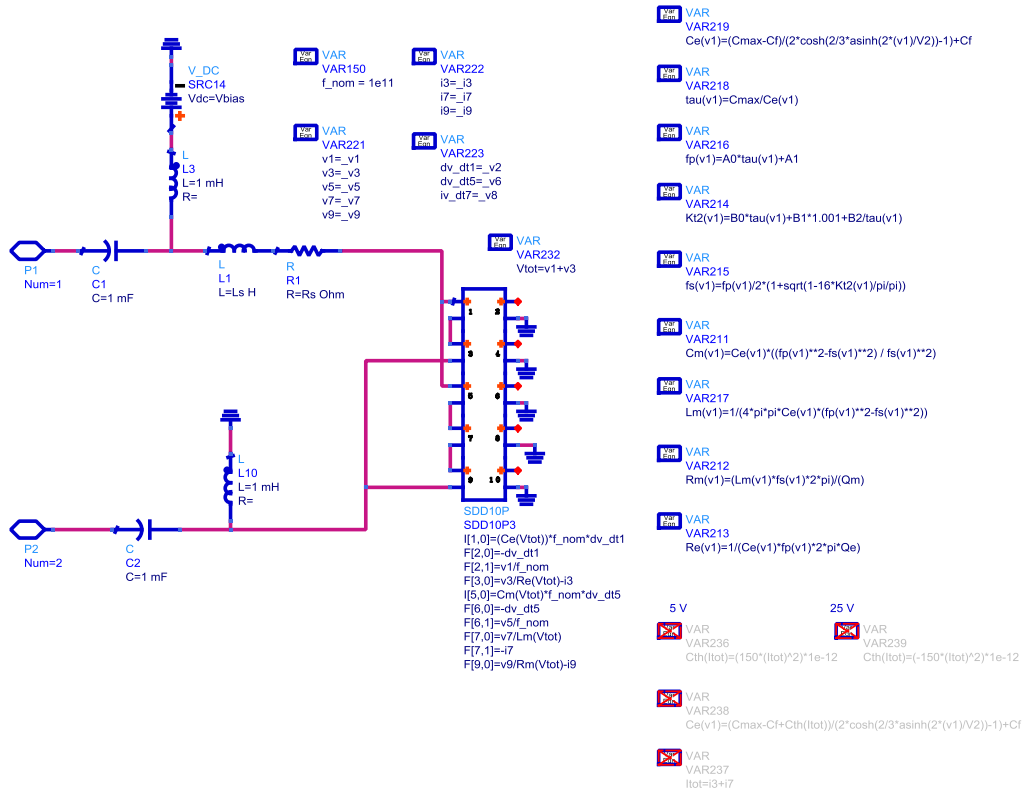


B4: nonlinear mBVD model implementation in ADS using BST FBAR nonlinear parameters (useful for the nonlinear simulation)



Nonlinear_model_for_BST_173_2xlast

X3
 Cmax=5.84 pF
 Cf=0.39 pF
 V2=6.45 V
 A0=-8.9416e6
 A1=2.0805e9
 B0=-5.0918e-3
 B1=1.509e-1
 Qm=115
 Qe=30
 Ls=0.04 nH
 Rs=1.6 Ohm



Appendix C

Matlab Code for Nonlinear Model Parameter Extraction and 1-D

Acoustic Transmission Line Model Simulation

C.1: Matlab code for nonlinear model parameter extraction

```
clear all; close all; clc;
```

```
%% Measurement results: Vdc, Ce, fs, fp, Kt2, real(Yin), real(Zin)
```

```
Measurement=[
```

```
0 5.84 2.0752 2.0752 0 0 0
1 5.494 2.0684 2.0747 0.75 0.0421 8.9329
2 4.959 2.057 2.0715 1.72 0.0914 24.7622
3 4.446 2.0428 2.0693 3.12 0.129 42.0515
4 3.995 2.0312 2.067 4.2 0.1542 59.5706
5 3.607 2.0212 2.0649 5.11 0.1662 76.3029
6 3.291 2.0125 2.0632 5.92 0.1713 91.376
7 3.026 2.0054 2.0615 6.54 0.1736 104.9909
8 2.796 1.9999 2.0606 7.06 0.1719 117.238
9 2.605 1.9941 2.0593 7.57 0.1699 128.4226
10 2.44 1.9904 2.0572 7.76 0.1658 138.7074
11 2.298 1.9855 2.057 8.29 0.161 148.0888
12 2.173 1.9823 2.0552 8.45 0.1571 157.4274
13 2.065 1.98 2.0539 8.57 0.1536 165.9948
14 1.968 1.9765 2.0525 8.81 0.1492 174.3758
15 1.882 1.9755 2.0516 8.82 0.1453 182.3265
16 1.806 1.9732 2.0516 9.08 0.1424 189.654
17 1.735 1.9714 2.0494 9.04 0.1383 195.9845
18 1.673 1.9705 2.0489 9.09 0.1349 203.1047
19 1.617 1.9684 2.048 9.23 0.1308 209.4845
20 1.564 1.9682 2.0476 9.21 0.1279 215.0943
21 1.515 1.9668 2.0463 9.23 0.1246 220.9366
22 1.472 1.9655 2.0462 9.36 0.1219 226.8344
23 1.43 1.9646 2.0462 9.46 0.1187 231.3644
24 1.393 1.9636 2.0448 9.42 0.1161 236.3335
25 1.356 1.9625 2.0439 9.45 0.113 240.9363
```

```
]; % Rs=1.6 ohm, Ls=0.04 nH, Ra=500 ohm de-embedded
```

```
Measurement=transpose(Measurement);
```

```

V_meas=Measurement(1,:);
Ce_meas=(Measurement(2,:))*1e-12; % unit is F
fs_meas=Measurement(3,:)*1e9; % unit is Hz
fp_meas=Measurement(4,:)*1e9; % unit is Hz
Kt2_meas=Measurement(5,+)/100; % unitless, not %
Real_Yin_meas=Measurement(6,); % unit is mho
Real_Zin_meas=Measurement(7,); % unit is ohm
tau_meas=max(Ce_meas)./Ce_meas;

%% dc bias voltage
V=-30:0.1:30;
Rs=1.6;

%% Ce model parameters
Cmax=max(Ce_meas);
fun_Ce = @(p1) sum((Ce_meas - ((Cmax-
p1(1))./(2*cosh(2/3*asinh(2*V_meas/p1(2))))-1)+p1(1))).^2);
pguess = [0,50];
[p1,fminres] = fminsearch(fun_Ce,pguess);

Ce_theo= (Cmax-p1(1))./(2*cosh(2/3*asinh(2*V/p1(2))))-1)+p1(1);
tau_theo=Cmax./Ce_theo;

figure(1)
plot(V_meas,Ce_meas*1e12,'ro','linewidth',2);hold on;
plot(V,Ce_theo*1e12,'r','linewidth',2);
ylabel('Ce (pF)','fontsize',15)
xlabel('dc bias voltage (V)','fontsize',15)
set(gca,'YGrid','on','fontsize',15);

%% fp model parameters
fun_fp = @(p2) sum( ( - fp_meas + p2(1)*tau_meas + p2(2) ).^2 );
pguess2 = [-1e7 1e7 1e7];
[p2,fminres2] = fminsearch(fun_fp,pguess2);

fp_theo= p2(1)*tau_theo + p2(2) ;

figure(2)
plot(V_meas,fp_meas/1e9,'ro','linewidth',2);hold on
plot(V,fp_theo/1e9,'r','linewidth',2)
ylabel('fp (GHz)','fontsize',15);
xlabel('dc bias voltage (V)','fontsize',15);
set(gca,'YGrid','on','fontsize',15);

%% Kt2 model parameters

```

```

weighting=1;
fun_Kt2 = @(p3) sum( ( - Kt2_meas + p3(1)*tau_meas + p3(2) +
p3(3)./tau_meas ).^2 ...
+ ( - Kt2_meas(1) + p3(1)*tau_meas(1) + p3(2) + p3(3)./tau_meas(1) ).^2
*weighting );
pguess3 = [1 1 1];
[p3,fminres3] = fminsearch(fun_Kt2,pguess3);

```

```

Kt2_theo= p3(1)*tau_theo + p3(2) + p3(3)./tau_theo;

```

```

figure(3)
plot(V_meas,Kt2_meas*100,'ro','linewidth',2);hold on
plot(V,Kt2_theo*100,'r','linewidth',2);
ylabel('Kt2,eff (%)','fontsize',15);
xlabel('dc bias voltage (V)','fontsize',15);
set(gca,'YGrid','on','fontsize',15);
%% fs model parameters
fs_theo= fp_theo/2 .* (1+ (1 - 16*Kt2_theo/pi/pi).^0.5);

```

```

figure(4)
plot(V_meas,fs_meas/1e9,'ro','linewidth',2);hold on
plot(V,fs_theo/1e9,'r','linewidth',2);
ylabel('fs (GHz)','fontsize',15);
xlabel('dc bias voltage (V)','fontsize',15);
set(gca,'YGrid','on','fontsize',15);

```

```

figure(5)
plot(V_meas,fp_meas/1e9,'ro','linewidth',2);hold on
plot(V,fs_theo/1e9,'r','linewidth',2);
plot(V_meas,fs_meas/1e9,'b*','linewidth',2);
legend('fp','fs')
plot(V,fp_theo/1e9,'r','linewidth',2);
ylabel('fs and fp (GHz)','fontsize',15);
xlabel('dc bias voltage (V)','fontsize',15);
set(gca,'YGrid','on','fontsize',15);

```

```

%% Cm and Lm
Cm_meas=Ce_meas.*( (fp_meas./fs_meas).^2 -1 );
Lm_meas=1./(Cm_meas .* (2*pi*fs_meas).^2);
Cm_theo=Ce_theo.*( (fp_theo./fs_theo).^2 -1 );
Lm_theo=1./(Cm_theo .* (2*pi*fs_theo).^2);

```

```

%% Qm model parameters
fun_Qm = @(p4) sum( ( - Real_Yin_meas +
1./(2*pi*fs_meas.*Lm_meas./p4(1)) ).^2 );

```

```
pguess4 = [100];
[p4,fminres4] = fminsearch(fun_Qm,pguess4);
```

```
Real_Yin_theo= 1./(2*pi*fs_theo.*Lm_theo./p4(1));
```

```
figure(6)
plot(V_meas,Real_Yin_meas,'ro','linewidth',2);hold on
plot(V,Real_Yin_theo,'r','linewidth',2);
ylabel('Real part of Yin (mho)','fontsize',15);
xlabel('dc bias voltage (V)','fontsize',15);
set(gca,'YGrid','on','fontsize',15);
```

```
Rm_meas=2*pi*fs_meas.*Lm_meas/p4;
Rm_theo=2*pi*fs_theo.*Lm_theo/p4;
```

```
%% Qe model parameters
```

```
fun_Qe = @(p5) sum( ( - Real_Zin_meas + 1./(((2*pi*fp_meas.*Ce_meas).^2) ...
    .*(Rm_meas+1./((2*pi*fp_meas.*Ce_meas).*p5(1)))) ).^2 );
pguess5 = [100];
[p5,fminres5] = fminsearch(fun_Qe,pguess5);
```

```
Real_Zin_theo=
1./(((2*pi*fp_theo.*Ce_theo).^2).*(Rm_theo+1./((2*pi*fp_theo.*Ce_theo).*p5(1))));
```

```
figure(7)
plot(V_meas,Real_Zin_meas,'ro','linewidth',2);hold on
plot(V,Real_Zin_theo,'r','linewidth',2);
ylabel('Real part of Zin (ohm)','fontsize',15);
xlabel('dc bias voltage (V)','fontsize',15);
set(gca,'YGrid','on','fontsize',15);
```

```
Re_meas=2*pi*fp_meas.*Ce_meas/p5;
Re_theo=2*pi*fp_theo.*Ce_theo/p5;
```

```
%% model parameters
```

```
C_max = Cmax
Cf_in_pF =p1(1)*1e12
V2_in_V = p1(2)
A0 = p2(1)
A1 = p2(2)
B0 = p3(1)
B1 = p3(2)
B2 = p3(3)
Q_m = p4
Q_e = p5
```

C.2: Matlab code for a 1-D acoustic transmission line model simulation

```
clear all; close all; clc;

Z0=50; % system impedance
Y0=1/Z0; % system admittance

%% Constants from Laust Peterson's file
% Velocity of longitudinal acoustic wave (m/s)
v_pt = 3236.1; %% modified from 3300
v_bst = 6307.3; %% modified from 5600
v_sio2 = 5848.1; %% modified from 5100
v_si = 8445.6; %% modified from 8100
v_au = 2800;
v_air = 360;
% v_au= 6300 ; % for aluminum simulation

% Acoustic impedance (kg/m^2s)
Z_pt = 69.4153e6; %% modified from 69.8e6 69.4153
Z_bst = 35.3206e6; %% modified from 33e6
Z_sio2 = 12.8657e6; %% modified from 12.5e6
Z_si = 19.68e6; %% modified from 19.5e6
Z_au = 63.8e6;
Z_air = 400;
% Z_au = 17e6; % for aluminun simulation

% Acoustic quality factor
Q_pt = 260; Q_au = 200; Q_si = 2000; Q_sio2 = 1000;
Q_bst = 500; Q_sto = 9500; Q_aln = 9500;
Q_sapphire = 9500; Q_ti = 100;
Q_al = 500;

%% Handling Figures

fmin=0.0001e9; % frequency range of plot
fmax=4e9;
fstep=0.1e6;

w0=2*pi*1.2e9;

color_a=[1 0 0]; color_b=[0 0 1];
color_c=[1 0 0]; color_d=[0 0 1];
```

```

f=(fmin:fstep:fmax);w=2*pi*f;fqmin=fmin;fqmax=fmax;
fxsize= 500;fysize= 422;fxoffset=900;fyoffset=572;
ttt1=20;

%% Material Thickness
t_pt_t = 100e-9; % top electrode
t_bst = 930e-9; %% this is a variable (initial parameter)
t_pt_b = 100e-9; % bottom electrode (preplatinized)
t_sio2 = 200e-9; % diffusion barrier layer
t_si = 4000e-9; %% this is a variable (initial parameter)

%% BST property
Area = (1600)*(10^-12); % Device Area (10^-12=um^2)
ER_bst_on = 130; % Relative permittivity when biased 20 V with 600-nm BST
thickness
ER_bst_off= 300; % Relative permittivity when biased 0 V with 600-nm BST thickness
K2= 0.06; % Estimated electromechanical coupling coefficient of BST

%% Other loss terms (Rpar: dielectric loss, Rser: ohmic loss, Lser: parasitic inductance)
Rpar=500000000000;
Rser=0;
Lser=0.055e-39;

% Electrical capacitance
E0=8.854e-12; %% permittivity of air
Ce_on = (E0*ER_bst_on*Area/t_bst);
Ce_off = (E0*ER_bst_off*Area/t_bst);

%% Acoustic impedance seen at top electrode looking into TOP direction

%Structure of the device: Air-Pt_t- BST -Pt_b-SiO2-Si-Air
%Calculation of impedances: Ztop (Air/Pt_t) --> Zin <-- Zbottom (Pt_b/SiO2/Si/Air)

%% Propagation constant and Phase delay in BST
% Platinum (Pt)
beta_pt = 2*pi.*f/v_pt;
alpha_pt = beta_pt/2/Q_pt;
gamma_pt = alpha_pt + j.*beta_pt;
% Silicon (Si)
beta_si = 2*pi.*f/v_si;
alpha_si = beta_si/2/Q_si;
gamma_si = alpha_si + j.*beta_si;
% Silicon Oxide (SiO2)
beta_sio2 = 2*pi.*f/v_sio2;
alpha_sio2 = beta_sio2/2/Q_sio2;

```

```

gamma_sio2 = alpha_sio2 + j.*beta_sio2;
% Transduction layer (BST)
beta_bst = 2.*pi.*f./v_bst;
alpha_bst = beta_bst./2./Q_bst;
gamma_bst = alpha_bst + j.*beta_bst;
% The half of the phase delay in BST
phi_bst = -j.*gamma_bst.*t_bst/2;

%% Acoustic impedance
% The impedance seen at top Pt layer looking into top direction
Ztop1 = Z_pt.*(Z_air + Z_pt.*tanh(gamma_pt.*t_pt_t))...
        ./(Z_pt + Z_air.*tanh(gamma_pt.*t_pt_t));

% The impedance seen at Si layer looking into bottom direction
Zbot1 = Z_si.*(Z_air + Z_si.*tanh(gamma_si.*t_si))...
        ./(Z_si + Z_air.*tanh(gamma_si.*t_si));
% The impedance seen at SiO2 layer looking into bottom direction
Zbot2 = Z_sio2.*(Zbot1 + Z_sio2.*tanh(gamma_sio2.*t_sio2))...
        ./(Z_sio2 + Zbot1.*tanh(gamma_sio2.*t_sio2));
% The impedance seen through BOTTOM electrode
Zbot3 = Z_pt.*(Zbot2 + Z_pt.*tanh(gamma_pt.*t_pt_b))...
        ./(Z_pt + Zbot2.*tanh(gamma_pt.*t_pt_b));

        Ztop=Ztop1;
        Zbot=Zbot3;

% The normalized top and bottom impedances
zt = Ztop./Z_bst;
zb = Zbot./Z_bst;

% FBAR impedance
Zelec = 1./(j*w*Ce_on).*...
        (1 - K2.*tan(phi_bst)./phi_bst...
        .* ((zt+zb).*cos(phi_bst).^2 + j.*sin(2.*phi_bst))...
        ./ ((zt+zb).*cos(2.*phi_bst) + j.*(zt.*zb+1).*sin(2.*phi_bst)) );
Zin_on=Zelec;
% Zin_on=Zelec.*Rpar./(Zelec+Rpar)+ Rser + j*w*Lser;
Zin_off = 1./(j*w*Ce_off + 1/Rpar)+Rser+j*w*Lser;
% quality factor calculation
Q=abs(f./2.*gradient(angle(Zin_on))./gradient(f));

[pks1 locs1]=findpeaks(real(1./Zin_on));
[pks2 locs2]=findpeaks(real(Zin_on));

```

```

% t_si=2040e-9;

mode_num=3;
t_si=(3200:25:4600)*1e-9;
target_fs=20000;

for kkk=1:length(t_si);

    Zbot1 = Z_si.*(Z_air + Z_si.*tanh(gamma_si.*t_si(kkk)))...
        ./(Z_si + Z_air.*tanh(gamma_si.*t_si(kkk)));
    Zbot2 = Z_sio2.*(Zbot1 + Z_sio2.*tanh(gamma_sio2.*t_sio2))...
        ./(Z_sio2 + Zbot1.*tanh(gamma_sio2.*t_sio2));
    Zbot3 = Z_pt.*(Zbot2 + Z_pt.*tanh(gamma_pt.*t_pt_b))...
        ./(Z_pt + Zbot2.*tanh(gamma_pt.*t_pt_b));
    Zbot=Zbot3;

    zb = Zbot./Z_bst;

    phi_bst = -j.*gamma_bst.*t_bst/2;

    Zelec = 1./(j*w*Ce_on).*...
        (1 - K2.*tan(phi_bst)./phi_bst...
        .* ((zt+zb).*cos(phi_bst).^2 + j.*sin(2.*phi_bst))...
        ./ ((zt+zb).*cos(2.*phi_bst) + j.*(zt.*zb+1).*sin(2.*phi_bst)) );
    Zin_on=Zelec.*Rpar./(Zelec+Rpar)+ Rser + j*w*Lser;

    [pks1 locs1]=findpeaks(real(1./Zin_on));
    [pks2 locs2]=findpeaks(real(Zin_on));

    while locs1(mode_num)~=target_fs

        delta_fs=abs(locs1(mode_num)-target_fs);

        if locs1(mode_num) > target_fs
            aaa1=20e-9;
            aaa2=5e-9;
            aaa3=0.9e-9;
            aaa4=0.05e-9;
        else
            aaa1=-20e-9;
            aaa2=-5e-9;
            aaa3=-0.9e-9;
            aaa4=-0.05e-9;
        end
    end
end

```

```

if delta_fs >= 1000
    t_bst=t_bst + aaa1;
else if delta_fs >= 100
    t_bst=t_bst + aaa2;
else if delta_fs >= 10
    t_bst=t_bst + aaa3;
else if delta_fs >= 1
    t_bst=t_bst + aaa4;
end
end
end
end

phi_bst = -j.*gamma_bst.*t_bst/2;

Zelec = 1./(j*w*Ce_on).*...
(1 - K2.*tan(phi_bst)./phi_bst...
.* ((zt+zb).*cos(phi_bst).^2 + j.*sin(2.*phi_bst))...
./ ((zt+zb).*cos(2.*phi_bst) + j.*(zt.*zb+1).*sin(2.*phi_bst)) );
Zin_on=Zelec.*Rpar./(Zelec+Rpar)+ Rser + j*w*Lser;

[pks1 locs1]=findpeaks(real(1./Zin_on));
[pks2 locs2]=findpeaks(real(Zin_on));

if t_bst < 40e-9
    locs1(mode_num)=target_fs;
    fprintf('\nNo solutions\n');
end
end
t_BST(kkk)=t_bst;
fs_locs(kkk)=locs1(mode_num);
fp_locs(kkk)=locs2(mode_num);
Q=(abs(f./2.*gradient(angle(Zin_on))./gradient(f)));
[pks3 locs3]=findpeaks(Q);
Q_fs(kkk)=pks3(mode_num*2);

end

Kt2_eff=pi/2*fs_locs./fp_locs.*tan(pi/2*(fp_locs-fs_locs)./fp_locs)*100
ratio=t_BST./t_si;

Everydata=transpose([ratio; Kt2_eff; Q_fs; t_BST; t_si]);

%% figures
figure (1);

```

```

semilogy(f,real(1./Zin_on),'color',color_a,'linewidth',1.5);hold on;grid on;
set(gcf,'position',[fxoffset fyoffset fxsize fysize]);
set(gca,'fontsize',15);
ylabel('Real part of Yin (mho)')
xlabel('Frequency (GHz)')
xlim([fmin fmax]);
hold off;

```

```

figure (2);
semilogy(f,real(Zin_on),'color',color_a,'linewidth',1.5);hold on;grid on;
set(gcf,'position',[fxoffset+fxsize+ttt1 fyoffset fxsize fysize]);
% title('Real part of Zin');grid on;
set(gca,'fontsize',15);
ylabel('Real part of Zin (ohm)')
xlabel('Frequency (GHz)')
% xlim([fmin fmax]);
hold off;

```

```

figure (3);
semilogy(f/1e9,abs(Zin_on),'color',color_a,'linewidth',1.5);hold on;grid on;
set(gcf,'position',[fxoffset fyoffset-fysize-95 fxsize fysize])
% title('Magnitude of Zin');grid on;
set(gca,'fontsize',15);
ylabel('Magnitude of Zin (mho)')
xlabel('Frequency (GHz)')
% xlim([fmin fmax]);
ylim([1 1000])
hold off;

```

```

figure(4)
plot(f,180*angle(Zin_on)/pi,'color',color_a,'linewidth',1.5);hold on;grid on;
set(gcf,'position',[fxoffset+fxsize+ttt1 fyoffset-fysize-95 fxsize fysize])
% title('Phase of Zin');grid on;
set(gca,'fontsize',15);
ylabel('Phase of Zin (degree)')
xlabel('Frequency (GHz)')
% xlim([fmin fmax]);
hold off;

```

```

figure(5)
plot(ratio,Kt2_eff,'linewidth',2);grid on;
set(gca,'fontsize',15,'ycolor','k')
xlabel('BST to Si thickness ratio','fontsize',15);
ylabel('Kt2,eff (%)','fontsize',15);
xlim([0.1 0.4]);

```

```
figure(6)
plot(ratio,Q_fs,'r','linewidth',2);grid on;
set(gca,'fontsize',15,'ycolor','k')
xlabel('BST to Si thickness ratio','fontsize',15);
ylabel('Quality Factor','fontsize',15);
xlim([0.1 0.4]);
```

```
figure(7)
plot(ratio,Q_fs.*Kt2_eff/100,'m','linewidth',2);grid on;
set(gca,'fontsize',15,'ycolor','k')
xlabel('BST to Si thickness ratio','fontsize',15);
ylabel('Kt2,eff X Q','fontsize',15);
xlim([0.1 0.4]);
```

```
figure(8)
plot(ratio,t_BST*1e9,'k','linewidth',2);grid on;
set(gca,'fontsize',15,'ycolor','k')
xlabel('BST to Si thickness ratio','fontsize',15);
ylabel('BST thickness (nm)','fontsize',15);
xlim([0.1 0.4]);
```

```
figure(9)
plot(ratio,t_si*1e6,'k--','linewidth',2);grid on;
set(gca,'fontsize',15,'ycolor','k')
xlabel('BST to Si thickness ratio','fontsize',15);
ylabel('Si thickness (um)','fontsize',15);
xlim([0.1 0.4]);
```

Appendix D

RF Magnetron Sputtering Standard Operating Procedures (SOP)

(M) = manual procedure

(A) = computer-controlled automatic procedure

D.1 Initialize the System

1. Make sure both water filters are “clean”
 - a. If not clean
 - i. Remove water filter (M)
 - ii. Dump liquid into drain in sputtering room (M)
 - iii. Replace with new water filter (M)
2. Open building water valves (both source (S: right) and return (R: left)) going to and from water chiller (M)
3. Make sure there is enough DI water in reservoir of water chiller (> 50%) of the gauge on the side
 - a. If there is not enough water
 - i. Remove the lid of water chiller (M)
 - ii. Add DI water from cleanroom (M)
 - iii. Replace the lid of water chiller (M)
4. Switch on water chiller (M)
5. Turn on roughing pump (M)
6. Open the valve between roughing pump and cryogenic pump (cryopump) (M)
7. Wait for “roughing pump pressure gauge” to read < 50 mTorr
8. Close the valve between roughing pump and cryopump (M)
9. Make sure main chamber is below 50 mTorr
 - a. If pressure is too high
 - i. Open the valve between roughing pump and load-lock (M)
 - ii. Open the gate valve between load-lock and main chamber (M)
 - iii. Wait until the pressure of main chamber is < 50 mTorr
 - iv. Close the gate valve between load-lock and main chamber (M)
 - v. Close the valve between roughing pump and load lock (M)
10. Turn off roughing pump (M)
11. Make sure the “cryopump temperature gauge” is on (should read below 300 K)
12. Make sure the cryopump has adequate water flow (> 0.5 gpm)
13. Turn on the cryopump compressor (M)
14. Make sure that water chiller is being properly cooled
 - a. When the compressor is running, the refrigerant head pressure should never exceed 500 psi
 - i. If this is the case, the compressor will automatically shut off

- ii. If this is the case, most likely the building water valves are not both open
 - b. The compressor should only be on for several minutes at a time and the refrigerant head pressure should not exceed 300 psi
 - c. If the compressor is running for > 3 minutes at a time, check the water filter and make sure the water chiller is properly chilling the circulating water
- 15. The temperature reading on the cryopump temperature gauge should start to decrease and after roughly 2 – 3 hours, will reach 11 K
- 16. Open valve between cryopump and main chamber
 - a. open the nitrogen gas cylinder (M), the second left one
 - i. To use computer-controlled automatic procedure, it should be open
 - b. open the gate valve between cryopump and main chamber (A, Relay 5 On)
 - c. close the nitrogen gas (M) cylinder unless you will do other processes immediately

D.2 Load Sample

1. Close valve between cryopump and main chamber (A, Relay 5 Off)
 - a. make sure the nitrogen gas cylinder is open for automatic procedure (A) above
 - b. for protecting cryopump from seeing roughing pump
2. Mount sample on sample-holder
 - a. Open load-lock door
 - i. turn on venting to load-lock (A, Relay 3 On)
 - ii. when pressure reaches >750 Torr, load-lock door will open
 - iii. make sure the thumb-screw does not seal the door shut
 - iv. turn off venting to load-lock (A, Relay 3 Off)
 - b. Take sample holder out of load-lock (M)
 - i. put on gloves
 - ii. do not touch sample holder and inside load-lock without wearing gloves
 - c. Put sample(s) on sample-holder (M)
 - i. make sure to screw it tight enough
 - d. Put sample-holder back in load-lock (M)
 - e. Close load-lock door
 - i. put off gloves
 - ii. use the thumb-screw to seal the door shut (M)
3. Rough out load-lock to < 50 mTorr
 - a. turn on roughing pump (M)
 - b. open valve between load-lock and roughing pump (M)
 - i. wait until load-lock pressure reading is < 50 mTorr
 - c. close valve between load-lock and roughing pump (M)
 - d. turn off roughing pump (M)
 - e. loosen the thumb-screw and rotate out of position (M)

4. Transfer sample from load-lock to main chamber
 - a. lower heater (M)
 - b. open the valve between load-lock and main chamber (M)
 - c. gently slide transfer arm to move sample holder over heater (M)
 - d. slowly raise heater until sample holder is resting on heater (M)
 - e. slowly rotate the heater in the unlock direction to disengage the sample holder from the loading arm (M)
 - f. move the transfer arm back into the load-lock (M)
 - g. close valve between load-lock and main chamber (M)
5. Open valve between cryopump and main chamber (A, Relay 5 On)
 - a. wait for the chamber to reach the desired base pressure (5×10^{-8} Torr)

D.3 Deposit BST

1. Prepare the following
 - a. check base pressure in main chamber is low enough
 - i. for high tunability optimized conditions $< 5 \times 10^{-8}$ Torr
 - ii. If more than 5×10^{-8} Torr, wait for it
 - b. turn on sample rotation (usually 10-20 rpm) (M)
 - c. close substrate shutter (A, Relay 4 Off)
 - i. substrate shutter is located between the sample and target
 - ii. if not working, manually control it
 - d. adjust the heater height to 0.8" mark (M)
 - i. to make sample just below substrate shutter
2. Make sure sputtering guns and substrate heater are adequately cooled
 - a. turn on secondary water pump by switching on extension cord (M)
 - b. check to see water flow is > 0.5 gpm for two (front/back) sputtering guns (M)
 - c. check to see water flow is > 0 gpm for the substrate heater (M)
3. Program temperature controller
 - a. turn on temperature controller (M)
 - b. make code pass (needs to write down in more detail)
 - c. set the current temperature to 25 °C
 - d. set the heater ramp rate (M)
 - i. 20 °C/min is relatively conservative, good for dissimilar materials
 - e. set the desired temperature (M)
 - i. 650 °C seems to be good.
 - f. Set the dwell time to non-zero value
 - g. run the program (M)
 - h. turn on current controller (M)
 - i. adjust current level (M)
 - i. adjust knob (maximum for 650 is 4.0)
 - j. check and make sure the sample is still on the sample holder when it reaches 200 °C

4. Start gas (Ar/O₂) flow when the sample reaches 200 °C (after ~15 minutes)
 - a. turn on “Power” (M, pulling and moving up)
 - b. check mass flow controller (MFCs) is 75 sccm for argon and 25 sccm for oxygen (M).
 - i. don’t need to change as it’s already set
 - c. open the argon & oxygen gas cylinder, very right & left one (M)
 - d. switch on the argon & oxygen mass flow controller (M, on position)
 - e. open the argon & oxygen valve (A, Relay 1 On & Relay 2 On)
 - f. set gate valve between main chamber and cryopump to its 3rd position (A, Relay 6 On)
5. Adjust the partial pressure to 45 mTorr.
 - a. first rotate the pressure regulator on cryopump gate valve in CCW direction (M)
 - i. pressure increases in main chamber
 - b. adjust the pressure regulator by increasing (CCW) and decreasing pressure (CW) (M)
 - i. CCW direction, cryopump shutter goes down (close), pressure increases
 - ii. CW direction, cryopump shutter goes up (open), pressure decreases
 - c. pressure changes suddenly (something like hysteresis) so needs to know the feeling
6. Turn on the sputter-gun power supply (located in bottom) and automatic matching network controllers (located in top) for both guns, when the sample reaches 300 °C
 - a. Make sure the substrate shutter is off (A, Relay 4 off)
 - b. press the power button on each unit: total of four (M)
 - c. check automatic matching network controllers are set to automatic (M)
 - d. check sputter-gun power supply for the following
 - i. ramp mode on (M)
 - ii. turn on time: 900 sec (M)
 - iii. turn off time: 900 sec (M)
 1. the power ramps up and down at 20 W/min
 - e. set the RF sputtering gun power supplies to 300 W (M)
 - f. turn on the “RF” output (M)
 - i. color changes from blue to red
7. Check and make sure the following
 - a. the plasma ignites in main chamber
 - b. the sample is still on the sample holder
 - c. the stage height is correct (1” mark)
8. Start deposition.
 - a. open the substrate shutter (A, Relay 4 On)
 - b. start your timer quickly (M)
 - i. As of 02/11/2014, deposition rate is around 400 nm / 60 min (=6.67 nm/min) with RF power of 300 W.

- c. record the load and tune values of the automatic matching network controller (M)
- 9. Stop deposition after desired deposition time,
 - a. close the substrate shutter when your timer goes off (A, Relay 4 Off)
- 10. Turn off the “RF” output of both power supplies (M)
 - a. just one click, do not click twice
 - b. should automatically ramp down
 - c. color does not change (remains in red)
- 11. Program temperature controller
 - a. set the current temperature to deposition temperature (650 °C) (M)
 - b. set the heater ramp rate to 20°C/min (M)
 - c. set the desired temperature to 25 °C (M)
 - d. run the program (M)
- 12. Turn off equipment when RF output power reaches 0 W (~15 min)
 - a. turn off the gases
 - i. close the argon & oxygen valves (A, Relay 1 Off & Relay 2 Off)
 - ii. switch off the argon & oxygen mass flow controller (M, middle position)
 - iii. close the argon & oxygen gas cylinders, very right & left one (M)
 - iv. turn off “Power” (M, moving down)
 - b. turn off the both (left/right) power supplies (M)
 - c. turn off the both (left/right) automatic matching network controllers (M)
 - d. turn off secondary water pump by switching off extension cord (M)
- 13. Open gate valve between main chamber and cryopump (A, Relay 6 Off while Relay 5 in On)
- 14. Turn off equipment when temperature is below 200 °C or 300 °C
 - a. turn off rotation (M)
 - b. turn off substrate heater power supply and current controller (M)

D.4 Unload Sample

- 1. make sure rotation is off (M)
- 2. lower substrate heater assembly (M)
- 3. rough out load-lock to < 50 mTorr
 - a. turn on roughing pump (M)
 - b. open valve between load-lock and roughing pump (M)
 - c. wait until load-lock pressure reading is < 50 mTorr
 - d. close valve between load-lock and roughing pump (M)
 - e. turn off roughing pump (M)
 - f. loosen the thumb-screw and rotate out of position (M)
- 4. transfer sample from main chamber to load-lock
 - a. open gate valve between load-lock and main chamber (M, CCW)
 - b. slide transfer arm into main chamber (M)
 - c. adjust heater height to match transfer arm (M)

- d. rotate in lock direction to attach sample holder to transfer arm (M)
- e. lower heater (M)
- f. move transfer arm back into load-lock (M)
- g. close gate valve between load-lock and main chamber (M, CW)
5. take sample out of load-lock and put sample holder back in load-lock
 - a. vent load-lock (A, Relay 3 On)
 - b. open load-lock door (M)
 - i. If pressure reaches >700 Torr, the door will open
 - ii. Make sure the thumb-screw does not seal the door shut
 - c. turn off venting (A, Relay 3 Off)
 - d. take out sample holder (M)
 - i. Put on gloves
 - ii. Do not touch inside load-lock without wearing gloves
 - e. remove sample (M)
 - f. replace sample holder (M)
 - g. close door to load-lock (M)
6. rough out load-lock to < 50 mTorr
 - a. turn on roughing pump (M)
 - b. open valve between load-lock and roughing pump (M)
 - c. wait until load-lock pressure reading is < 50 mTorr
 - d. close valve between load-lock and roughing pump (M)
 - e. turn off roughing pump (M)
 - f. loosen the thumb-screw and rotate out of position (M)
7. close the nitrogen gas cylinders (M)

D.5 Close the System

1. Turn off cryopump compressor (M)
2. Switch off water chiller (M)
3. Close the two building water valves (M)

Appendix E

Fabrication Process in Lurie Nanofabrication Facility (LNF)

E.1 Clean Wafer

Rinse in acetone for 3 min.

Rinse in isopropyl alcohol (IPA) for 3 min.

Dry using nitrogen gun

Dehydration bake at 115 °C for 5 min.

E.2 Lithography

Clean wafer

Dispense HMDS on the wafer

Spin HMDS at 4000 rpm for 30 sec.

Dispense SPR 220 3.0 on the wafer

Spin SPR 220 3.0 at 3000 rpm for 30 sec.

Soft bake at 115 °C for 90 sec.

Exposure for 6.5 to 10 sec. depending on a required PR thickness in MA/BA 6 mask/bond aligner

Post-exposure bake at 115 °C for 90 sec.

Develop using AZ726 for 1 min.

Plasma descum in YES Plasma Stripper

E.3 Bottom Electrode

Lithography

Etch Pt in Plasmatherm 790 (RIE)

Remove PR in acetone and IPA

Clean the wafer

E.4 BST Deposition using RF Magnetron Sputtering

Described in Appendix *D*

E.5 Top Electrode

Lithography

Pt evaporation in Enerjet Evaporator

Liftoff in hot acetone

Ultrasonic if required

Rinse in IPA for 3 min.

Clean the wafer

E.6 Annealing

Furnace temperature at 500 °C

Flow oxygen with 3 SCCM for 30 min.

E.7 BST Etch

Lithography

Wet etch in HF:DI (1:10) solution in Acid Bench 73

Clean wafer in Acid Bench 73

Inspect the wafer

Clean the wafer

E.8 Biasing Line

Lithography

NiCr evaporation in Cooke Evaporator

Liftoff in hot acetone

Ultrasonic if required

Rinse in IPA for 3 min.

Clean the wafer

E.9 Contact Layer

Lithography

Ti/Al/Ti/Au evaporation in Enerjet Evaporator

Liftoff in hot acetone

Ultrasonic if required

Rinse in IPA for 3 min.

Clean wafer

E.10 Mass Loading Layer

Lithography

Ti/Pt evaporation in Enerjet Evaporator

Liftoff in hot acetone

Ultrasonic if required

Rinse in IPA for 3 min.

Clean wafer

E.11 Frame Layer

Lithography

Ti/Pt evaporation in Enerjet Evaporator

Liftoff in hot acetone

Ultrasonic if required

Rinse in IPA for 3 min.

Clean wafer

E.12 Release Substrate using Deep Reactive Ion Etching (DRIE)

Backside Lithography

Plasma etch for Si using DRIE in Pegasus 4 or 6

Wet etch for SiO₂ using BHF in Acid Bench 73

BIBLIOGRAPHY

Bibliography

- [1] Qualcomm Press Release, “Qualcomm and TDK Form Joint Venture to Provide Industry-Leading RF Front-End Solutions for Mobile Devices,” San Diego, January 13, 2016, (<https://www.qualcomm.com/news/releases/2016/01/12/qualcomm-and-tdk-form-joint-venture-provide-industry-leading-rf-front-end>).
- [2] R. York, “Tunable dielectrics for RF circuits,” in Multifunctional adaptive microwave circuits and systems, M. Steer, Ed., Wiley 2008.
- [3] S. Gevorgian, *Ferroelectrics in Microwave Devices, Circuits and Systems: Physics, Modeling, Fabrication and Measurements*. New York: Springer-Verlag, 2009.
- [4] S. Sh. Gevorgian, A. K. Tagantsev, and A. K. Vorobiev, *Tuneable film bulk acoustic wave resonators*, Springer-Verlag London 2013.
- [5] R. York, A. Nagra, E. Erker, T. Taylor, P. Periaswamy, J. Speck, S. Streiffer, O. Auciello, "Microwave integrated circuits using thin-film BST," *Applications of Ferroelectrics*, 2000. ISAF 2000. Proceedings of the 2000 12th IEEE International Symposium on, Honolulu, HI, 2000, pp. 195-200 vol. 1.
- [6] A. Tombak, J.-P. Maria, F. T. Ayguavives, Z. Jin, G. T. Stauf, A. I. Kingon, and A. Mortazawi, “Tunable barium strontium titanate thin film capacitors for RF and microwave applications,” *IEEE Microw. Wireless Comp. Lett.*, vol. 12, pp. 3–5, Jan. 2002.
- [7] Tombak, J. P. Maria, F. T. Ayguavives, Zhang Jin, G. T. Stauf, A. I. Kingon, A. Mortazawi, "Voltage-controlled RF filters employing thin-film barium-strontium-titanate tunable capacitors," *IEEE Transactions on Microwave Theory and Techniques*, vol. 51, no. 2, pp. 462-467, Feb. 2003.
- [8] N. K. Pervez, P. J. Hansen, and R. A. York, “High tunability barium strontium titanate thin films for rf circuit applications,” *Appl. Phys. Lett.*, vol. 85, no. 19, pp. 4451-

4453, Nov. 2004.

- [9] D. R. Chase, L.-Y. Chen, and R. A. York, "Modeling the capacitive nonlinearity in thin-film BST varactors," *IEEE Trans. Microw. Theory Tech*, vol. 53, no. 10, pp. 3215-3220, Oct. 2005.
- [10] M. Schmidt, E. Lourandakis, R. Weigel, A. Leidl, and S. Seitz, "A thin-film BST varactor model for linear and nonlinear circuit simulations for mobile communication systems," in *2006 IEEE Int. Appl. Ferroelect. Symp.*, Aug. 2006, pp. 372-375.
- [11] E. Lourandakis, M. Schmidt, S. Seitz, and R. Weigel, "Reduced size frequency agile microwave circuits using ferroelectric thin-film varactors," *IEEE Trans. Microw. Theory Tech.*, vol. 56, no. 12, pp. 3093-3099, Dec. 2008.
- [12] X. Zhu, J. D. Phillips, and A. Mortazawi, "A DC voltage dependant switchable thin film bulk wave acoustic resonator using ferroelectric thin film," in *IEEE MTT-S Int. Microw. Symp. Dig.*, Jun. 2007, pp. 671-674.
- [13] X. Zhu, J. S. Fu, V. Lee, and A. Mortazawi, "Thin Film Ferroelectric Tunable Devices for Reconfigurable Radios," in *Proceedings of the Army Science Conference (26th)*, Orlando, FL. 2008.
- [14] X. Zhu, V. Lee, J. Phillips, and A. Mortazawi, "An intrinsically switchable FBAR filter based on barium titanate thin films," *IEEE Microw. Wireless Compon. Lett.*, vol. 19, no. 6, pp. 359-361, Jun. 2009.
- [15] X. Zhu, "Switchable and Tunable Ferroelectric Thin Film Radio Frequency Components," PhD dissertation, the University of Michigan, 2014.
- [16] A. Noeth, T. Yamada, V. O. Sherman, P. Muralt, A. K. Tagantsev and N. Setter, "DC bias-dependent shift of the resonance frequencies in BST thin film membranes," *IEEE Transactions on Ultrasonics, Ferroelectrics, and Frequency Control*, vol. 54, no. 12, pp. 2487-2492, December 2007.
- [17] Noeth, T. Yamada, A. K. Tagantsev, and N. Setter, "Electrical tuning of dc bias induced acoustic resonances in paraelectric thin films," *J. Appl. Phys.*, vol. 104, no. 9, pp. 094102-094102-10, Nov. 2008.
- [18] Noeth, T. Yamada, P. Muralt, A. K. Tagantsev, and N. Setter, "Tunable thin film bulk

- acoustic wave resonator based on Ba_xSr_{1-x}TiO₃ thin film," IEEE Trans. Ultrason. Ferroelectr. Freq. Control, vol. 57, no. 2, pp. 379-385, Feb. 2010.
- [19] S. A. Sis, V.C. Lee, and A. Mortazawi, "Intrinsically switchable, BST-on-silicon composite FBARs," in IEEE MTT-S International Microwave Symposium Digest, Baltimore, MD, 2011, pp. 1-4.
- [20] S.A. Sis, V. Lee, J. Phillips, and A. Mortazawi, "Intrinsically switchable thin film ferroelectric resonators," in IEEE MTT-S Int. Microw. Symp. Dig., pp. 1-3, Jun. 2012.
- [21] S. A. Sis, V. Lee, J. D. Phillips, and A. Mortazawi, "A DC voltage dependent switchable acoustically coupled BAW filter based on BST-on-silicon composite structure," in IEEE MTT-S International Microwave Symposium Digest, Montreal, QC, Canada, 2012, pp. 1-3.
- [22] S. A. Sis, V. Lee, S. Lee, and A. Mortazawi, "Intrinsically Switchable Thin Film Ferroelectric Resonators Utilizing Electric Field Induced Piezoelectric Effect," in IEEE MTT-S International Wireless Symposium Digest, Beijing, China, 2013, pp. 1-4.
- [23] S.A. Sis, S. Lee, V. Lee, A. Bayraktaroglu, J. Philips, and A. Mortazawi, "Intrinsically switchable, high-Q ferroelectric-on-silicon composite film bulk acoustic resonators," IEEE Trans. Ultrason. Ferroelectr. Freq., vol. 61, no. 2, pp. 231-238, Feb. 2014.
- [24] S.A. Sis, "Ferroelectric-on-Silicon Switchable Bulk Acoustic Wave Resonators and Filters for RF Applications," PhD dissertation, the University of Michigan, 2014.
- [25] S.A. Sis, S. Lee, V. Lee, and A. Mortazawi, "An intrinsically switchable, monolithic BAW filter using ferroelectric BST," IEEE Microwave and Wireless Components Letters (MWCL), vol. 26, no. 1, pp. 25-27, Jan. 2016.
- [26] V. Lee, S. A. Sis, X. Zhu, and A. Mortazawi, "Intrinsically switchable interdigitated barium titanate thin film contour mode resonators," in IEEE MTT-S International Microwave Symposium Digest, Anaheim, CA, 2010, pp. 1448-1450.
- [27] V. Lee, S. Lee, S.A. Sis, and A. Mortazawi, "Large signal performance of ferroelectric FBARs." in 2012 IEEE MTT-S International Microwave Symposium (IMS) Dig., Montreal, QC, pp. 1-3, June 2012.
- [28] V. Lee, S.A. Sis, S. Lee, and A. Mortazawi, "Intrinsically switchable ferroelectric bulk

- acoustic wave filters based on barium strontium titanate thin films," in 2013 IEEE MTT-S International Wireless Symposium (IWS) Dig., Beijing, China, pp. 1–4, April 2013.
- [29] V. Lee, S. Lee, S.A. Sis, and A. Mortazawi, "Switching reliability of tunable ferroelectric resonators and filters," in 2013 IEEE MTT-S International Microwave Symposium (IMS) Dig., Seattle, WA, pp. 1–4, June 2013.
- [30] V. Lee, S. A. Sis, J. Phillips, and A. Mortazawi, "Intrinsically Switchable Ferroelectric Contour Mode Resonators," *IEEE Transactions on Microwave Theory and Techniques*, vol. 61, no. 8, pp. 2806-2813, Aug. 2013.
- [31] V. Lee, S.A. Sis, S. Lee, X. Zhu, and A. Mortazawi, "Lateral mode intrinsically switchable barium titanate film bulk acoustic wave resonators," in 2013 European Microwave Conference (EuMC), Nuremberg, Germany, pp. 1347-1350, October 2013.
- [32] V. Lee, "Switchable and tunable ferroelectric devices for adaptive and reconfigurable RF circuits", PhD dissertation, the University of Michigan, 2014.
- [33] V. Lee, S. Lee, S.A. Sis, and A. Mortazawi, "Switchable dual-frequency barium strontium titanate film bulk acoustic resonators," in 2014 IEEE MTT-S International Microwave Symposium (IMS) Dig., Tampa, FL, pp. 1–4, June 2014.
- [34] V. Lee, S. Lee, S.A. Sis, and A. Mortazawi, "Switching reliability and switching speed of barium strontium titanate (BST) BAW devices," in 2014 European Microwave Conference (EuMC), Rome, Italy, pp. 500-503, October 2014.
- [35] S. Lee, V. Lee, S.A. Sis, and A. Mortazawi, "Large signal modeling of switchable ferroelectric FBARs," in 2012 European Microwave Integrated Circuits Conference (EuMIC), Amsterdam, Netherlands, pp. 24-27, October 2012.
- [36] S. Lee, V. Lee, S.A. Sis, and A. Mortazawi, "Large-signal performance and modeling of intrinsically switchable ferroelectric FBARs," *IEEE Trans. Microw. Theory Tech.*, vol. 61, no. 1, pp. 415-422, Jan. 2013.
- [37] S. Lee, V. Lee, S.A. Sis, and A. Mortazawi, "Linearity analysis of intrinsically switchable ferroelectric FBAR filters," in *IEEE MTT-S Int. Microw. Symp. Dig.*, pp. 1-3, Jun. 2013.

- [38] S. Lee, V. Lee, S.A. Sis, and A. Mortazawi, "A simple nonlinear mBVD model parameter extraction method for intrinsically switchable ferroelectric FBARs," in Eur. Microw. Conf., Oct. 2013, pp. 1355-1358.
- [39] S. Lee, V. Lee, S.A. Sis, and A. Mortazawi, "Physics-based large-signal modeling of intrinsically tunable and switchable ferroelectric FBARs," in 2014 IEEE MTT-S International Microwave Symposium (IMS) Dig., Tampa, FL, pp. 1–4, June 2014.
- [40] S. Lee, M. Zolfagharloo Koochi, V. Lee, S.A. Sis, and A. Mortazawi, "Temperature dependent characteristics of intrinsically switchable ferroelectric composite FBARs," in 2015 IEEE MTT-S International Microwave Symposium (IMS) Dig., Phoenix, AZ, pp. 1-4, May 2015.
- [41] S. Lee and A. Mortazawi, "An intrinsically switchable ladder-type ferroelectric BST-on-Si composite FBAR filter," IEEE Trans. Ultrasonics, Ferroelectrics, and Frequency Control (TUFFC), vol. 63, no. 3, pp. 456-462, Mar. 2016.
- [42] S. Lee and A. Mortazawi, "BAW filter design method based on intrinsically switchable ferroelectric BST FBARs," in 2016 IEEE MTT-S International Microwave Symposium (IMS) Dig., San Francisco, CA, to be presented in May 2016.
- [43] S. Lee, M. Zolfagharloo Koochi, and A. Mortazawi, "Lateral-wave spurious-modes elimination in switchable ferroelectric BST-on-Si composite FBARs," in 2016 IEEE MTT-S International Microwave Symposium (IMS) Dig., San Francisco, CA, to be presented in May 2016.
- [44] S. Gevorgian, A. Vorobiev, and T. Lewin, "dc field and temperature dependent acoustic resonances in parallel-plate capacitors based on SrTiO₃ and Ba_{0.25}Sr_{0.75}TiO₃ films: Experiment and modeling," J. Appl. Phys., vol. 99, no. 12, pp. 124112-124112-11, Jun. 2006.
- [45] J. Berge, A. Vorobiev, W. Steichen, and S. Gevorgian, "Tunable solidly mounted thin film bulk acoustic resonators based on Ba_xSr_{1-x}TiO₃ Films," IEEE Microw. Wireless Compon. Lett. vol. 17, no. 9, pp. 655-657, Sep. 2007.
- [46] J. Berge, M. Norling, A. Vorobiev, and S. Gevorgian, "Field and temperature dependent parameters of the dc field induced resonances in Ba_xSr_{1-x}TiO₃-based tunable thin film bulk acoustic resonators," J. Appl. Phys., vol. 103, no. 6, pp.

064508–064508-8, March 2008.

- [47] M. Norling, J. Berge, and S. Gevorgian, "Parameter extraction for tunable TFBARs based on $\text{Ba}_x\text{Sr}_{1-x}\text{TiO}_3$," in IEEE MTT-S Int. Microw. Symp. Dig., Jun. 2009, pp. 101-104.
- [48] A. Vorobiev, S. Gevorgian, M. Löffler, and E. Olsson, "Correlations between microstructure and Q-factor of tunable thin film bulk acoustic wave resonators," J. Appl. Phys., vol. 110, pp. 054102-1–054102-11, September 2011.
- [49] Vorobiev and S. Gevorgian, "Improved tunable performance of high Q-factor $\text{Ba}_x\text{Sr}_{1-x}\text{TiO}_3$ film bulk acoustic wave resonators," Eur. Microw. Integrated Circuits Conf., vol., pp.20-23, Oct. 2012.
- [50] G. N. Saddik, D. S. Boesch, S. Stemmer, and R. A. York, "dc electric field tunable bulk acoustic wave solidly mounted resonator using SrTiO_3 ," Appl. Phys. Lett., vol. 91, no. 4, pp. 043501-043501-3, Jul. 2007.
- [51] G. N. Saddik and R. A. York, "Capacitively coupled dc voltage switchable barium strontium titanate solidly mounted resonator filter," Microwave Symposium Digest (MTT), 2011 IEEE MTT-S International, Baltimore, MD, 2011, pp. 1-4
- [52] G. N. Saddik and R. A. York, "Temperature dependence of DC voltage activated $\text{Ba}_{0.5}\text{Sr}_{0.5}\text{TiO}_3$ solidly mounted resonator," 2012 IEEE MTT-S Int. Microwave Symp. Dig., pp. 1-3, June 2012.
- [53] G.N. Saddik and R.A. York, "An L-section DC electric field switchable bulk acoustic wave solidly mounted resonator filter based on $\text{Ba}_{0.5}\text{Sr}_{0.5}\text{TiO}_3$," IEEE Trans. Ultrason. Ferroelectr. Freq. Control, vol.59, no.9, pp.2036-2041, Sep. 2012.
- [54] G. N. Saddik and R. A. York, "Impact of chemical mechanical polishing on the quality factor of $\text{Ba}_{0.5}\text{Sr}_{0.5}\text{TiO}_3$ solidly mounted resonator," Microwave Symposium Digest (IMS), 2013 IEEE MTT-S International, Seattle, WA, 2013, pp. 1-4.
- [55] K.M. Lakin, "Thin film resonators and filters," 1999 IEEE Ultrasonics Symp. Dig., vol. 2, pp. 895-906, October 1999.
- [56] R. Ruby, "A snapshot in time," IEEE Microwave Mag., vol. 16, no.7, pp. 46-59, August 2015.

- [57] R. Aigner, "Bringing BAW technology into volume production: The ten commandments and seven deadly sins," in Proc. Int. Chiba Symp. on Acoustic Wave Devices, 2007, pp. 85–91.
- [58] R. Aigner, N.-H. Huynh, M. Handtmann, and S. Marksteiner, "Behavior of BAW devices at high power levels," in IEEE MTT-S Int. Microw. Symp. Dig., Jun. 2005, pp. 429-432.
- [59] D.S. Shim and D.A. Feld, "A general nonlinear Mason model of arbitrary nonlinearities in a piezoelectric film," in IEEE Ultrason. Symp., Oct. 2010, pp. 295-300.
- [60] K. M. Lakin, G. R. Kline, and K. T. McCarron, "High-Q microwave acoustic resonators and filters," IEEE Trans. Microw. Theory Tech, vol. 41, no. 12, pp. 2139-2146, Dec. 1993.
- [61] COMSOL Multiphysics, COMSOL Inc.
- [62] F. Z. Bi and B. P. Barber, "Bulk acoustic wave RF technology," IEEE Microw. Mag., vol. 9, no. 5, pp. 65-80, Oct. 2008.
- [63] Matlab, MathWorks, Inc.
- [64] K. M. Lakin and J. S. Wang, "Acoustic bulk wave composite resonators," Appl. Phys. Lett., vol. 38, no. 3, pp. 125-127, Feb. 1981.
- [65] J. Rosenbaum, H.L., Jr. Salvo, and S.V. Krishnaswamy, "Overtone Response of Composite Bulk Acoustic Resonators," 40th Annual Symposium on Frequency Control. 1986 , vol., no., pp.206,210, 28-30 May 1986.
- [66] J. Rosenbaum, "Design of Ultra High Frequency Composite Piezoelectric Resonators," Applications of Ferroelectrics. 1986 Sixth IEEE International Symposium on , vol., no., pp.296,299, 8-11 June 1986.
- [67] A. Artieda and P. Muralt, "High-Q AlN/SiO₂ symmetric composite thin film bulk acoustic wave resonators," Ultrasonics, Ferroelectrics and Frequency Control, IEEE Transactions on , vol.55, no.11, pp.2463-2468, November 2008.
- [68] H.M. Lavasani, R. Abdolvand, and F. Ayazi, "A 500MHz Low Phase-Noise AlN-on-Silicon Reference Oscillator," Custom Integrated Circuits Conference, 2007. CICC '07. IEEE , vol., no., pp.599,602, 16-19 Sept. 2007.

- [69] W. Pang, R.C. Ruby, R. Parker, P.W. Fisher, J.D. Larson, K.J. Grannen, D. Lee, C. Feng, and L. Callaghan, "11E-3 A Thermally Stable CMOS Oscillator Using Temperature Compensated FBAR," Ultrasonics Symposium, 2007. IEEE , vol., no., pp.1041,1044, 28-31 Oct. 2007.
- [70] M. Li, S. Seok, N. Rolland, P. Rolland, H. El Aabbaoui, E. De Foucauld, and P. Vincent, "Comparison of low phase noise oscillators topologies using BAW resonator," Microwave Integrated Circuits Conference (EuMIC), 2010 European , vol., no., pp.345,348, 27-28 Sept. 2010.
- [71] R. Ruby, "Review and comparison of bulk acoustic wave FBAR, SMR technology," in Proc. IEEE Ultrasonics Symp., pp. 1029–1040, October 2007.
- [72] J. Kaitila, M. Ylilammi, J. Ellä, and R. Aigner, "Spurious resonance free bulk acoustic wave resonators," in Proc. IEEE Ultrasonics Symp., pp. 84–87, October 2003.
- [73] J. Kaitila, "BAW device basics," in RF bulk acoustic wave filters for communications, K. Hashimoto , Ed., Artech House, 2009.
- [74] H.P. Hsu, "On The General Relation Between α and Q (Correspondence)," Microwave Theory and Techniques, IEEE Transactions on , vol.11, no.4, pp.258, July 1963.
- [75] R. Ruby, "FBAR resonators and filters," in RF bulk acoustic wave filters for communications, K. Hashimoto , Ed., Artech House, 2009.
- [76] R. Melamud, S. A. Chandorkar, B. Kim, H. K. Lee, J. C. Salvia, G. Bahl, M. A. Hopcroft, and T. W. Kenny, "Temperature-insensitive composite micromechanical resonators," J. Microelectromech. Syst., vol. 18, no. 6, pp. 1409-1419, December 2009.
- [77] K.-Y. Hashimoto, RF bulk acoustic wave filters for communications, Boston: Artech House, 2009.
- [78] A. Link and P. Warder, "Golden age for filter design," IEEE Microwave Mag., vol. 16, no.7, pp. 60-72, August 2015.
- [79] O. Ikata, T. Miyashita, T. Mastsuda, T. Nishihara, and Y. Satoh, "Development of low-loss band-pass filters using SAW resonators for portable telephones," Proc.

- IEEE Ultrasonics Symp., pp. 111-115, October 1992.
- [80] O. Menendez, P. de Paco, R. Villarino, and J. Parron, "Closed-form expression for the design of ladder-type FBAR filters," *IEEE Microw. Wireless Compon. Lett.*, vol. 16, no. 12, pp. 657-659, December 2006.
- [81] M. Ueda, "Comparison with SAW devices," in *RF bulk acoustic wave filters for communications*, K. Hashimoto, Ed., Artech House, 2009.
- [82] S.B. Cohn, "Dissipation loss in multiple-coupled resonator filters," *Proc. IRE*, vol. 47, no. 8, pp. 1342-1348, August 1959.
- [83] L. N. Dworsky, "A comparison of band pass filter technologies for communications system applications," in *Proc. IEEE Int. Ultrason. Symp.*, 1991, pp. 241–250.
- [84] K.M. Lakin, "A review of thin-film resonator technology," *IEEE Microw. Mag.*, vol. 4, no. 4, pp. 61-67, Dec. 2003.
- [85] K.M. Lakin, "Thin film resonator technology," *IEEE Trans. Ultrason. Ferroelectr. Freq.*, vol. 52, no. 5, pp. 707-716, May. 2005.
- [86] G. Matthaei, E.M.T. Jones, and L. Young, *Microwave filters, impedance-matching networks, and coupling structures*, Artech House, 1980.
- [87] J.-S. Hong, *Microstrip filters for RF/Microwave Applications*, second edition, Wiley, 2011.
- [88] D.M. Pozar, *Microwave Engineering*, 4th ed., New York: J. Wiley & Sons, 2012.
- [89] J. D. Larson, III, P.D. Bradley, S. Wartenberg, and R.C. Ruby, "Modified Butterworth-Van Dyke circuit for FBAR resonators and automated measurement system," in *Proc. IEEE Int. Ultrason. Symp.*, pp. 863–868, October 2000.
- [90] T. H. Lee, "The Design of CMOS Radio-Frequency Integrated Circuits," Second Edition, Cambridge University Press, 2003.
- [91] *Advanced Design System (ADS)*, Agilent Technol.